



## City Research Online

### City, University of London Institutional Repository

---

**Citation:** Elshalakani, M. O. M. E (2020). Investigation of biomimetic systems and their applications in robotic solutions in fluids: using deep learning and vision-based control. (Unpublished Doctoral thesis, City, University of London)

This is the accepted version of the paper.

This version of the publication may differ from the final published version.

---

**Permanent repository link:** <https://openaccess.city.ac.uk/id/eprint/25329/>

**Link to published version:**

**Copyright:** City Research Online aims to make research outputs of City, University of London available to a wider audience. Copyright and Moral Rights remain with the author(s) and/or copyright holders. URLs from City Research Online may be freely distributed and linked to.

**Reuse:** Copies of full items can be used for personal research or study, educational, or not-for-profit purposes without prior permission or charge. Provided that the authors, title and full bibliographic details are credited, a hyperlink and/or URL is given for the original metadata page and the content is not changed in any way.

---

---

---

City Research Online:

<http://openaccess.city.ac.uk/>

[publications@city.ac.uk](mailto:publications@city.ac.uk)

---

# Investigation of Biomimetic Systems and their Applications in Robotic Solutions in Fluids: Using Deep Learning and Vision-Based Control

Mohamed Omar Mohamed Elsayed Elshalakani

Thesis submitted for the degree of Doctor of Philosophy



Department of Mechanical Engineering &  
Aeronautics

City, University of London

July, 2020



# Contents

<b>Contents</b>	<b>2</b>
<b>List of Figures</b>	<b>6</b>
<b>List of Tables</b>	<b>15</b>
<b>Acknowledgements</b>	<b>16</b>
<b>Abstract</b>	<b>18</b>
<b>Thesis Contributions</b>	<b>19</b>
<b>1 Introduction</b>	<b>22</b>
1.1 Motivations and research aims . . . . .	23
1.1.1 Biomimetic sensors for underwater surveillance . . . . .	23
1.1.2 Hydrodynamic sensing using artificial seal whiskers . . . . .	24
1.1.3 Emergence of metachronal coordination in experiment . . . . .	24
1.1.4 Propulsion as a result of spontaneous coordination . . . . .	26
1.2 Thesis outline . . . . .	28
<b>2 Background</b>	<b>30</b>
2.1 Study one . . . . .	30
2.1.1 Whiskers as tactile sensors . . . . .	30
2.1.2 Marine mammals and hydrodynamic detection . . . . .	31
2.1.3 Whisker-inspired robotic sensors . . . . .	32
2.1.4 Key questions addressed by the present research . . . . .	34
2.1.5 Relevant previous studies . . . . .	34

2.2	Study two and three . . . . .	34
2.2.1	Cilia and metachronal coordination . . . . .	34
2.2.2	Dynamical similarity . . . . .	36
2.2.3	Emergence of assembly . . . . .	37
2.2.4	Hydrodynamic synchronization . . . . .	38
2.2.5	Low-Reynolds swimmers . . . . .	38
2.2.6	Key questions addressed by the present research . . . . .	41
2.2.7	Relevant previous studies . . . . .	42
<b>3</b>	<b>A Deep-Learning Model for Underwater Position Sensing of a Wake’s Source Using Artificial Seal Whiskers</b>	<b>44</b>
3.1	Introduction . . . . .	45
3.2	Materials and methods . . . . .	49
3.2.1	Physical model . . . . .	49
3.2.2	Experiment . . . . .	50
3.2.3	Data acquisition . . . . .	51
3.2.4	Data processing and feature extraction . . . . .	54
3.2.5	Supervised learning models . . . . .	57
3.3	Results . . . . .	59
3.3.1	Wake-induced bending of the whiskers . . . . .	59
3.3.2	Prediction outcomes of the learning models . . . . .	62
3.3.3	Sensitivity of the predictions to the size of the training dataset	66
3.3.4	Sensitivity of the predictions to the number of whisker-pairs included in the training . . . . .	67
3.4	Discussion and conclusions . . . . .	69
3.5	Appendix A . . . . .	73
3.6	Appendix B . . . . .	75
3.7	Critical Analysis . . . . .	76
3.7.1	Overview and study contributions . . . . .	76
3.7.2	Exploratory discussion and future work . . . . .	76

3.7.3	Prediction of the direction of the disturbance source and selection of the parameter $T$ . . . . .	81
<b>4</b>	<b>Spontaneous Synchronization of Beating Cilia: An Experimental Proof Using Vision-Based Control</b>	<b>84</b>
4.1	Introduction . . . . .	85
4.2	Materials and methods . . . . .	87
4.2.1	Fluidic chamber and artificial cilia . . . . .	87
4.2.2	Computer-vision system . . . . .	88
4.2.3	Feedback control-loop . . . . .	90
4.2.4	Reference test in an inviscid environment . . . . .	91
4.3	Results . . . . .	91
4.4	Discussion and conclusions . . . . .	92
4.5	Critical analysis . . . . .	100
4.5.1	Overview and study contributions . . . . .	100
4.5.2	Exploratory discussion and future work . . . . .	100
4.5.3	Flow propulsion as a consequence of metachronal self-coordination	103
<b>5</b>	<b>Simulation of Self-Coordination in a Row of Beating Flexible Flaplets for Micro-Swimmer Applications: Model and Experiment Study</b>	<b>105</b>
5.1	Introduction . . . . .	107
5.2	Concept formulation . . . . .	109
5.2.1	Model objective . . . . .	109
5.2.2	Material and environment . . . . .	109
5.3	Experiment description . . . . .	110
5.3.1	Set-up and control loop . . . . .	110
5.4	Theoretical modelling . . . . .	112
5.4.1	Mathematical description . . . . .	113
5.4.2	State-space model . . . . .	116
5.5	Results and analysis . . . . .	117
5.5.1	Hydrodynamic synchronization . . . . .	117
5.5.2	Net propulsion force . . . . .	120

5.5.3	Stability of the synchronization . . . . .	122
5.6	2D flow visualization . . . . .	122
5.7	Conclusion . . . . .	126
5.8	Appendix A . . . . .	129
5.9	Critical analysis . . . . .	138
5.9.1	Overview and study contributions . . . . .	138
5.9.2	Exploratory discussion and future work . . . . .	138
5.9.3	Relation between the number of flaplets and the time required for self-synchronization . . . . .	141
5.9.4	Flow visualization results due to different coordination phase- shifts among the flaplets . . . . .	142
<b>6</b>	<b>Conclusions</b>	<b>145</b>
	<b>Bibliography</b>	<b>148</b>

## List of Figures

2.1	Experiment of harbour seal tracking a hydrodynamic wake generated by another pilot seal; from (Schulte-Pelkum et al. 2007). (a) the trail-tracking seal while blindfolded detects the swimming direction using its whiskers. (b) the path followed by the seal (red line) in approximately 60% of the performed trials while tracking the pilot’s path (blue line). In most of the remaining trials, the seal could also follow the path successfully but with some undulatory deviations from the original path. . . . .	31
2.2	Outer surfaces of two whiskers that belong to a California sea lion (top) and the Harbor seal (bottom); from (Murphy et al. 2013). . . .	32
2.3	E-whisker sensors used for active and passive sensing in robotic applications; (a) artificial rat-whisker array attached to a robotic manipulator and used for texture classification of different surfaces; from (Sullivan et al. 2011); (2) wake-detection system composed of 8 artificial whiskers that can identify and track the trail of a pilot submarine; from (Eberhardt et al. 2016). . . . .	33
2.4	Schematic representation of the periodic motion of cilia: (a) different phases of a beat cycle of a single cilium where the power and return strokes are highlighted in blue and red respectively. The dash line highlights the path undertaken by the cilium’s tip during the cycle; (b) a metachronal wave formed by a group of beating cilia. . . . .	36

2.5	Emergence of hydrodynamic synchronization at low Reynolds numbers; (a) model of cilia arrays self-assembly in metachronal waves; from (Elgeti & Gompper 2013); (b) anti-phase synchronization of oscillating colloidal spheres; from (Kotar et al. 2010). . . . .	39
2.6	Schematics of numerical and experimental examples of micro-swimmer models. (a) gait cycle of the Purcell’s three link swimmer; from (Becker et al. 2003); (b) model of a linked two-sphere swimmer that can be actuated using optical tweezers; from (Nasouri et al. 2017); (c) realization of a magnetic-field-actuated helical micro-swimmer whose structure is derived from different plants; from (Gao et al. 2014). . . . .	41
3.1	Three-dimensional (3D) printed model of the pinniped head. (a) captured image of the head while the optical fibres are illuminated. (b) side view (c) plan view of the head. . . . .	50
3.2	Experimental set-up of the artificial head and the flow disturbance inside the water tunnel. The side view (top) shows the optical setup of a high-speed camera underneath the test section and a 45° mirror that are used to monitor the motion of the illuminated whisker tips. The plan view (bottom) shows the boundary locations of the cylinder during different tests. The recorded data of the whiskers’ vibrations due to the existence of the cylinder at different locations are used for training the learning models. The origin of the coordinate system is placed at the intersection of the head axis with its frontal face. . . . .	52
3.3	Camera views in the $(x, y)$ plane of the two recording modes: (a) grey-level compressed mode. (b) binary mode with centroid calculation. The grey-level image is masked before binarization so that only the 12 whiskers’ tips of interest are visible. The whiskers are numbered from 1 to 12 such that whiskers no. 1, 6, 7 and 12 indicate the front-left, rear-left, front-right and rear-right whiskers respectively. . . . .	53

3.4	Camera views in the $(y, z)$ plane of the whiskers on the right side of the head; from (Muthuramalingam & Bruecker 2019). This set-up was used in another study that used the same whisker-array sensor. Here, we only borrow the recorded $z$ -deflection response, presented in section 3.3.1, to quantify the deflection response in the $z$ direction in reaction to the cylinder wake and compare it to the $y$ component of deflection that we use in this study. . . . .	54
3.5	Distribution of the mean and fluctuating deflection samples (inputs to the learning models) for the 12 whiskers in the $(\gamma', \bar{\gamma})$ space: (a) population of the complete input dataset that correspond to all positions of the cylinder. Highlighted in blue and red are the data samples of the whiskers numbered 1 and 12 respectively. (b) input samples of two selected recordings that correspond to the cylinder positions $(-15, 75)$ and $(5, 75)$ . The scattered sample points are coloured by their whisker indexes as represented by the colour bar. . . . .	56
3.6	Schematic drawing highlighting the $x$ and $y$ components of the whisker's bending deflection in the $(x, y)$ plane (the recorded plane in the used camera setup). . . . .	60
3.7	Wake-induced deflection values of a sample whisker in the $z$ (bottom), $x$ (middle) and $y$ (top) directions. . . . .	61
3.8	Deflection responses of a selected whisker tip due to the existence of the cylinder at different locations: (a) variation of the tip's deflection response due to different $x$ -coordinate locations of the cylinder. The curves from top to bottom represent the following cases respectively: no cylinder (reference case), cylinder positions: $(-5, 75)$ , $(0, 75)$ , $(5, 75)$ . (b) variation of the tip's deflection response due to different $y$ -coordinate locations of the cylinder. The curves from top to bottom represent the following positions of the cylinder, respectively: $(5, 85)$ , $(5, 29)$ . . . . .	63

3.9	Results of the NNs predictions of $(x, y)$ coordinates of different cylinder locations using the input samples of the training dataset. (a,b) predicted outputs of $(x, y)$ as a linear fitted function of their labeled targets. (c,d) histogram plots of the prediction error instances resulted from both models. . . . .	64
3.10	Results of the NNs predictions of $(x, y)$ coordinates of three different cylinder locations using the input samples of the test dataset. For a total of 59 input samples and three different locations of the cylinder, the prediction instances of each location and their mean are represented by different colours (left). The two-dimensional (2D) error histogram (algorithm available here ( <i>Efficient 2D histogram, no toolboxes needed, MATLAB Central File Exchange. Retrieved from: n.d.</i> )) is presented as a colour-contour plot with a total number of 25 bins and a biharmonic interpolant fitting function (right). . . . .	65
3.11	Structure of the $M$ -layer feedforward neural networks used for the prediction of the $x$ and $y$ coordinates of the cylinder position. . . . .	73
3.12	Schematic showing the difference between the vortex-induced vibrations (left) and the wake-induced vibrations (right) of the whisker. . . . .	77
3.13	Performance results of the trained neural-network models for the prediction of the disturbance source direction (the angle $\psi$ ) for varying values of $T$ . . . . .	83
3.14	Error histogram plots of the angle $\psi$ predictions of the associated neural network models for: (a) $T = 2$ s and (b) $T = 3$ s. . . . .	83
4.1	Schematic view of the closed working chamber: (a) front view of the chamber with the five flexible flaplets at resting conditions and (b) side view of one flaplet clamped on the short side to the axle of one of the five motors. . . . .	88
4.2	Schematic view of the optical set-up to record the tip motion of the artificial cilia. . . . .	89

4.3	Original image of the flaplet tips after binarization and color inversion for a single instant in the process of self-organization. For reference, we overlaid circles marking the centroids and the flaplet tip contours (dashed lines). The oscillatory motion is along the horizontal image axis, perpendicular to the flaplet span. The left-most flaplet is $i = 1$ , and the right most is $i = 5$ in rising order. Note that the roots of the model cilia are uniformly spaced, as shown in Fig. 4.1. . . . . .	89
4.4	Schematic view of the integrated mechatronic system (a) and the feedback control-loop flow chart (b). . . . .	90
4.5	Position trajectories of the five flaplet tips while applying the feedback control loop; (top): flaplets in reference case (air); (bottom): flaplets in highly viscous liquid. The black lines indicate the phase relationships between maxima of neighbouring flaplets over time. The position corresponds to the centroid coordinate of the flaplet tip marker in pixel units along the horizontal image axis in Fig. 4.3. The colors indicate the different flaplets (red: flaplet $i = 1$ , blue: flaplet $i = 5$ ). Note that we selected for visibility reasons in the plot for air the initial phase shift between pairs of cilia to be at the extreme value of $180^\circ$ , which results in out-of-phase beating. Therefore, the black lines in the upper plot do not indicate any synchronization, as there is no interaction between the flaplets. . . . .	93
4.6	Evolution of the flaplet-to-flaplet phase relationship in the first 18 cycles, shown in terms of the cycle ratio $CR_{n3-5}$ between pairs of flaplets 2–5. For comparison, the black line shows the behavior of one pair of flaplets $CR_{n4}$ for the reference case in air. The curve fitting is done with a smoothing spline. The gray shaded region is the range of cycle ratios reported in literature for metachronal waves of model cilia to achieve optimum fluid transport (Gauger et al. 2009).	94

4.7	Repetition of the control experiment in glycerol; compare this to Figure 5b. Note, again, emergence of metachronal coordination after about 15 cycles. Herein, the observed metachronal wave runs in opposite direction to the one documented in Figure 5, bottom. For explanation of the lines see the figure caption in Figure 5. . . . .	96
4.8	PDF of the individual “teeth” to overlap with the mean in the zig-zag motion profile for a selected flaplet in air (a) and glycerol (b) for a total period of 1 min. Blue values show a larger deviation from the mean, while red is aligned with the mean of all teeth. Note that all teeth are fixed with their maximum position at beginning of cycle time 0. . . . .	98
4.9	Peaks of normalized autocorrelation function of the zig-zag motion profile for a selected flaplet in air (red symbol “+”) and glycerol (blue symbol “x”) for a total period of 1 min. For illustration, the continuous auto-correlation profile is added for the case of glycerol as a solid line in blue. . . . .	99
4.10	Illustration of the time-reversibility principle for the phase-coordination of five flaplets; (a) out-of-phase $\Delta\phi = 180^\circ$ coordination of the flaplets as a time-reversible gait sequence; (b) $\Delta\phi = 90^\circ$ coordination of the flaplets as a time-irreversible gait sequence. The sequence in (b) violates the Purcell’s symmetry arguments and therefore is expected to generate uni-directional net transport of the surrounding fluid. . . .	104
5.1	The experimental set-up of the five flexible flaplets in the viscous chamber. Each flaplet is clamped from one end to the spindle axle of a rotary motor. (a,b) front view (c) top view (d) side view (b,d) schematic drawings that show the geometrical parameters of the flaplets.	111

5.2	Physical implementation of the control closed-loop based on the geometric clutch hypothesis. The feedback signal is the position of the oscillators' tips that are marked with florescent dyes which can be captured by the high-speed camera. Another measurement of the feedback signal is applicable by the use of strain gauges that can capture the tips' deflection. . . . .	112
5.3	Lumped element model of the flaplet highlighting the viscous-coupling parameters. The description of the model parameters is provided in Table 5.1. . . . .	115
5.4	Normalized deflection of a still flaplet's tip due to the oscillation of its right neighbour during two successive beat cycles. The distance $r$ between the two neighbouring tips varies in the domain $0 < r < 2A$ during a beat cycle. . . . .	117
5.5	Position trajectories of 32 oscillators' tips in the modelled viscous environment. The randomness in the phase relationship is shown as curvy lines at the start of the beating (left). The emerged synchronization is shown as straight (constant slope) lines after 225 cycles from the start of beating (right) . . . . .	118
5.6	Evolution of synchronization in a row of five flexible oscillators in the model (top) and in the experiment (bottom). The different colours indicate different oscillators. The solid lines indicate a constant phase slope among four neighbouring oscillators and the dash lines are parallel to the solid ones and show the deviations from coordination at the early stages. . . . .	119

5.7	Evolution of the net propulsion force that arises due to the emerged synchronization at $\zeta \simeq 3$ . The presented results are for 32- and 16-oscillator models respectively. The shaded areas represent the period after the synchronization lines (constant slope lines) are witnessed in the tips' position trajectories (red for $N = 16$ and blue for $N = 32$ ). The blue area is shown on top of the red area which also covers the part beneath it. The dash lines bound the growth in the effective forces due to barely noticeable deviations in the phase slopes during the coordinated state. . . . .	121
5.8	Schematic of the experimental setup for the Particle Image Velocimetry measurements. A vertical laser light-sheet parallel to the X–Y plane and passing through the centre of the flaplets is used along with the shown camera configuration to record the 2D flow field around the oscillators while beating in metachronal coordination. . . . .	124
5.9	The pathlines of the tracer particles in the glycerine fluid as the flaplets follow the metachronal wave pattern prescribed by Eq. 5.11. The image is acquired by overlaying the frame of the flaplets with 5 phase-locked particle images that are recorded with a frame rate equal to the frequency of the flaplets' oscillatory motion. The direction of the flaplet oscillation at the instance of recording is shown by the white arrows. . . . .	125
5.10	Time-averaged vector map of the velocity field in a vertical plane around the oscillators while beating in the metachronal coordination prescribed by Eq. 5.11. The colour map overlaid with the graph represents the magnitude and direction of $u$ in $mm/s$ (the $X$ component of the velocity vectors). . . . .	126

5.11	(a,b) Schematic view of the oscillator model as a simple beam (c) the curvature of deflection and strain parameters in the x–y plane. The deflection of the oscillator is magnified in the figures for better visibility. The actual deflection does not exceed 5% of the total length. The coordinate system (x,y,z) introduced here is attached to the oscillator and inherits its orientation while the global coordinate system (X,Y,Z) is presented in Fig. 5.8. . . . . .	130
5.12	CFD model results of the normalized pressure difference between the x–z faces of a flaplet that rotates inside the viscous medium at a Reynold number of $Re \simeq 0.2$ . . . . .	132
5.13	Normalized deflection magnitude of a rotating flaplet in glycerine as a function of its normalized angular speed. The bar lines indicates the deviation of the dynamic deflection from its mean during a single beat cycle. . . . .	133
5.14	Normalized deflection of a still flaplet due to the rotation of its neighbour as a function of the normalized distance between their tips. The ramp dashed line is a linear fit for the deflection values that are greater than 2% of the oscillation amplitude. From there the deflection is considered constant. . . . .	134
5.15	The model of the flexible flat-plate oscillator as a mass–spring–damper system. . . . .	136
5.16	Measured response of the oscillator’s tip in the glycerine liquid due to an initial imposed deflection; $\gamma(0)$ . . . . .	137
5.17	Number of oscillators to reach synchronization during the build-up stage of full metachronal coordination of 32 oscillators. Each oscillator is considered to join coordination once it reaches within 2% around its steady-state phase relationship with its adjacent neighbour. . . . .	142
5.18	Flow visualization results of the coordinated oscillators for different phase relationships. . . . .	144

## List of Tables

2.1	Previous studies on whisker-like devices in engineering applications. . . . .	35
2.2	Previous studies on micro-swimmers and propulsion devices at low-Reynolds numbers. . . . .	42
2.3	Previous studies on the self-coordination of artificial and model cilia. . . . .	43
3.1	Camera settings for the recording of the artificial seal whiskers. . . . .	53
3.2	Sensitivity of the prediction accuracy ( $\text{mean}[R]$ ) of the $(x, y)$ models to the size of the training dataset. . . . .	67
3.3	Sensitivity of the prediction accuracy ( $\text{mean}[R]$ ) of the $(x, y)$ models to the number of whisker pairs included in the training stage. The number is varied in the front-to-rear direction of the whiskers (top) and vice versa (bottom). . . . .	68
5.1	Description of the parameters of the mathematical model . . . . .	114

## Acknowledgements

Undertaking this PhD has been a life-changing experience for me that would not have been possible without the support and guidance that I received along the way.

Firstly, with deep gratitude, I would like to express my sincere appreciation to my supervisor, Professor Christoph Bruecker, who has continually offered his precious support and advice to me throughout my PhD at City, University of London. Without his guidance and persistence to help, this work would have not been brought to light.

My sincere thanks goes to my family; parents, wife and siblings, for their peerless and unceasing support. They kept me going on and this work would not have been possible without their help.

I would also like to thank the Deutsche Forschungsgemeinschaft (DFG) for supporting my current doctorate position under the reference number BR 1491/30-1 and within the research project “Microswimmers”.

Special thanks go to my PhD-team members, Qianhui Li, Edward Tallboys, Muthukumar Muthuramalingam and Omar Selim, for their support and helpful discussions. Additional thanks to Muthukumar Muthuramalingam for providing me with the helpful resources for the water-tunnel experiment and for helping in the setup and data collection of that experiment. The comments and advice I received along the way from the research staff at City are also gratefully acknowledged.

I am also very grateful to all the postgraduate officers at City University especially Ms. Nathalie Chatelain. They were always so helpful and provided me with their assistance throughout my PhD.



## Abstract

Impressive robotic solutions with astonishing capabilities have been designed to inherit certain propensities of living creatures and mimic some of their abilities in order to perform real-life tasks. In the present work, two bio-inspired systems are developed to investigate certain characteristics of biological hair-like structures and employ their behaviours in robotic and sensory solutions in fluids. The first is an intelligent sensor that is developed using deep learning to detect the position of underwater wake-generating objects inspired by the seal's ability to track its prey by sensing the surrounding fluid motion using its facial hairs (i.e., whiskers). The produced sensor provides a safe, passive and lifelike way of underwater sensing which can be utilized in robotic applications for underwater navigation in dark or cloudy environments and in situations that require stealth. The second is a mechatronic system that is designed and implemented to resemble the self-organization of biological cilia in an enlarged model and to generate flow propulsion at low-Reynolds regimes using the metachronal coordination of rotational oscillators. Using two-dimensional flexible flat-plates (i.e., flaplets) as the oscillating (beating) elements, a metachronal-wave pattern is experimentally proven to spontaneously emerge due to the hydrodynamic interaction among the oscillators. A mathematical model of the physical system is then developed for a better understanding of the coordination collective effects and for analysing its stability. The model can track the emerged coordination over long periods and estimate the net propulsive force acting on the physical model. The developed system is able to produce effective propulsion, that can be utilized in robotic applications, despite the time-symmetric beating profiles and the single degree-of-freedom actuation of the individual oscillators.

# Thesis Contributions

The present PhD thesis aims at researching two natural behaviours witnessed in biological fluidic organisms and exploring how these behaviours can be implemented in robotic solutions in fluids, using artificial mimicry tools and advanced imaging and computational techniques. In the following section, I provide a list of brief vindications on how this PhD thesis significantly contributes to the current state of research in nature-inspired mechatronics, bridging the gap between well-known biological abilities and applied mechanical systems.

Different contributions of this thesis can be classified into the following three categories:

## **1. Investigation of nature-inspired processes and capabilities**

### **(a) Understanding how the seal's whiskers are utilized for performing localization and tracking tasks**

Even blindfolded, the seal can localize and track its target underwater using its whiskers. Various studies have demonstrated these abilities of the seal while performing astonishing tasks using its mechanical transducers. Some studies have researched the behaviour of the whiskers and how they interact with the surrounding flow. However, the seal's perception of the whiskers' vibrations as useful localization information has not been fully understood yet. In this thesis, machine-learning models simulates how the seal's brain compares certain characteristics of the vibration signals of its whiskers in order to localize the source of the disturbance in the surrounding water.

### **(b) Examining how the spontaneous-synchronization of cilia is achieved**

By applying the clutch control hypothesis and introducing system flexibility, leading to the viscous-coupling of artificial cilia in an enlarged experimental model, the resemblance of metachronal self-coordination for symmetric 2D oscillating flaplets is achieved. The evolution stages of the coordination and its collective effect could be analysed by means of a simulation model and particle-image-velocimetry measurements.

**(c) Explaining how the metachronal coordination of symmetric oscillators can produce fluid propulsion**

A running metachronal wave at ciliated surfaces is crucial for increasing the efficiency of the directed propulsion of the surrounding fluid. In this thesis, it is demonstrated that the metachronal coordination of a row of oscillators with time-symmetric beating profiles (i.e., each can not generate propulsion on its own) provides the degree of asymmetry required to generate effective propulsion.

**2. Introducing novel biomimetic systems and discussing their applications in fluidic and robotic solutions**

**(a) Introducing a whisker-array sensor that uses learning models for localization tasks underwater**

Neural-network models are applied to an artificial sensor composed of a 3D printed head model and optical-fiber whiskers, and used for underwater two-dimensional position sensing of a wake-generating body.

**(b) Introducing a mechatronic system of flexible flaplets that uses metachronal coordination for generating fluid propulsion**

A system of five flapping oscillators, made of silicone rubber, is actuated using rotational motors to mimic the metachronal self-coordination of cilia. The system can successfully induce flow propulsion at low-Reynolds number in its coordinated state.

### **3. Presenting new methodological approaches that can be adopted in future research**

(a) **The use of computational-intelligence tools for the interpretation of the whisker-flow interaction and hydrodynamic sensing**

Analytical equations and numeric computations are often used to interpret the problems of fluid-structure interaction. Here, the use of deep learning is introduced to mimic and explore the behaviour of the whisker interaction with the surrounding disturbed flow, instead of using complicated analytical or numeric models.

(b) **The use of vision-based feedback control for the online implementation of the geometric clutch hypothesis that describes the ciliary gait cycle**

The recorded frames of a high-speed camera are processed online to identify the oscillator tips and control the motors so that the identified tips perform fixed-amplitude oscillations, implementing the geometric-clutch hypothesis.

# Chapter 1

## Introduction

Inspired by nature, from huge machinery to micro systems have been developed to solve complex problems around the globe. Engineers and roboticists often seek nature for sustainable and stable solutions to different challenges that face humanity. This approach of innovation is known as biomimicry. In short, it is the strategy of adopting nature-tested schemes and applying them to technological systems.

As it turns out day after day, living creatures are very good at what they are doing. Scientists are very happy to steal some of their evolutionary skills and implement them in a galaxy of clever machines that they design to turn our world into a better place. That is not to say that they would replicate their exact behaviour found in nature (good luck with that!). Instead, using artificial tools, they try to investigate different approaches how to achieve a form of solution similar to that witnessed in the natural behaviour. Nowadays, various tools that we witness and use in our everyday life are designed to mimic some features of animals or plants. They have shown impressive results in performing tasks more efficiently and a lot easier than ever.

That said, to replicate the precise natural behaviour is not always the best available option. Often, some features need to be altered so that the resulted product can better address the required functionality. A well-known example of that is the history of the aircraft development. At first, around 1490, humans tried to replicate the way birds fly by building forms of flapping wings that they can strap onto their arms (i.e., ornithopters). It was not until the early days of the twentieth century

when the first capable aircraft was built by the Wright Brothers. The design showed features such as propellers which was not witnessed in a natural flying bird before.

Examples of biomimetic devices are currently all over the place. To mention but a few, butterfly wings have inspired scientists to integrate bio-inspired nano-holes into light-harvesting cells to improve the efficiency of light absorption. The unique bump protrusions on the fins of whales have inspired the design of serrated-edge wind turbines which are reported to be much quieter and more efficient than turbines with smooth blades. Last but not least, the natural shock absorbers of the woodpeckers have inspired the creating of more shock-resistant flight recorders.

## **1.1 Motivations and research aims**

*1 In general, the investigation and understanding of the inspiring processes witnessed in nature would help to produce imitating solutions that are capable of achieving functionalities currently beyond our reach, serving humanity on many levels.*

In this thesis, I investigate two different behaviours witnessed in biological organisms that possess hair-like structures (i.e., cilia and whiskers) and live in fluidic environments using artificial mimicry tools. I then study the characteristic features of the developed artificial systems and how they can be utilized in relevant robotic solutions. A brief background about the topics covered in this thesis is introduced in chapter 2. In the following illustration, I build on the key concepts of these topics to conclude with the different motivations and aims of our present studies.

### **1.1.1 Biomimetic sensors for underwater surveillance**

Due to the diversified and significant contributions of underwater robotics in defence, security and commercial applications, the advancement in underwater navigation and surveillance systems is currently a trending research topic. The present sensing techniques used for underwater localization (e.g., vision and sonar) feature a wide range of drawbacks from the lack of stealth to the low energetic efficiency and the dangerous impact on the surrounding life (Griffiths 2002, Kinsey et al. 2006). Ac-

cordingly, scientists have been mining the marine life for safe and passive techniques of hydrodynamic sensing that can be used in the harsh aquatic environment.

*2 Exploring how marine animals navigate the underwater world, may reveal innovative sensing techniques that can assist or replace the current tracking and surveillance devices used in autonomous and non-autonomous underwater vehicles.*

### **1.1.2 Hydrodynamic sensing using artificial seal whiskers**

Neural systems within living creatures accomplish a unique job in the perception of external stimuli and their interpretations as useful information. For example, the visual and auditory cortices translate the perceived light or sound vibrations into recognizable faces, objects and sounds. Inspired by the brain's interpretation abilities, artificial neural-models have been widely utilized for facial and speech recognition in security, e-learning, scientific and entertainment purposes.

Pinnipeds such as seals and sea lions possess a remarkable ability of hydrodynamic detection using their facial mechanoreceptors – known as whiskers. Up till now, it is not entirely clear how the vibrations of whiskers (due to the surrounding fluid movements) are interpreted in the brain for underwater navigation (e.g., as locations of preys or objects). The reader is referred to section 2.1.1 and 2.1.2 for an overview about biological whiskers and their uses in mammals for tactile sensing and hydrodynamic detection.

*3 The design of a localization sensor based on spatially-distributed whisker-like transducers has not been attempted yet. Emulating the whisker-trigeminal system of seals using machine learning would allow us to translate the underwater flow disturbances, encoded in the vibrations of artificial whiskers, to information about the hydrodynamic trails and the location of their sources.*

### **1.1.3 Emergence of metachronal coordination in experiment**

We know that motile cilia (e.g., in human windpipes, on the surface of locomoting cells such as Paramecium, etc.) often beat in coordinated patterns forming traveling metachronal waves (described in section 2.2.1). In these patterns, individual

cilia appear to be controlled simultaneously so that they maintain certain phase relationships during their beating (as if a cilium is aware of the configurations of its neighbours' beats). A while ago, it had been initially believed that the cilia coordination was controlled by a neuroid mechanism (Sleigh 1963, 1968, Kinoshita & Murakami 1967). Later investigations of biological ciliated organisms, however, showed that the metachronal coordination depend on the hydrodynamic interactions between neighbouring cilia (Machemer 1974, Sleigh 1974, TAMM 1973). Many studies had experimentally demonstrated (for example by restricting the movement of some cilia in the middle) that biological cilia lose their coordination when the viscous coupling among them was interrupted (Tamm 1983, 1984). However, much less was discovered about the build-up stage of the synchronization and whether this type of coordination (i.e., metachronal waves) can emerge for different and more simple shapes of artificial cilia.

*4 Resembling self-coordination in experiment among cilia-like oscillators starting from a chaotic phase pattern would be helpful to test the conditions and control hypothesis that are necessary for the self-coordination to rise by viscous coupling. It would also help to examine the coordination's build-up stage as the interaction among the beating elements takes place.*

More recent studies have established that the synchronized behaviour of cilia is nothing but a spontaneous form of hydrodynamic cross-talk among them that arises from the nature of the viscous (low-Reynolds) environment they are in and the conformation of their own characteristic beats (Golestanian et al. 2011, Brumley et al. 2014). Numerical simulations, that resembled the unique asymmetric beating of cilia with oscillation profiles that were fairly similar to those of natural cilia, have shown the evolution of metachronal waves (an example is illustrated in section 2.2.4), sometimes with breaks in coordination at different stages (Niedermayer et al. 2008, Elgeti & Gompper 2013). In experiment, such replication of the beating profiles of cilia is complicated to achieve, due to the shape control of the beating elements required through different stages of their oscillations (the reader is referred to the background introduced in section 2.1.1 for more information about the motion of biological

cilia). Therefore, experiments that tried to prove the emergence of hydrodynamic synchronization have used simple structures, such as colloidal spheres, as rotating or oscillating elements in the viscous medium (Kotar et al. 2010, Di Leonardo et al. 2012). However, up to now simple two-dimensional shapes like flaplets (i.e., thin rectangular flat plates) have not been studied for their possible self-coordination. Additionally, the hitherto known experiments using colloidal elements could not examine the evolution of the collective effects of self-coordination and whether or not it could result in the emergence of effective flow propulsion. To sum up, most of the studies that paid attention to the emergence of self-synchronization were numerical. The few experimental studies used elements (e.g., colloidal spheres) that could not highlight the collective effects of the synchronization on the beating system and its surrounding fluid.

*5 2D artificial cilia such as flaplets have not yet been tested for their possible self-coordination. The flapping oscillators would be more cilia-like than the beating elements used in the previous experiments of self-synchronization. The resulted pattern of coordination would also be better comparable to the metachronal wave witnessed in natural cilia.*

#### **1.1.4 Propulsion as a result of spontaneous coordination**

*6 The development of micro- and nano-scale robots that are able to generate propulsion in viscous environments is one of the most appealing topics of modern research. Further innovation in the micro-swimmer field is motivated by the significant potential of these devices in biomedical applications such as minimally invasive procedures and drug-cell delivery.*

Metachronal coordination is believed to play an important role in inducing a directed transport at the surface of beating cilia. Recently, synchronization was imposed among ciliated walls by controlling a row of pneumatic-actuators to have a coordinated pattern of oscillations (Rockenbach et al. 2015). It was demonstrated that metachronal coordination could help the beating system achieve directed propulsion. In addition, for a model of artificial magnetic-controlled cilia, it was shown that the

imposed metachronal coordination increases the transport performance in the flow significantly (Gauger et al. 2009). Although, these studies highlighted the propulsion effect of metachronal coordination, they used asymmetric actuation of the individual cilia to achieve preliminary low-Reynolds propulsion (illustrated in section 2.2.5). It would be interesting to examine if the metachronal coordination is sufficient to solely give rise to propulsion even for symmetric actuation of oscillators. The metachronal coordination itself, presented in the uni-directional running surface wave, can introduce the beating asymmetry required for propulsion at low Reynolds numbers. Moreover, the previous studies did not examine the propulsion emergence stages as the coordination is formed from chaos. The coordination of cilia in former studies were controlled by external systems (e.g. pneumatic systems, magnetic fields) that are difficult to utilize for embedded micro-swimmer applications. Developing cilia-like systems that use the viscous environment to spontaneously achieve propulsion would facilitate the embedded-control of individual oscillators independently using conventional rotary actuators.

*7 Scalable beating systems, that implement time-symmetric rotational (single-degree-of-freedom) actuation of their oscillators and use self-coordination to generate flow propulsion, have not been realized nor investigated yet. They would be prime candidates for micro-swimmer applications and propulsion devices at low Reynolds numbers due to their time-symmetric and easy-to-control beating profiles as well as the possibility to actuate them using embedded rotary motors.*

*8 Monitoring the internal states of the flapping oscillators (i.e., the forces acting on the flaplets during their beating) experimentally or via a validated mathematical model would facilitate the investigation of the gradual build-up of the coordination collective role (i.e., effective propulsion) while the metachronal coordination is rising. It would also help identify the effect of small changes of the phase-relationships among the oscillators on the resulted propulsion.*

## 1.2 Thesis outline

This thesis is structured in the prospective-publications format. During my doctoral research period, I have mainly conducted three studies that have been published as journal peer-reviewed research articles of which I am a first author. In this thesis, the three studies are included in separate chapters (Chapter 3, 4 and 5). Each study is structured as follows: (i) Abstract; (ii) Introduction, containing a brief literature review of the previously-conducted work related to the study and describing how it clearly stands out. Here, any specific hypotheses being tested are usually highlighted (sometimes the objective is included separately); (ii) Materials and Methods, containing important material considerations, the experimental setup, and the mathematical model if exists (sometimes this part is exploded into multiple sections instead of one); (iii) Results and Analysis: containing a precise description of the experimental or model results as well as their detailed interpretations; (iv) Discussion and/or Conclusions, expanding on the analysis of the study findings as well as highlighting the study's conclusions. Future research directions may be also mentioned here. Appended to each of these chapters, a critical analysis of the study is presented where the study's contributions and raised issues are thoroughly discussed. Additional results may be also included at the end of each chapter.

Chapter 2 contains a theoretical background of the key terms and topics that are discussed or used in the following studies. This chapter along with the introduction sections of the following three chapters form a coherent literature review of the thesis work.

### List of Publications

- Elshalakani, M., Muthuramalingam, M., and Bruecker, C. (2020), 'A Deep-Learning Model for Underwater Position Sensing of a Wake's Source Using Artificial Seal Whiskers', *Sensors* **20**(11), 3522. – Published: 22 June 2020
- Elshalakani, M. and Brücker, C. (2020), 'Simulation of self-coordination in a row of beating flexible flaplets for micro-swimmer applications: Model and

experiment study', *Journal of Fluids and Structures* **94**, 102923. – Published: 29 February 2020

- Elshalakani, M. and Brücker, C. H. (2018), 'Spontaneous Synchronization of Beating Cilia: An Experimental Proof Using Vision-Based Control', *Fluids* **3**(2), 30. – Published: 25 April 2018

# Chapter 2

## Background

This chapter introduces the fundamental background of the research topics covered in this thesis in order to familiarize the reader with the key terms used in the presented studies. The reader is referred to the introduction sections of the following chapters for a concise literature review of the previous experimental and numerical studies related to the presented work.

### 2.1 Study one

#### 2.1.1 Whiskers as tactile sensors

Whiskers or vibrissae are mammalian hairs that are usually characterized by their long length. They typically grow around the nose and above the lips and eyes of mammals and act as touch (tactile) sensors. The way they work as sensors can be illustrated as follows: (i) as they brush or touch a near-by object or a surrounding medium, the details and movements of the touched surface is translated into whiskers' movements. (ii) hundreds of nerve cells located in the hair follicle can transduce detailed information about the motion of each whisker. (iii) the whisker-trigeminal system relays the transduced signals to the brain where they are interpreted as information about the touched object or medium. That said, the role of whiskers is still an active area of research. So far, whiskers have been shown to contribute to many functions such as: localization of food (preys), detection of surrounding movements, shape and texture recognition, navigation, locomotion,

maintenance of equilibrium, and swimming (Prescott et al. 2011).

### 2.1.2 Marine mammals and hydrodynamic detection

Pinnipeds possess a set of well-developed whiskers with up to 1500 nerve cells inside each whisker follicle. They use these facial sensors to detect water movements and hence navigate their surrounding environment. Various studies have demonstrated the ability of harbour seal to track the hydrodynamic trails in water (i.e., disturbances generated by fish, another seal or pilot submarines) using its whiskers. A control experiment was performed by Dehnhardt et al. where the movement of the seal's whiskers had been impeded. It was proven that the seal cannot detect the water disturbances nor perform tracking tasks without the use of its whiskers (Dehnhardt et al. 2001). Fig. 2.1 shows a blindfolded seal in another experiment while tracking the path taken by another trail-generating seal after it had left the water (Schulte-Pelkum et al. 2007). In approximately 90 percent of the trials, the seal could identify and follow the pilot's path successfully (sometimes with undulatory deviations to both sides).

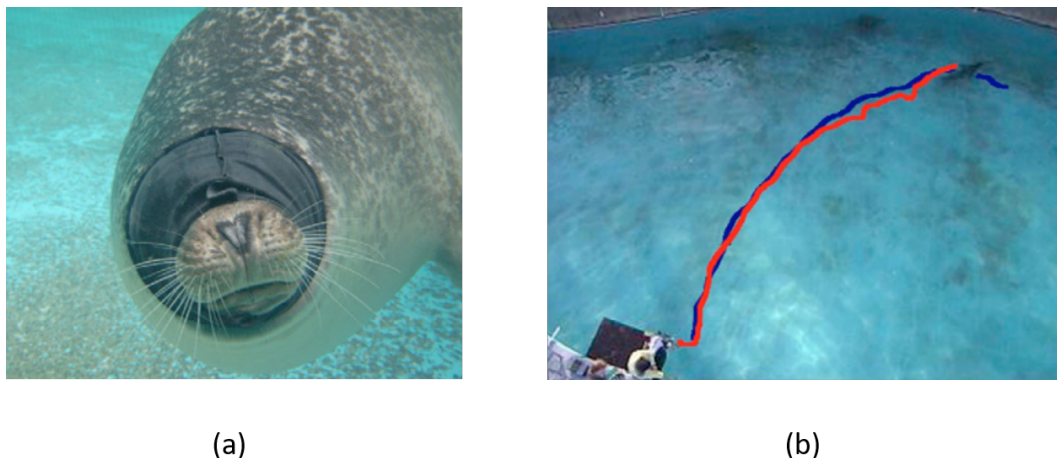


**Figure 2.1:** Experiment of harbour seal tracking a hydrodynamic wake generated by another pilot seal; from (Schulte-Pelkum et al. 2007). (a) the trail-tracking seal while blindfolded detects the swimming direction using its whiskers. (b) the path followed by the seal (red line) in approximately 60% of the performed trials while tracking the pilot's path (blue line). In most of the remaining trials, the seal could also follow the path successfully but with some undulatory deviations from the original path.

Unlike rodents, pinnipeds keep their whiskers steady while sensing the underwater disturbances and hence maximizing their detection ability (Murphy et al. 2013).

Usually, Pinnipeds’ whiskers have an elliptical cross-section that is tapered towards the whisker tip. Harbor seals, however, possess a unique undulated design of the cross-section along the whisker’s shaft that is different from the smooth whisker of the California sea lions (see Fig. 2.5) (Murphy et al. 2013). This design was found to have a higher signal to noise ratio than that of the smooth one (Hanke et al. 2010).

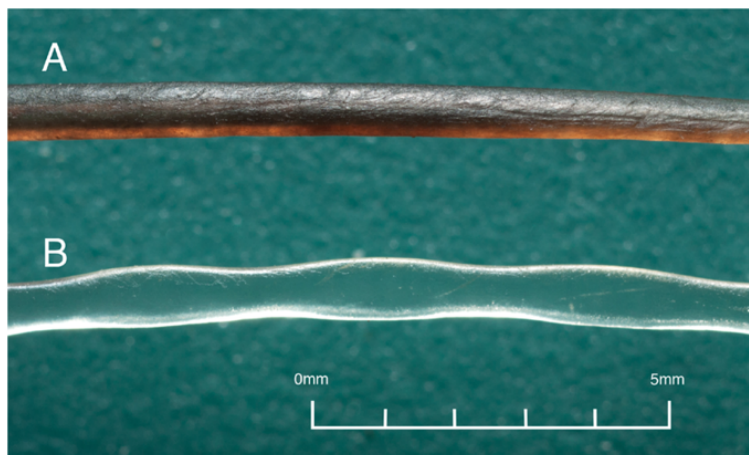


**Figure 2.2:** Outer surfaces of two whiskers that belong to a California sea lion (top) and the Harbor seal (bottom); from (Murphy et al. 2013).

### 2.1.3 Whisker-inspired robotic sensors

Robotic e-whiskers have been implemented in various engineering systems for active and passive sensing. Herein, we present some of these applications and highlight the functionality of the used whisker-type sensors. In 2011, Sullivan et al. used an active array of artificial rat-whiskers to recognize three different surface textures (Sullivan et al. 2011). Fig. 2.6a shows the sensor while integrated on a robotic arm for accurate and robust manipulation of its location in the 3D space. The deflections of the whiskers’ shafts while brushing the different surfaces are measured used instrumentation at their base. Using the gathered data, different classifiers were trained to distinguish the texture of each surface. The work concluded that artificial active whiskers could be successfully used as robotic tactile sensors. Other studies have utilized whisker-type tactile sensors for shape-recognition and texture-identification tasks (Kim & Möller 2007, Pearson et al. 2011, Lepora 2016).

The use of artificial whiskered sensors in the aquatic environment has focused on experimenting the sensitivity limits of these structure in the detection underwater disturbances. The observation of the undulated cross-section of the seal’s whisker has inspired a design of artificial whisker-like sensors whose resonant frequency can be tuned to suppress unwanted environmental noise (y Alvarado et al. 2012). Eberhardt et al. developed a wake-detection sensor, shown in Fig. 2.6b, using an array of artificial whiskers whose vibrations could be related to the trail of a pilot submarine (Eberhardt et al. 2016). Recently, an experimental study revealed that the vibrations of artificial whiskers while interacting with an underwater flow disturbance could decode the shedding frequency of a Kármán vortex street (Muthuramalingam & Bruecker 2019).

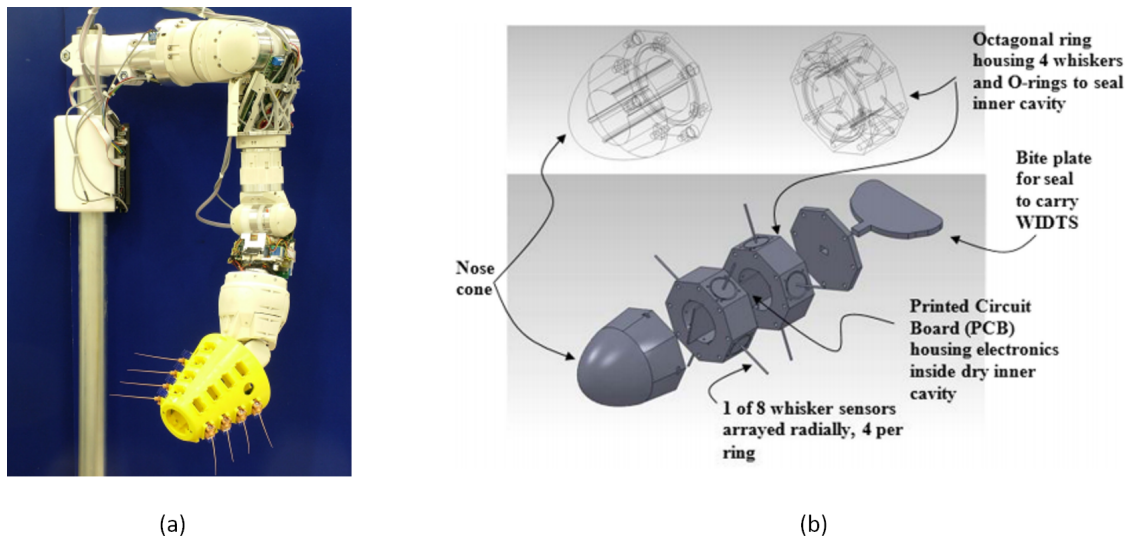


**Figure 2.3:** E-whisker sensors used for active and passive sensing in robotic applications; (a) artificial rat-whisker array attached to a robotic manipulator and used for texture classification of different surfaces; from (Sullivan et al. 2011); (2) wake-detection system composed of 8 artificial whiskers that can identify and track the trail of a pilot submarine; from (Eberhardt et al. 2016).

Previous experiments that showed the seal’s abilities to track surrounding objects in the aquatic environment (e.g. fish, submarines or other seals) using its whiskers as well as the previous implementations of whisker-inspired underwater sensors form the basis for the first study presented in chapter 3 of this thesis.

### 2.1.4 Key questions addressed by the present research

The research presented in this study aims at providing adequate answers to the following unknown research questions:

**Research question 1:** How does the seal’s brain interpret the surrounding water disturbances as useful information for navigation and tracking?

**Research Question 2:** To what extent can the vibrations of flexible elements in response to a body’s wake underwater encode information about the location of that body?

**Research question 3:** Can artificial neural-networks mimic the whisker-trigeminal system accurately-enough to be used in engineered applications for underwater sensing?

### 2.1.5 Relevant previous studies

Table 2.1 summarizes the key studies highlighting the previous attempts to produce whisker-type systems for robotic applications. The studies are classified according to their publication date, the presented whisker-like device and its main utilization.

## 2.2 Study two and three

### 2.2.1 Cilia and metachronal coordination

Covering most of the human body’s cells and the surface of many cellular organisms are microscopic hair-like structures known as cilia (length  $2 \sim 12 \mu m$  (Bottier et al. 2019)). Previously, they were thought of as some kind of vestigial remnants that hardly play any role in biological processes. It was not until the last few decades that the contributions of cilia began to be partially recognized (Marshall 2013). Nowadays, the importance of cilia continues to be acknowledged further as many illnesses are being associated with their dysfunction. Several medical conditions -

**Table 2.1:** Previous studies on whisker-like devices in engineering applications.

year	reference	whisker-type device	usage
2006	(Kim & Möller 2007, Lepora 2016)	active-whisking platform based on rodent whiskers	shape discrimination
2011	(Sullivan et al. 2011)	robotic manipulator with artificial rodent whiskers	texture recognition
2012	(Beem et al. 2012)	artificial seal whisker with undulated cross-section	flow velocity sensing
2008	(Eberhardt et al. 2016)	torpedo-shaped sensor based with artificial seal whiskers	wake detection
2017	(Zhuang et al. 2017)	neural-network driven model based on rodent whiskers	shape recognition
2019	(Muthuramalingam & Bruecker 2019)	artificial whisker-array distributed on a pinniped head model	vortices frequency detection

known as ciliopathies - such as respiratory infections, kidney disease and infertility have been proven to be triggered by defects in cilia (Waters & Beales 2011).

Motile cilia possess the ability to move the surrounding fluid in a certain direction which plays an essential role in the locomotion of sperms and sweeping dirt and mucus outside of the lungs (Brokaw 1975, Fulford & Blake 1986*a*). A motile cilium perform cyclic motion triggered by interactions of its composing microtubules, that consists of repeating beat cycles. A single cycle is composed of two asymmetric strokes; i.e., power stroke and return stroke. The ability of an individual cilium to generate a fluid flow is essentially due to the asymmetry of its beating strokes. Fig. 2.4a highlights different phases during the two strokes of a cilium’s beat. If the beat of an individual cilium were time-symmetric, the scallop theorem suggests that the net displacement of its surrounding fluid would vanish (Purcell 1977). The switching moment between power and recovery strokes is constrained by a mechanical (stress) feedback in a biological cilium. Yet, Lindemann proved in what is known as the geometric clutch hypothesis that mechanical stresses and geometrical configuration of the cilia are coupled parameters and hence, the geometric feedback condition is a simple way to represent how a cilium sense the moment to switch between the two strokes (Lindemann 1994, 2007).

Cilia often beat in groups while maintaining a certain phase shift among adjacent neighbours forming a pattern known as a metachronal wave. A schematic resemblance of this pattern is shown in Fig 2.4b. Similar patterns of coordinated cilia are witnessed in human tissues (e.g., brain and lungs) and on the surface of swimmer organisms such as ciliates (e.g., Paramecium) and Ctenophora (e.g., Pleurobrachia). The metachronal coordination was shown to have a significant role in the generation of the steady-streaming transport of the surrounding fluid (Gauger et al. 2009, Bruot & Cicuta 2016). In the work presented in this thesis, it is proven that the metachronal coordination introduces a different degree of asymmetry to a beating system of cilia-like flaplets even if the individual beating elements perform time-symmetric beat profiles and cannot induce propulsion while beating separately.

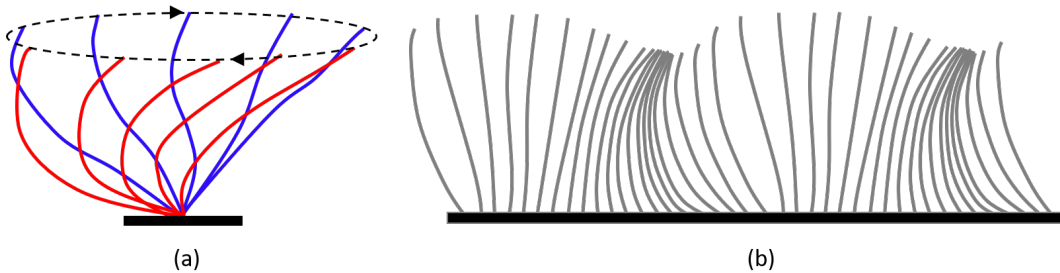


**Figure 2.4:** Schematic representation of the periodic motion of cilia: (a) different phases of a beat cycle of a single cilium where the power and return strokes are highlighted in blue and red respectively. The dash line highlights the path undertaken by the cilium's tip during the cycle; (b) a metachronal wave formed by a group of beating cilia.

## 2.2.2 Dynamical similarity

Navier-Stokes equation (Tritton 2012) is the basic formula that describes Newton's second law of motion for an incompressible fluid. The non-dimensionalized form of the equation can be written as:

$$\frac{\partial u'}{\partial t'} + u' \cdot \nabla u' = \frac{1}{Re} (\nabla'^2 u' - \nabla' p') \quad (2.1)$$

$$Re = \frac{\rho U L_c}{\mu}, \quad \nabla \cdot u = 0$$

where  $u, p$  velocity and pressure fields of the fluid respectively, the prime superscript refers to a dimensionless quantity,  $t$  is time,  $Re$  is the Reynolds number,  $\mu$  is the

fluid's dynamic viscosity,  $\rho$  is the fluid's density,  $L_c$  is the characteristic length and  $U$  is the speed scale selected for the given problem.

By examining the equation, one can realize that  $Re$  is the only parameter that survived its normalization. Therefore, a correspondence can be created between problems that have different length and speed scales but have similar  $Re$ . This correspondence is known as dynamical similarity (Batchelor & Batchelor 2000). It enables us to use the results of an enlarged experiment to investigate an observation that happens at a much smaller scale.

### **2.2.3 Emergence of assembly**

There is no such thing as a master ant that controls the organization of an ant colony. An ant makes use of its own receptors and surroundings so that it can automatically play an effective role in the group (Beckers et al. 1989). By keeping track of the perceived information, an ant's brain is chemically programmed to perform a group-missing task and hence colonies of smart-acting ants are developed (Allan et al. 1996). The rise of a collaborative behaviour due to individual body reactions and surrounding environment properties with no central control involved is called emergence.

Emergence is anything that once composed becomes more than the sum of its parts. It results in the synergistic integration of individual parts when brought together and act as a unit. That said, emergence can be noticed on many scales. Humans when brought together form societies that have their own set of rules and dynamics. On a tiny scale, water molecules that are relatively close to each other interact under a specific set of rules giving birth to "witness" which is not a property of a single water molecule (Ball 2013). Similarly, the metachronal wave pattern of cilia is believed to spontaneously emerge due to the hydrodynamic forces in the viscous environment. A mechanical resemblance of this emergence phenomenon is presented in the second study of this thesis.

## 2.2.4 Hydrodynamic synchronization

Hydrodynamic synchronization is when the kinetics in a fluid cause a set of relatively-close moving bodies to affect each other's kinematics and finally have a coordinated pattern of motion (e.g., in speed, phase, direction, etc.). Several models have demonstrated the spontaneous emergence of hydrodynamic organization for bodies with different shapes that are moving in viscous environments. Herein, light is spotted on two of these examples as well as some of their key findings. The first is a numeric model that is developed to mimic the beating of natural cilia and demonstrate how a metachronal wave (MW) rises from an uncorrelated beating pattern (Elgeti & Gompper 2013). Cilia were modelled as active rods that simulate the beating of Paramecium and the surrounding fluid environment was modelled using multi-particle collision dynamics (MPC). After approximately 130 cycles of beating, the modelled cilia formed a MW-like beating pattern that possessed some minor defects as shown in Fig. 2.5a. The model also studied the dependence of the fluid velocity on the cilia spacing. It was revealed that the transport velocity of the surrounding fluid increased as the cilia spacing decreased.

The second study is an experiment that was performed in the Cicuta laboratory using two colloidal spheres (Kotar et al. 2010). By implementing the geometric clutch hypothesis, the spheres are controlled using optical tweezers to have fixed amplitude oscillations. The experiment demonstrated that with the help of the viscous coupling between the oscillating spheres, a phase-lock is achieved between their oscillations in an out-of-phase configuration. A microscopic view of the spheres as well as the position trajectories of their centres are plotted in Fig. 2.5b.

## 2.2.5 Low-Reynolds swimmers

For biological and robotic swimmers with micro scale sizes (i.e., micro-swimmers), the effect of inertial forces is suppressed compared to that of viscous forces; resulting in a low  $Re$ . By examining Eq. 2.1 further, one can notice that as  $Re$  gets smaller (less than one), the left-hand side terms gradually become less significant and can

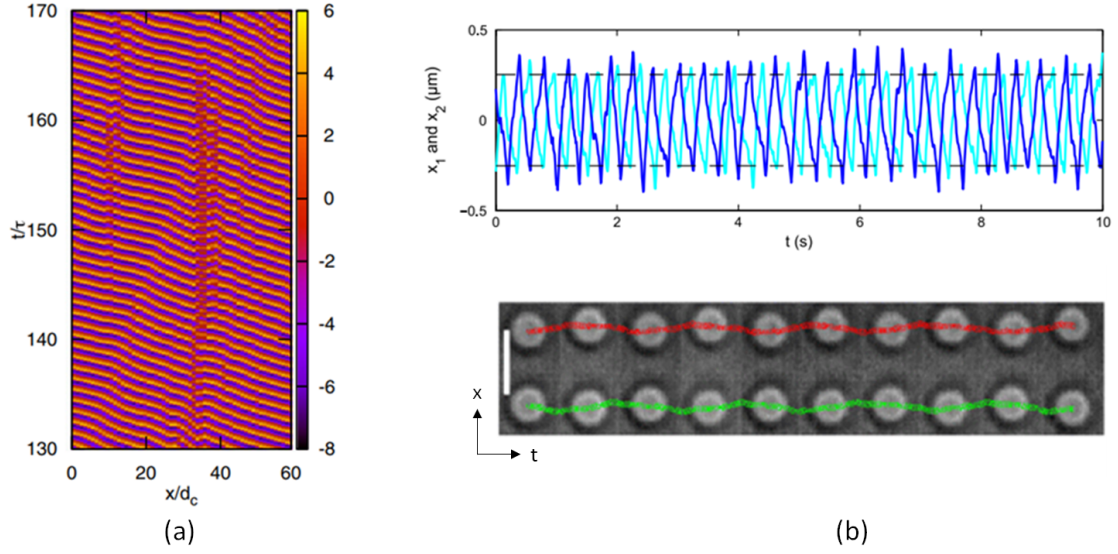


**Figure 2.5:** Emergence of hydrodynamic synchronization at low Reynolds numbers; (a) model of cilia arrays self-assembly in metachronal waves; from (Elgeti & Gompper 2013); (b) anti-phase synchronization of oscillating colloidal spheres; from (Kotar et al. 2010).

be neglected at  $Re \ll 1$ ; simplifying the equation to the linear Stokes equations:

$$\mu \nabla^2 u - \nabla p = 0, \quad \nabla \cdot u = 0 \quad (2.2)$$

Due to the linearity and time-invariance of the Stokes equations, it was proven that for a body in a fluid, whose dynamics are described by the Stokes equations, moving through a sequence of configurations  $C(t)$ , the locomotion of the body and the propulsion of its surrounding fluid do not depend on the speed of the performed sequence. Herein, each point  $C$  in the configuration space represents the positions of all points on the surface of the body at that instance in time  $t$ .

The proof can be outlined as follows:

- we know from applying the reciprocal theorem to the linear low-Reynolds problem that the swimming (propulsion) speed  $U$  can be directly related to the beating gait  $\dot{C}(t)$  of the swimmer (Stone & Samuel 1996)

$$U = \iint_S \dot{C} \cdot g(C) dS \quad (2.3)$$

in which  $S$  is the instantaneous boundary of the swimming object and  $g$  is

some general function that depends on the instantaneous gait configuration.

- the net displacement of the swimmer between  $t_1$  and  $t_2$  can be calculated by the integral

$$\Delta X = \int_{t_1}^{t_2} U dt = \int_{t_1}^{t_2} \iint_S \dot{C} \cdot g(C) dS dt \quad (2.4)$$

- from there, if we consider another swimmer with a speed  $U'$  that undertakes the same gait configurations but with a different rate, we give that different-rate gait the notation  $C(\tau)$  with  $\tau = f(t)$ , then we have

$$U'(\tau) = \iint_S \frac{dC}{d\tau} \dot{\tau} \cdot g(C(\tau)) dS \quad (2.5)$$

- we choose the temporal points  $t_3$  and  $t_4$  in the second swimmer's gait to have the same configuration as the points  $t_1$  and  $t_2$  in the first swimmer's gait; such that  $\tau_1 = f(t_3) = t_1$  and  $\tau_2 = f(t_4) = t_2$ . The net displacement of the second swimmer between  $t_3$  and  $t_4$  can be calculated by the integral

$$\begin{aligned} \Delta X' &= \int_{t_3}^{t_4} U' dt = \int_{t_3}^{t_4} \iint_S \frac{dC}{d\tau} \dot{\tau} \cdot g(C(\tau)) dS dt \\ &= \int_{\tau_1}^{\tau_2} \iint_S \frac{dC}{d\tau} \cdot g(C) dS d\tau \\ &= \Delta X \end{aligned} \quad (2.6)$$

A consequence of this property of the Stokes flow is the so-called scallop theorem. It states that if a body in a fluid, whose dynamics are described by the Stokes equations, undergoes a periodic cycle of configurations and the time-reversed sequence of the configurations cannot be distinguished from the original sequence, the body cannot produce net propulsion.

Purcell firstly introduced the theorem in 1977 where he stated that in order for a body to generate fluid propulsion by cyclic motion, the time-reversed sequence of a cycle needs to be different from the original (Purcell 1977). He suggested a three-link swimmer that would follow a straight line in Stokes flow and was investigated later

by Becker et al. in 2002. The model possesses two moving rods; each on its own performs a reciprocal motion. However, the geometrical sequence of the swimmer as a whole is not time-symmetrical (Fig. 2.6a) (Becker et al. 2003). Other micro-swimmer designs have been utilizing Purcell’s arguments to generate propulsion at low Reynolds numbers. Nasouri et.al. introduced a model micro-swimmer composed of two spheres linked by a rod that changes its length in a periodic manner (Fig. 2.6b). One of the spheres was modelled as a hyperplastic solid that introduced the required non-reciprocal pattern of deformations (Nasouri et al. 2017). Another example was realized by Gao et al. of a helical micro-swimmer that was controlled by an external rotating magnetic field (Gao et al. 2014). The rotation direction of the helix controls the direction of resulted propulsion (Fig. 2.6c). The reader is referred to Lauga’s review article (Lauga 2011) for more examples of synthetic swimmers at low Reynolds numbers.

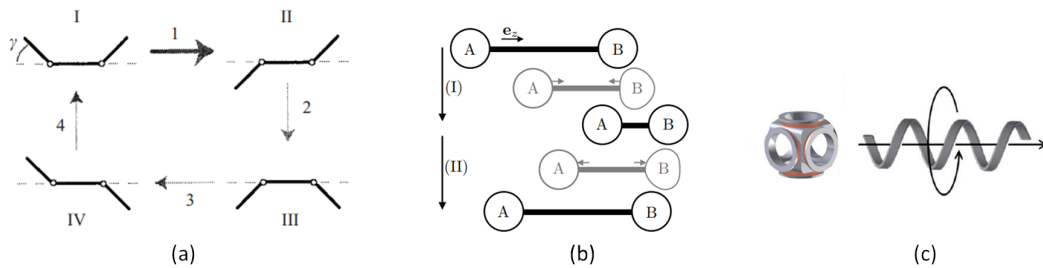


**Figure 2.6:** Schematics of numerical and experimental examples of micro-swimmer models. (a) gait cycle of the Purcell’s three link swimmer; from (Becker et al. 2003); (b) model of a linked two-sphere swimmer that can be actuated using optical tweezers; from (Nasouri et al. 2017); (c) realization of a magnetic-field-actuated helical micro-swimmer whose structure is derived from different plants; from (Gao et al. 2014).

## 2.2.6 Key questions addressed by the present research

The presented research herein aims to provide adequate answers to the following unknown research questions:

**Research question 1:** Can the metachronal self-coordination of cilia be replicated using simple shapes like 2D flaplets?

**Research question 2:** To what extent does the geometric clutch hypothesis play a role in the cross-talk among adjacent oscillators in viscous environments?

**Research question 3:** What are the conditions necessary for oscillators (not necessarily performing cilia-like profiles) to undergo hydrodynamic synchronization?

**Research question 4:** Can the metachronal coordination of oscillators with time-symmetric beat profiles produce net propulsion?

### 2.2.7 Relevant previous studies

Tables 2.2 and 2.3 present the key relevant studies that demonstrated the previous attempts of producing propulsion devices at low-Reynolds regimes and investigating the hydrodynamic synchronization of artificial and model cilia. In Table 2.2 the studies are classified according to their publication date, the main material of the propulsion device and the actuation method of the produced mechanism. In Table 2.3, the studies are classified according to their publication data, type (experimental or numerical) and the key finding or feature.

**Table 2.2:** Previous studies on micro-swimmers and propulsion devices at low-Reynolds numbers.

<b>year</b>	<b>reference</b>	<b>substantial material</b>	<b>actuation</b>
<b>2007</b>	(Kosa et al. 2007)	piezoelectric beams	electric filed
<b>2007</b>	(Evans et al. 2007)	PDMS	magnetic field
<b>2011</b>	(Kokot et al. 2011)	superparamagnetic beads (Dynabeads Epoxy M-450)	magnetic field
<b>2014</b>	(Gao et al. 2014)	plant vessels	magnetic filed
<b>2015</b>	(Rockenbach & Schnakenberg 2015, Rockenbach et al. 2015)	PDMS	pneumatics
<b>2016</b>	(Kim et al. 2016)	polymer IP-Dip	magnetic field
<b>2019</b>	(Ren et al. 2019)	polymer IP-Dip	acoustic field

**Table 2.3:** Previous studies on the self-coordination of artificial and model cilia.

<b>year</b>	<b>reference</b>	<b>type</b>	<b>key feature</b>
<b>2003</b>	(Kim et al. 2003)	experiment	bundling process of macroscopic scale flagella
<b>2010</b>	(Kotar et al. 2010)	experiment	out-of-phase lock of two oscillating colloidal spheres actuated by optical tweezers
<b>2014</b>	(Di Leonardo et al. 2012)	experiment and numerical simulation	synchronization of two mesoscopic rotors actuated by light and radiation pressure
<b>2008</b>	(Niedermayer et al. 2008)	numerical simulation	synchronization of spherical beads using a phase-oscillator model
<b>2013</b>	(Elgeti & Gompper 2013)	numerical simulation	formation of metachronal waves in a mesoscopic model of 2D cilia arrays
<b>2019</b>	(Chakrabarti & Saitillan 2019)	numerical simulation	phase synchronization of a couple of beating filaments

# Chapter 3

## A Deep-Learning Model for Underwater Position Sensing of a Wake's Source Using Artificial Seal Whiskers

### Abstract

Various marine animals possess the ability to track their preys and navigate dark aquatic environments using hydrodynamic sensing of the surrounding flow. In the present study, a deep-learning model is applied to a biomimetic sensor for underwater position detection of a wake-generating body. The sensor is composed of a bundle of spatially-distributed optical fibers that act as artificial seal-like whiskers and interact with the body's wake in the form of time-variant (bending) deflections. Supervised learning is employed to relate the vibrations of the artificial whiskers to the position of an upstream cylinder. The labeled training data are prepared based on the processing and reduction of the recorded bending responses of the artificial whiskers while the cylinder is placed at various locations. An iterative training algorithm is performed on two neural-network models while using the 10-fold cross-validation technique. The models are able to predict the coordinates of the cylinder in the two-dimensional (2D) space with a high degree of accuracy. The current implementation of the sensor can passively sense the vortex-street wake generated by the cylinder and estimate its position with an average error smaller than the characteristic diameter  $D$  of the cylinder and for inter-distances (in the water tunnel) up to 25-times  $D$ .

## 3.1 Introduction

According to the market research report presented in (*Underwater Robotics Market Size* 2018), the size of the underwater robotics market was estimated at USD 2.52 billion in 2017, which represented about 7.6 per cent of the global robotics market size. With water covering about 71 percent of the earth's surface, underwater robotics has allowed for a broad range of applications in military, commerce, and science. Generally, the robot's perception of its surrounding environment is essential for performing tasks, avoiding risks, and navigation. With the help of surveillance sensors, robots can explore the unknown offshore world securely, despite the hazardous and unpredictable underwater environment. However, further progression in the development of navigation and object-tracking sensors faces a variety of technical challenges (Leonard et al. 1998, Griffiths 2002, Kinsey et al. 2006).

Mostly, vision and sonar systems have been used for underwater surveillance. However, both techniques feature some serious drawbacks. Firstly, vision-based sensors are known for their limited perceptible range, which confines the use of cameras to the near surrounding space. The absorption and scattering of light cause the underwater environments to be muddy and cloudy, which results in images that can hardly be featured (Kröger 2008, Lee et al. 2012). Additionally, an artificial source of light energy is required in order to use a vision-based underwater sensor due to the low level of natural illumination in the deep water (Yang et al. 2006). Similarly, the transmission of acoustic waves is required for a sonar system to estimate the location of the objects in the surrounding space (Akyildiz et al. 2004). Because both of the techniques perform active sensing, the location of the emitter is revealed, while a high level of stealth is often required in surveillance applications. On another hand, sound emissions have been declared to be life-threatening to many marine animals. Schrope, M. reported several death cases of beaked and minke whales due to the emissions of the sonar systems used by the US Navy (Schrope 2002). Finally, the energetic efficiency of both techniques is questionable. It has been shown that the use of sonar sensing in a small autonomous-underwater-vehicle (AUV) leads to significant inflation of the total consumed power (Akyildiz et al. 2004).

Marine life is full of examples that can be studied to mine for new techniques that can help to overcome the current challenges of underwater sensing. Fish and marine animals demonstrate the ability to use their passive mechanical sensors for object-detection and navigation under water, even with a partial or full lack of both visual and bio-sonar. The blind cavefish is able to swim at high-speeds while avoiding collisions with nearby objects. This fish developed the ability, known as hydrodynamic imaging, to blindly sense the motion of water and recognize the surrounding objects due to the usually-dark environment where it lives (Windsor et al. 2008, Von Campenhausen et al. 1981, Montgomery et al. 2001). Pinnipeds (such as sea lions and seals) have the ability to detect water disturbances using their facial mechanoreceptors, known as whiskers. They can use the acquired information to navigate the surrounding environment, identify certain objects, and track their preys. Hanke et al. demonstrated that the hydrodynamic trail of some preys remain detectable in water for several minutes (Hanke et al. 2000, Hanke & Bleckmann 2004). This gives Pinnipeds the ability to track far targets that can hardly be detected by vision. It was experimentally shown that the Harbor seal can follow the path undertaken by a submarine, even with an inter-distance of about 40 m (Dehnhardt et al. 2001). It was also able to detect the direction of the submarine's wake even with a 90° encountering angle. A control experiment was conducted under the same conditions after the motion of the tracking seal's whiskers had been impeded. In this experiment, it was proven that the seal cannot detect the submarine's wake without its whiskers. In another study, a blindfolded Harbor seal was able to follow the hydrodynamic trail generated by a pilot seal after it had left the water (Müller & Kuc 2007). Harbour seals were also capable of detecting sinusoidal vibrations in water with speeds that ranged from 0.245 to 1.8 mm·s<sup>-1</sup> and frequencies ranging from 10 to 100 Hz (Dehnhardt et al. 1998). Last but not least, seals were also found to be capable of distinguishing sizes and shapes of objects by sensing their hydrodynamic wakes (Wieskotten et al. 2011).

Various sensing techniques have been adopted from biological models and used for the characterization of underwater environments (Ju & Ling 2014, Tao & Yu 2012, Dijkstra et al. 2005, Kottapalli et al. 2017). Such sensors may assist or even

replace the sonar and vision functionalities in some applications that require certain levels of accuracy, stealth, or environmental impact. Kottapalli et al. developed a MEMS pressure sensor for AUVs (autonomous-underwater-vehicles) that mimics the fish lateral-line (Kottapalli et al. 2012). Motivated by Dehnhardt’s experiments of Harbor seals, Eberhardt et al. presented a system of artificial whiskers that produced vibration signals that were related to the hydrodynamic trail of a pilot submarine (Eberhardt et al. 2016). We believe that further development of biomimetic sensory systems would help marine robots to expand their perception of the surrounding fluid motion.

Previous studies about seal’s sensing abilities have guided us to explore how the seal interprets the perceived whiskers’ vibrations for hydrodynamic detection. Different vortex structures were shown to carry information about the direction of the disturbance source to the seal (Krüger et al. 2018, Wieskotten et al. 2010*a*). Wieskotten et al. showed that the seal is able to track a propelled and gliding submarine, even with two different wake’s inner fields (Wieskotten et al. 2010*b*). By fluid-whisker interaction, the seal is able to detect the direction in which it needs to swim to track the swimming body (Eberhardt et al. 2016). The wake of a cylinder, which mimics the trail generated by a prey (fish), was reported to induce time-variant deflection responses of artificial seal-like whiskers (Muthuramalingam & Bruecker 2019). With the whiskers distributed over both sides of the frontal area of the pinniped’s head, the generated wake affects each whisker differently, depending on its adjacent local flow structure. We believe that, by comparing the vibrations of different whiskers, information about the location of the wake’s source can be deduced. The whiskers’ vibrations in (Muthuramalingam & Bruecker 2019) were measured by tracking the whisker tips’ motion while using a camera. Other embedded techniques, such as the fiber-Bragg-grating (Yu et al. 2004, Grattan & Meggitt 2013) and strain gauges, can also be used to record the bending responses of such whisker beams.

Neural systems of the brain do a unique job in exploiting the perceived noisy raw data. In the visual cortex, signals that contain visual information (e.g., colours, intensities, etc.) are interpreted as recognizable faces and objects. In the auditory

cortex, the noisy vibration signals (i.e., amplitudes and frequencies) are interpreted as meaningful sounds. Likewise, it is believed that the seal’s brain is capable of translating the perceived whisker vibrations into a hydrodynamic image of the surrounding aquatic environment. Accordingly, we aim to realize an artificial-neural model that relates the vibration signals of an array of artificial whiskers to the source of the disturbance that causes these vibrations. In 2017, the same approach was taken by (Zhuang et al. 2017) for developing a goal-driven neural-network model that mimics the rodent’s vibrissal-trigeminal system. They built a 31-whisker array that performed as a bio-physical realistic model the rodent’s vibrissal system. As the whiskers swept across various objects with different shapes, they collected the data from different sweeps (i.e., torques and forces at the base of each whisker) and used them to train the networks to perform a three-dimensional (3D) shape recognition task.

Whisker-like artificial systems have been utilized in engineering applications for both active and passive sensing. Pearson et al. demonstrated the use of active whisker-arrays for increasing the amount and quality of tactile sensory information for mobile robots inspired by the vibrissal sensory systems of small mammals, such as rats (Pearson et al. 2011). Similar whisker-like tactile systems have been developed and tested for recognizing the shapes and identities of different surrounding objects (Lepora 2016, Kim & Möller 2007, Delamare et al. 2016). The hitherto known studies of the use of whiskers in underwater sensing have focused on finding the sensitivity limits of such structures in sensing flow disturbances in the aquatic environment. A special undulated design of the cross-section along the whisker body was found to suppress the vortex-induced vibrations of the whisker, thus removing the unwanted responses induced by the seal’s own propulsive motion (Hanke et al. 2010, Beem & Triantafyllou 2015). These results inspired Alvarado et al. to propose a whisker-type sensor design that could be tuned in order to amplify certain hydrodynamic signals and suppress others (e.g., noise) (y Alvarado et al. 2012). Recently, experimental studies were carried out in our group for underwater sensing using arrays of whiskers, where it was proven that the deflection signals of artificial whiskers can decode the specific shedding frequency of a Kármán vortex street (Muthuramalingam &

Bruecker 2019). The studies also highlighted the importance of the vortex-induced pressure-gradients as a major contribution to the jerky response of the whiskers. These studies have established the basis for the present work.

## **Objective**

While previous studies have proposed and developed promising underwater sensors based on seal whiskers' behavior, the vast majority could only identify the hydrodynamic wakes generated by different objects and some of their characteristics. Up to now, to the best of the authors' knowledge, whisker-like sensors were not used for the position detection of a wake's source or for navigation applications in autonomous and non-autonomous underwater vehicles. In this study, we aim to employ the ability of seal whiskers to detect surrounding water movements in the development of an underwater sensor that detects the position of the source of an upstream flow disturbance. Using supervised learning, we develop two models that relate the whiskers' vibrations, on both sides of a pinniped's head model, to the 2D coordinates of the position of an upstream wake-generating body. The proposed sensory system implements a stealthy and life-like way of hydrodynamic sensing. It is meant to build the basis for the development of a replacement or complementary device to the current conventional underwater tracking systems.

## **3.2 Materials and methods**

### **3.2.1 Physical model**

A copy of a sea lion's head was designed and 3D printed at City, University of London based on the CT scan data of a real sea lion that was acquired from Museo Delle Scienze, Italy. Optical fibers were gathered and illuminated from one end and inserted through holes from the back side of a pinniped's head model. The fibers' free endings, which are existing out of the holes from the front side of the head model, perform as artificial whisker-like transducers. The diameter, lengths, and locations of the fibers were selected so that their dimensions and spatial distribution are

comparable to those of real whiskers based on the analysis presented in (Summarell et al. 2015, Sawyer et al. 2016). The fibers are made of polymethylmethacrylate (PMMA), which has a Young’s Modulus of about 3.5 GPa (Leal-Junior et al. 2018), which is similar to the real whisker’s (Subramaniam et al. 2017). An illumination source was attached to the end of the fibers that act as a guide to the light until it exists from their tips. Figure 3.1 shows the 3D printed head and the attached fibre cables that act as artificial whiskers. All of the fibers have the same diameter of 0.75 mm that is constant over their lengths. We capture the motion of 12 artificial whiskers that have the same length and were previously shown in (Muthuramalingam & Bruecker 2019) to have a similar response to real whiskers.

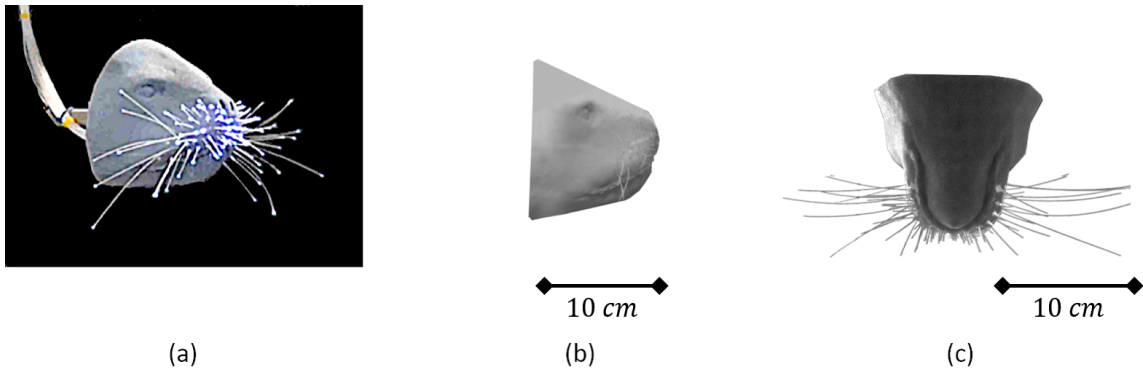


**Figure 3.1:** Three-dimensional (3D) printed model of the pinniped head. (a) captured image of the head while the optical fibres are illuminated. (b) side view (c) plan view of the head.

### 3.2.2 Experiment

Figure 3.2 shows the experimental setup used for generating the data, which will then be processed to prepare the training datasets (input-target pairs) of the learning models. The head model is placed and fixed in the center of an open-surface water tunnel with a transparent test section (120 cm  $\times$  50 cm  $\times$  40 cm: length  $\times$  width  $\times$  depth), which processes a water flow of 30 cm/s free-stream velocity. A 35 mm cylindrical metal rod is vertically placed in the open-surface flow in the upstream direction of the head. A high-speed camera records the coordinates of 12 whiskers’ tips that are distributed on both sides of the head and subjected to the hydrodynamic trail of the cylindrical rod which can be located at different locations in the water tunnel.

The wake generated by the cylinder can be characterized by the Reynolds and Strouhal numbers;  $Re$  and  $St$ , that are given by Equations (3.1) and (3.2):

$$St = \frac{fD}{U_\infty} \quad (3.1)$$

$$Re = \frac{U_\infty D}{\nu} \quad (3.2)$$

where  $f$  is the Strouhal frequency,  $D$  is the diameter of the rod,  $U_\infty$  is the free-stream flow velocity, and  $\nu$  is the kinematic viscosity of water. For cylindrical bluff bodies and the present configuration;  $Re \simeq 10^4$  and  $St \simeq 0.2$  (Williamson 1996), a repeating pattern of vortices (Kármán vortex street), is formed in the wake of the cylinder, which interacts with the artificial whiskers, which act like cantilever beams, in the form of bending deflections.

### 3.2.3 Data acquisition

The high-speed camera (ProcImage 500-Eagle high-speed camera, 1280 px  $\times$  1024 px, Photon Lines Ltd, Bloxham, UK) is used to record the bottom view of the head and the illuminated whisker tips at a frame rate of 200 fps and with a pixel resolution of 0.294 mm/px, given in Table 3.1. Figure 3.3 shows the image captured by the camera in two different modes: (1) eight-bit grey level mode. (2) binary mode with centroid detection of white connected pixels in a selected area in the frame. The 12 coordinates of the centroids of the white dots that correspond to the whiskers' tips are extracted from the second-mode frames and then saved for further processing. The position trajectories of the tips of the outer whiskers that possess the largest length ( $l \simeq 10$  cm) are recorded throughout various tests. The inner whiskers are less sensitive to the disturbance generated by the upstream rod that is placed at different locations relative to the head due to their lengths and orientations. For each of 32 different positions of the cylinder in the two-dimensional (2D) domain, a separate recording of the image-coordinates of the whisker tips (that has a period of approximately one minute) is saved for further processing. For the present set-up, the recording has to be stopped each time before the position of the cylinder is

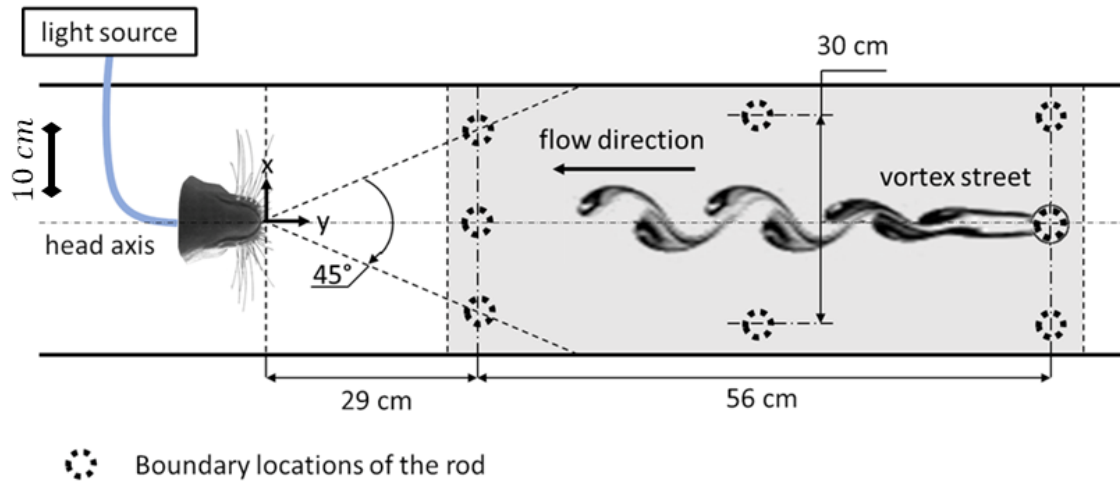
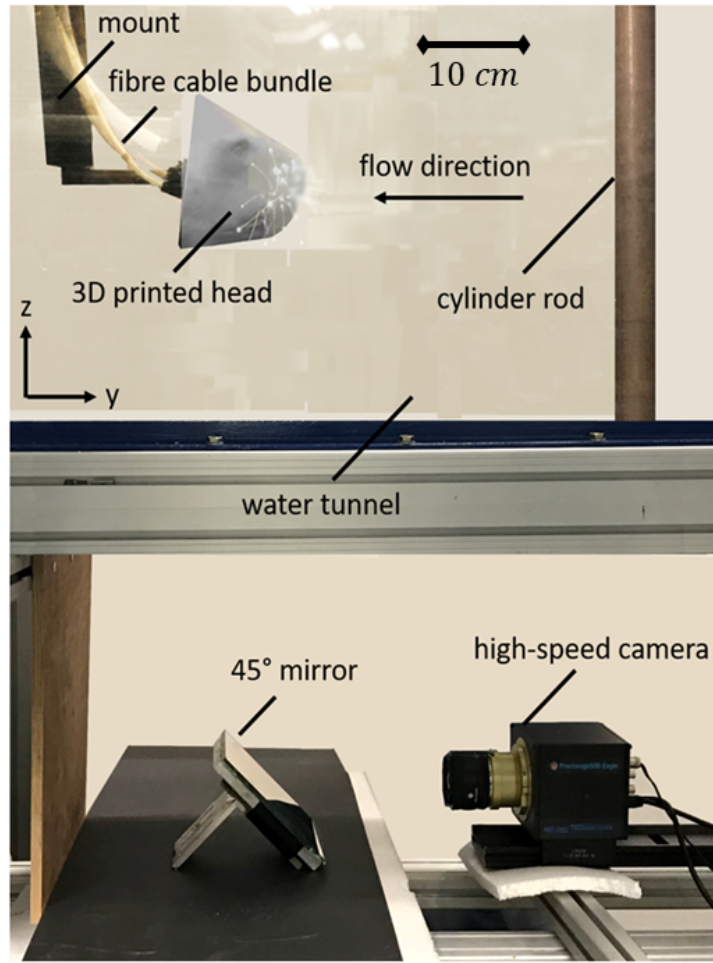


**Figure 3.2:** Experimental set-up of the artificial head and the flow disturbance inside the water tunnel. The side view (top) shows the optical setup of a high-speed camera underneath the test section and a 45° mirror that are used to monitor the motion of the illuminated whisker tips. The plan view (bottom) shows the boundary locations of the cylinder during different tests. The recorded data of the whiskers' vibrations due to the existence of the cylinder at different locations are used for training the learning models. The origin of the coordinate system is placed at the intersection of the head axis with its frontal face.

**Table 3.1:** Camera settings for the recording of the artificial seal whiskers.

setting	frame rate [fps]	resolution [ $px \times px$ ]	pixel pitch [ $mm/px$ ]
value	200	1280×1024	0.294

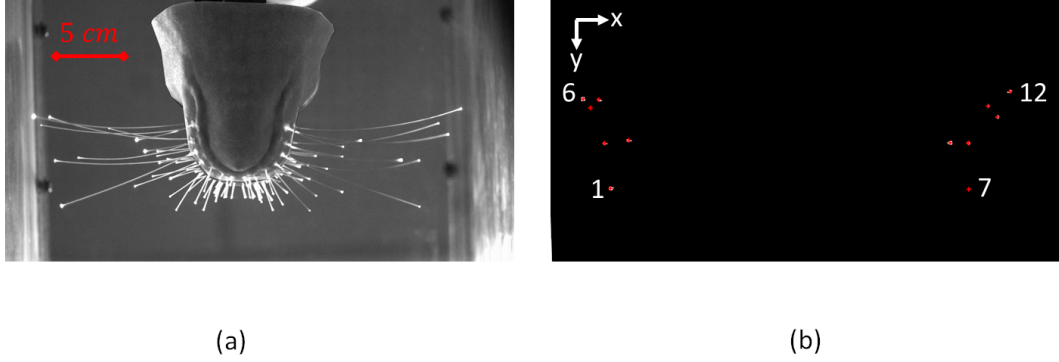


**Figure 3.3:** Camera views in the  $(x, y)$  plane of the two recording modes: (a) grey-level compressed mode. (b) binary mode with centroid calculation. The grey-level image is masked before binarization so that only the 12 whiskers' tips of interest are visible. The whiskers are numbered from 1 to 12 such that whiskers no. 1, 6, 7 and 12 indicate the front-left, rear-left, front-right and rear-right whiskers respectively.

changed.

### Measurement accuracy

The depth of field of the camera measurements is adjusted to about 10 *cm* in order to capture an acceptably-sharp image the 12 whisker tips that have different locations along the  $z$  direction. The resulted image in the grey-level compressed mode is shown in Fig. 2.6.a. During the online recording of the tips, there exists a small uncertainty in the detection of the tip coordinates that results from the centroid calculation algorithm embedded in the camera barycentres recording mode. We could quantify this error while monitoring a stationary tip coordinates in reference conditions and found that the resulted measurement of the centroid has a maximum deviation from the true value of less than the pixel pitch ( $|e_\gamma| < 0.3 \text{ mm}$ ). We also kept the other possible sources of error (e.g. instrumental, environmental or human) as minimum as possible by keeping a dark environment with no light obstruction, minimizing human interference with the optical setup and using a fast USB3 connection (i.e., with high bandwidth) for the transmission of the recorded coordinates.

### 3.2.4 Data processing and feature extraction

Using the recorded tip coordinates in the successive camera frames, the wake-induced deflection vectors,  $\underline{\gamma}$ , are calculated and saved at a sample rate  $r = 200 \text{ samples/sec}$ . As illustrated later in the results section 3.3.1, the recordings of the wake-induced vibrations of the whiskers show that the  $y$  component of the vibrations,  $\underline{\gamma}_y$ , is the dominant component in reaction to the cylinder wake. Here, the two-dimensional coordinates in the  $(x, y)$  plane are recorded, which give us access to the  $x$  and  $y$  components of whiskers' vibrations. The reason we use this optical setup is that it enables use to monitor the whiskers on both directions of the head which is essential to predict the cylinder position. That said, the  $z$  component was also recorded in another optical setup where the camera is fixed in front of the flow channel parallel to the  $(y, z)$  plane, the camera scene is shown in Fig. 3.4. The recorded deflection responses using that setup, presented in section 3.3.1, also show that the whiskers' vibrations in the  $y$  direction in response to cylinder wake is dominant over those in the  $z$  direction. The physical interpretation why the  $y$  deflection component is the main component that captures the whiskers' response to the cylinder wake is illustrated in section 3.3.1. In the following analysis, we use the  $y$  component of deflection to extract the required features for the machine-learning models.

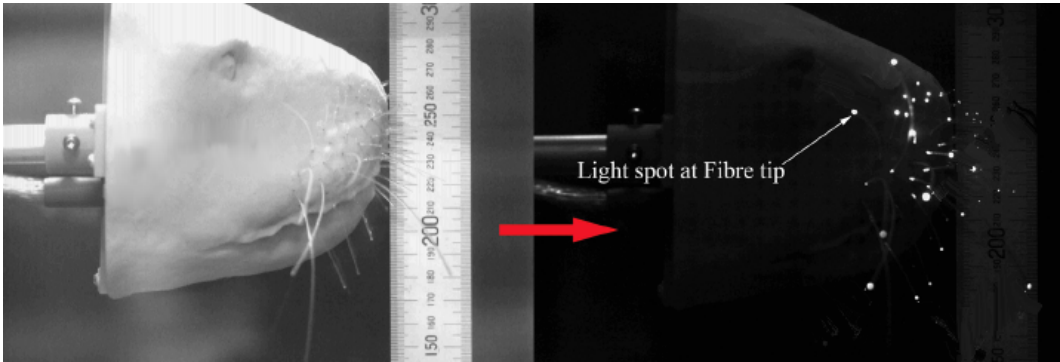


**Figure 3.4:** Camera views in the  $(y, z)$  plane of the whiskers on the right side of the head; from (Muthuramalingam & Bruecker 2019). This set-up was used in another study that used the same whisker-array sensor. Here, we only borrow the recorded  $z$ -deflection response, presented in section 3.3.1, to quantify the deflection response in the  $z$  direction in reaction to the cylinder wake and compare it to the  $y$  component of deflection that we use in this study.

The  $y$ -deflection recordings of the whiskers result in 32 time-series instances of  $\underline{\gamma}_y$  that correspond to the 32 different locations of the cylinder (refer to section 3.3.1,

for example, responses of  $\underline{\gamma}_y$ ). Each time-series is then divided into equal portions of time period  $T$  that are then used to generate the input dataset. The corresponding coordinates of the cylinder in the  $(x, y)$  space are also saved in order to generate the target dataset.

When considering the whiskers' bending responses that correspond to different cylinder positions (presented in section 3.3.1), each time-series portion of the deflection vectors of time period  $T$  is reduced into two 12-element vectors that can capture the reaction of the wake-induced deflection responses to changes in the cylinder's position. The two vectors are: the deflection mean;  $\underline{\bar{\gamma}}$ , and the root-mean-square of the deflection fluctuations around the mean;  $\underline{\gamma}'$ .

$$\underline{\bar{\gamma}} = \frac{\sum_{i=1}^N \underline{\gamma}_y(i)}{N}, \quad N = r \times T \quad (3.3)$$

$$\underline{\gamma}' = \sqrt{\frac{\sum_{i=1}^N (\underline{\gamma}_y(i) - \underline{\bar{\gamma}})^2}{N}} \quad (3.4)$$

$$\underline{\bar{\gamma}} = [\bar{\gamma}_1 \ \bar{\gamma}_2 \ \dots \ \bar{\gamma}_{12}]^T, \quad \underline{\gamma}' = [\gamma'_1 \ \gamma'_2 \ \dots \ \gamma'_{12}]^T \quad (3.5)$$

The generated data along with the corresponding cylinder positions compose two 24-input-single-output datasets. The input dataset is composed of  $Q$  samples of the two vectors:  $\underline{\bar{\gamma}}$  and  $\underline{\gamma}'$  (each consists of 12 elements that correspond to 12 different whiskers), where the number of samples  $Q$  is dependent on the choice of the sampling period  $T$ . The target dataset consists of the separated  $(x, y)$  coordinates of the cylinder positions that correspond to each input sample. Figure 3.5a shows the population of all the input data in the  $\mathbb{R}^2$  space  $(\gamma', \bar{\gamma})$  during the recordings of 32 positions of the cylinder for  $T = 3$  s and  $Q = 772$  samples. The input samples of the whiskers numbered 1 and 12 are highlighted in blue and red colours. The underline in the notations  $\underline{\bar{\gamma}}$  and  $\underline{\gamma}'$  indicates the vector representation of the deflection values for the 12 whiskers (representing 12-element vectors). However, when mentioning the deflection quantities of a single whisker ( $\bar{\gamma}_1$  and  $\gamma'_1$ ) or mentioning the deflection features in general ( $\bar{\gamma}$  and  $\gamma'$ ), the underline notation is not

used. Figure 3.5b presents the sample distribution of all whiskers within two different complete recordings that correspond to positions  $(-15,75)$  and  $(5,75)$  of the cylinder. Different colors in both plots in Figure 3.5b represent different whiskers. The plots show the diversity of each whisker's data of the mean and fluctuating tip deflection during a single recording (the same position of the cylinder). The diversity of the deflection data is more significant for the whiskers that are located on the same side as the cylinder is.

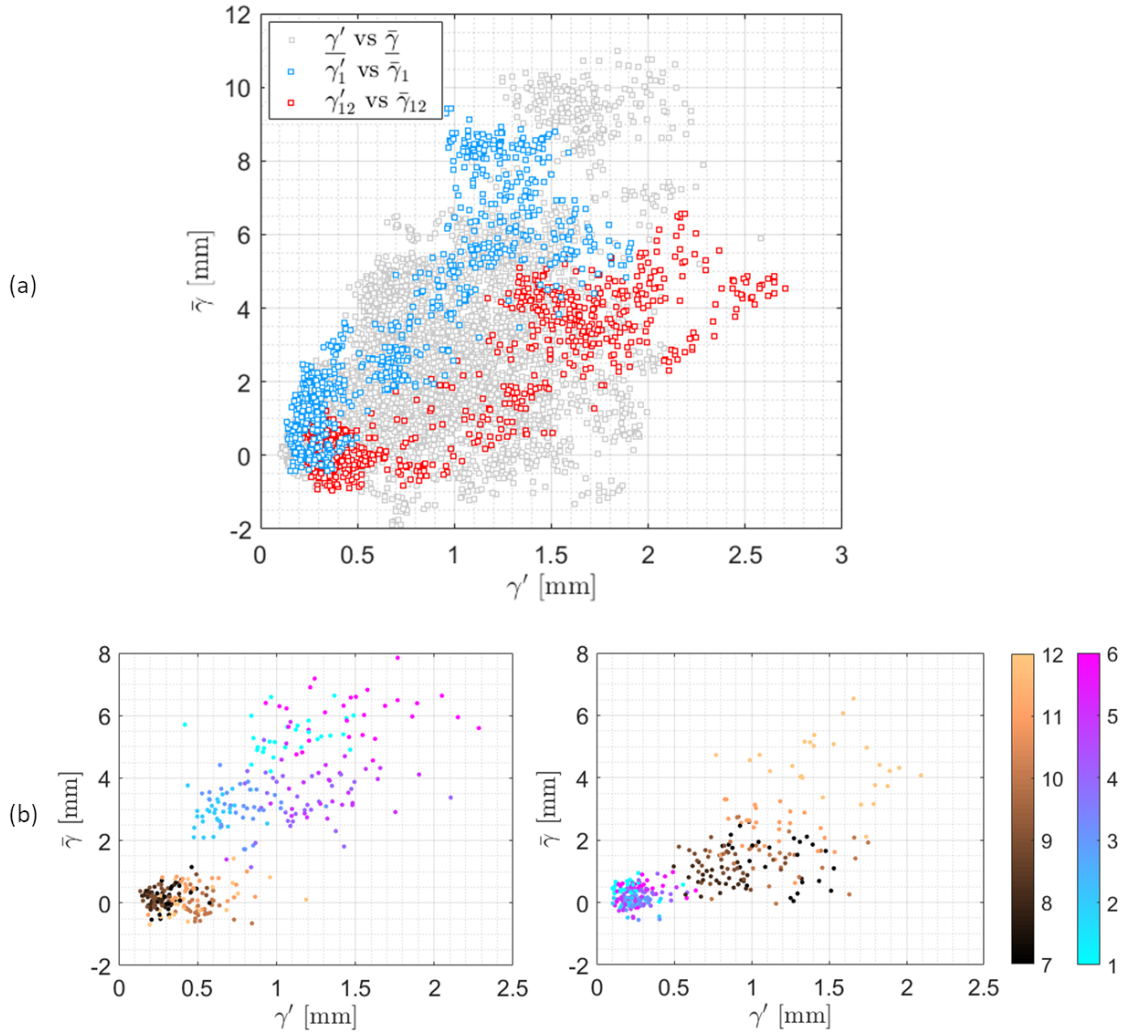


**Figure 3.5:** Distribution of the mean and fluctuating deflection samples (inputs to the learning models) for the 12 whiskers in the  $(\gamma', \bar{\gamma})$  space: (a) population of the complete input dataset that correspond to all positions of the cylinder. Highlighted in blue and red are the data samples of the whiskers numbered 1 and 12 respectively. (b) input samples of two selected recordings that correspond to the cylinder positions  $(-15,75)$  and  $(5,75)$ . The scattered sample points are coloured by their whisker indexes as represented by the colour bar.

### 3.2.5 Supervised learning models

The wake-induced deflection responses vary differently in response to changes in the  $x$  and  $y$  coordinates of the wake-generating cylinder position, as illustrated in section 3.3.1. Consequently, two separate neural-network models are developed in Matlab, so that each one is responsible for the prediction of a single coordinate of the cylinder position. The input samples are separately prepared to be fed into two 24-input-single-output NNs. Each NN is trained to predict the associated coordinate of the cylinder position  $(x, y)$  that corresponds to a given 24-element sample  $q$  of the input deflection data  $\bar{\gamma}$  and  $\gamma'$  of the 12 whiskers. The selected structures of both NNs as well as their learning algorithms are thoroughly described in Appendixes A and B, respectively. The selection of the final structures and the optimization of the NN parameters is based on maximizing the prediction accuracies of the models while keeping them as fast and simple as possible. Finally, the feedforward neural network (FFNN) model is used for the prediction of the  $x$  coordinate, while the time-delay neural network (TDNN) model is used for the prediction of the  $y$  coordinate with an input-memory (input-layer delay) of four samples.

The selection of the NN types, associated with the predictions of each coordinate, was performed as follows: (i) Firstly, different NN types (e.g. feedforward, time-delay, layer-recurrent, etc.) were tested for the prediction of each coordinate separately. (ii) For each type, the models were trained and the best performances were recorded. (iii) At the end, the selection of the final NN type for the prediction of each coordinate was done separately so that the associated NN model achieved the best performance with the simplest structure possible. For example, for the prediction of the  $x$  coordinate, the FFNN type showed a very good performance using a small network structure while the addition of the dynamic behaviour through testing the TDNN type required more computational resources without having a positive effect on the resulted performance.

The task of the learning models is to compare the deflections of the whiskers located at different locations on the head and on both sides and accordingly deduce the position of the upstream wake-generating cylinder, without the need to further

investigate the flow between the cylinder and the head. With a total number of samples of  $Q$ , the network is trained to optimize the model that associates between the different input-target pairs of the given dataset. The number of samples  $Q$  is determined by the selection of the sampling period  $T$ . After setting different values of  $T$  for different rounds of training for both models, we selected the sampling periods 3 s and 5 s, for the  $x$ -coordinate model and the  $y$ -coordinate model respectively.

Two strategies are followed in order to prevent the models from being over-fitted to match the training dataset pairs. The problem of overfitting is a common one when dealing with supervised machine learning and it is thoroughly described in (Dietterich 1995, Jones 1957).

Firstly, the standard 10-fold cross-validation algorithm (Hastie et al. 2009) (developed in Matlab and the code is available with the authors) is performed, as follows: (1) shuffling the training input-target pairs and dividing them into 10 subsets; (2) performing 10 different rounds of the network training iterative algorithm; (3) for each round of training, one of the 10 data folds is used as a validation set while the rest are used for training the network; and, (4) the model accuracy of each round is separately evaluated by calculating the correlation coefficient  $R$  between the trained model response (output) to the validation set and their given targets. The mean of the correlation coefficients  $\Sigma R/10$  of the cross-validation rounds is considered to be an approximate representation of the generalized performance of the model.

For additional validation, three extra recordings of the whiskers' deflection data (with cylinder locations different from those of the original 32 recordings) are processed to come up with approximately  $Q/13$  samples of input-target pairs that would be used as a test dataset. This dataset serves the following purposes: (1) it is used to evaluate the error ranges of the trained-NNs predictions of new cylinder positions in the 2D space  $(x, y)$  that were completely excluded from the training itself; (2) the accuracy of the test results is used as a feedback to minimize the number of training iterations of the networks; and, (3) it is lastly merged with the validation subsets of the 10-fold cross-validation to calculate unbiased estimates of the models' accuracies.

The following parameters are also selected in order to optimize the NN training: the number of NN layers  $M$  and the number of neurons per each of the  $M-1$  hidden layers  $S_{1,2..M-1}$ . The following steps summarize the training procedure and the selection of those parameters:

1. the optimization parameters of the Marquardt–Levenberg Algorithm (MLA) are initialized, as follows:  $\mu = 0.001$ ,  $\beta = 10$  (refer to Appendix B for a brief description of the MLA);
2. preliminary values of the two parameters are used, such that the hidden-layer size is set to  $[S_1 = 15, M = 2]$  for both models;
3. the network training algorithm is performed (as illustrated above) and the overall model accuracy is estimated after the 10-fold cross-validation;
4. the hidden-layer size is then updated by increasing the number of neurons per layer and/or the number of hidden layers and then jumping back to step 3 to restart the training of the networks;
5. after several loops of the above sequence, the hidden-layer size associated with the highest prediction accuracy is selected:  $[S_1 = 15, S_2 = 16, M = 3]$  for the x-coordinate prediction model and  $[S_1 = 29, S_2 = 13, S_3 = 18, M = 4]$  for the y-coordinate prediction model.

## 3.3 Results

### 3.3.1 Wake-induced bending of the whiskers

The wake-induced deflection vectors,  $\underline{\gamma}_x$  and  $\underline{\gamma}_y$ , of the 12 whisker tips in the x and y directions, respectively, are extracted by the processing of the camera output and are defined as:

$$\underline{\gamma}_x = [\gamma_{1x} \ \gamma_{2x} \ \dots \ \gamma_{12x}]^T, \quad \underline{\gamma}_y = [\gamma_{1y} \ \gamma_{2y} \ \dots \ \gamma_{12y}]^T \quad (3.6)$$

$$\gamma_{nx} = x_n - x_{0n}, \quad \gamma_{ny} = y_n - y_{0n}, \quad n \in [1..12] \quad (3.7)$$

where  $x_n, y_n$  are the position coordinates of the  $n$ th whisker tip in the  $(x, y)$  space and  $x_{0n}, y_{0n}$  are the coordinates of the mean position of the  $n$ th whisker tip due to the free flow  $U_\infty$  (without the existence of the cylinder rod).

As a consequence of the orientation of the 12 whiskers along the lateral axis of the head (the  $x$  axis) and due to the small angles of the whiskers' bending, the displacement of the tip in the  $(x, y)$  can be roughly approximated by its  $y$  component, see Fig 3.6. Therefore, the  $x$  component of the wake-induced deflection can be neglected. By examining the different components of the wake-induced deflection of a selected whisker in the presence of the cylinder (plotted in Figure 3.7), it is clear that the effect of the cylinder wake on the whisker's deflection is dominant in the  $y$  direction. For reference, we also plot the results of the  $z$  component of the deflection at the whisker tip,  $\gamma_z = z - z_0$ , where  $z$  is the position component of the whisker tip along the  $z$  axis and  $z_0$  is the nominal position of the whisker tip due to the free flow. The deflection data in the  $z$  direction were taken from a former experiment with an optical setup that captures the whiskers' vibrations in the  $(y, z)$ , illustrated by Fig 3.4, but using the same cylinder disturbance and the same flow speed in the water tunnel (Muthuramalingam & Bruecker 2019). Since the flow and the cylinder's wake are mainly propagating in the  $y$  direction, the  $z$  component of the whiskers' deflection also appeared to be minor when compared to the  $y$  component.

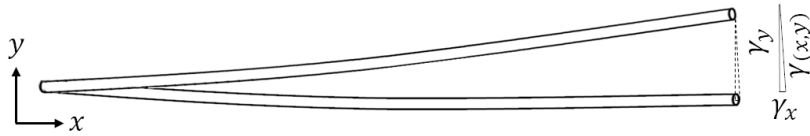


**Figure 3.6:** Schematic drawing highlighting the  $x$  and  $y$  components of the whisker's bending deflection in the  $(x, y)$  plane (the recorded plane in the used camera setup).

Now, let us investigate the effect of changing the position of the upstream cylinder on the  $y$ -deflection curves of the whiskers. In Figure 3.8a, responses of the deflection in the  $y$ -direction are plotted over 1 min. for different locations of the cylinder along the  $x$ -axis and for a reference case of the free flow with no disturbance. In the reference case, with no cylinder placed upstream, the tip location varies slightly from its nominal position due to the self-induced vibration of the artificial whisker in the

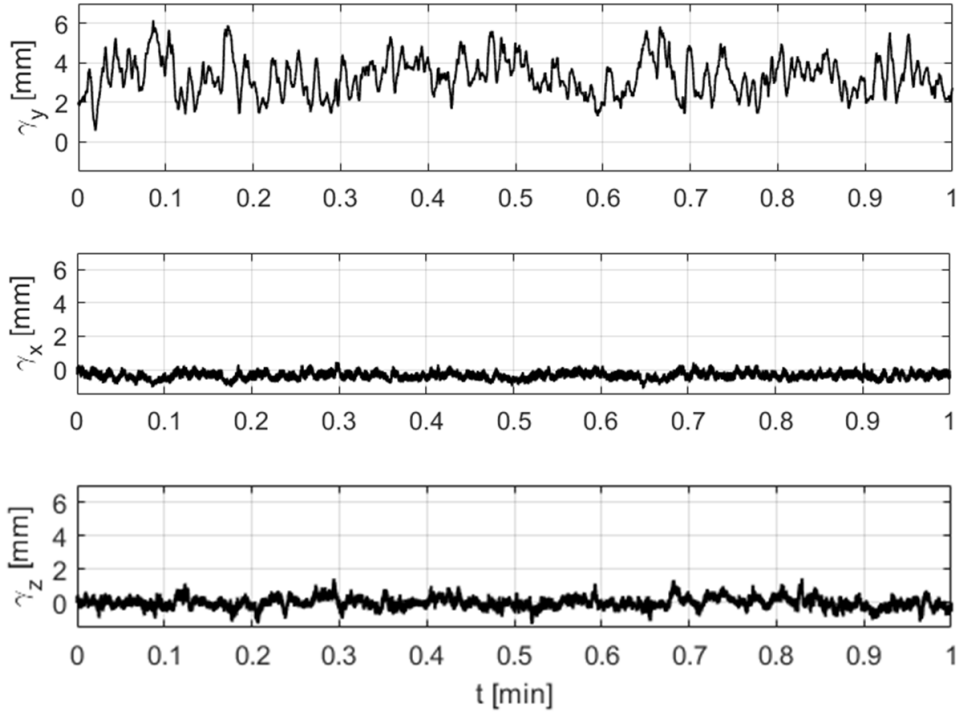


**Figure 3.7:** Wake-induced deflection values of a sample whisker in the z (bottom), x (middle) and y (top) directions.

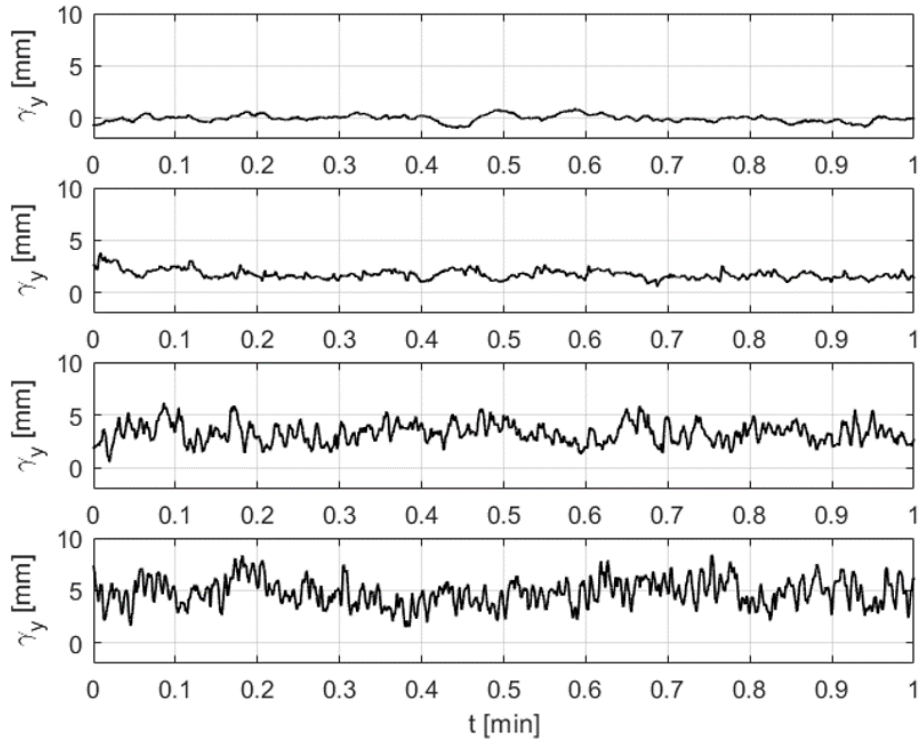
presence of the flow and the surface wave of the open channel (Muthuramalingam & Bruecker 2019). After inserting the cylinder, the vortex street in its wake interacts with the whisker and causes a noticeable large-scale variation of both the mean tip deflection and the amplitude of the deflection’s fluctuations around the mean. The deflection response of a whisker that is located on the left side of the head is found to change with the position of the upstream cylinder. Among three different locations of the cylinder, the largest variation of the deflection curve from its reference case (top plot) is found when the cylinder is on the left and centre position with respect to the head axis (i.e., positions (5,75) and (0,75), respectively). This variation gradually shrinks as the cylinder is moved to the right position (−5,75). Similarly, the response of the deflection is found to vary for different locations of the cylinder along the  $y$ -axis. The fluctuations of the tip deflection curve around the mean (particularly the high-frequency components) get larger as the cylinder moves closer towards the head (from position (5,85) to position (5,29)), as illustrated in Figure 3.8b for the same selected whisker. Despite that the deflection response is not solely dependent on a

single coordinate of the position of the cylinder for a given Re and St numbers, we believe that each coordinate can be separately deduced by comparing the deflection data of different whiskers that are located on both sides of the head.

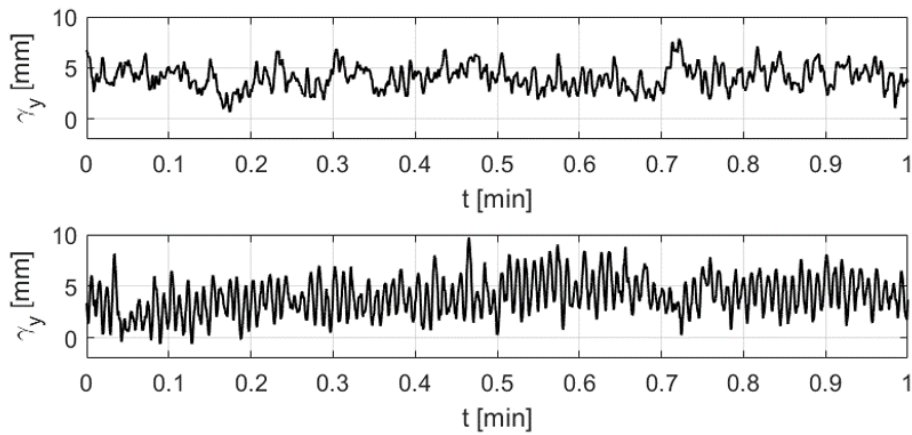
### 3.3.2 Prediction outcomes of the learning models

After the post-processing and reduction of the wake-induced  $y$ -deflection data of the 12 whisker tips that correspond to 32 different locations of the upstream cylinder, 24 inputs (two inputs per whisker) are sampled and used to train the learning models (i.e., each sample is derived from a time-series portion of  $\gamma_y$  of a period  $T$ , as illustrated in the Methods section). Two separate artificial neural networks (NN) are developed to associate between the 24-input samples and each one of the cylinder's position-coordinates in the  $(x, y)$  space. A feedforward neural network (FFNN) is used for the prediction of the  $x$  coordinate, while a time-delay neural network (TDNN) is used for the prediction of the  $y$  coordinate. The Methods Section illustrates the selection and parameter optimization of both networks.

The prediction outcomes of the trained NN models of the  $x$  and  $y$  coordinates of the cylinder positions are plotted in Figure 3.9 in the form of regression and error-histogram plots. In Figure 3.9a,b, the predicted (output) coordinates, represented by the label  $o$ , are plotted as a linear fitted function of their labeled target values, represented by the label  $g$ . The slopes of the fitting lines, as well as the correlations between the output/target pairs, show the ability of both models to accurately predict the upstream cylinder position. The error histograms, as plotted in Figure 3.9c,d, show satisfactory ranges of the prediction deviations from the true target values when considering the small size of the training datasets and the measurement inaccuracies (deviations are represented in the plots by the label  $e$ ). Note that the number of prediction instances is different between the two models due to the choice of different sampling periods  $T$  for both models while preparing their training datasets. Increasing the size of the training samples has been attempted by overlapping the time-series portions of data that are processed to generate training inputs, described in Equations (3.3) and (3.4). However, the overlapping did not have much influence on the resulted error ranges. It is expected that increasing the



(a)



(b)

**Figure 3.8:** Deflection responses of a selected whisker tip due to the existence of the cylinder at different locations: (a) variation of the tip's deflection response due to different  $x$ -coordinate locations of the cylinder. The curves from top to bottom represent the following cases respectively: no cylinder (reference case), cylinder positions:  $(-5,75)$ ,  $(0,75)$ ,  $(5,75)$ . (b) variation of the tip's deflection response due to different  $y$ -coordinate locations of the cylinder. The curves from top to bottom represent the following positions of the cylinder, respectively:  $(5,85)$ ,  $(5,29)$ .

size of training dataset shall be done by performing more recordings of further positions of the cylinder as well as increasing the recording period to have more portions of  $T$ -sampled data. The accuracy of the model as a function of the training-dataset size is investigated later in this section.

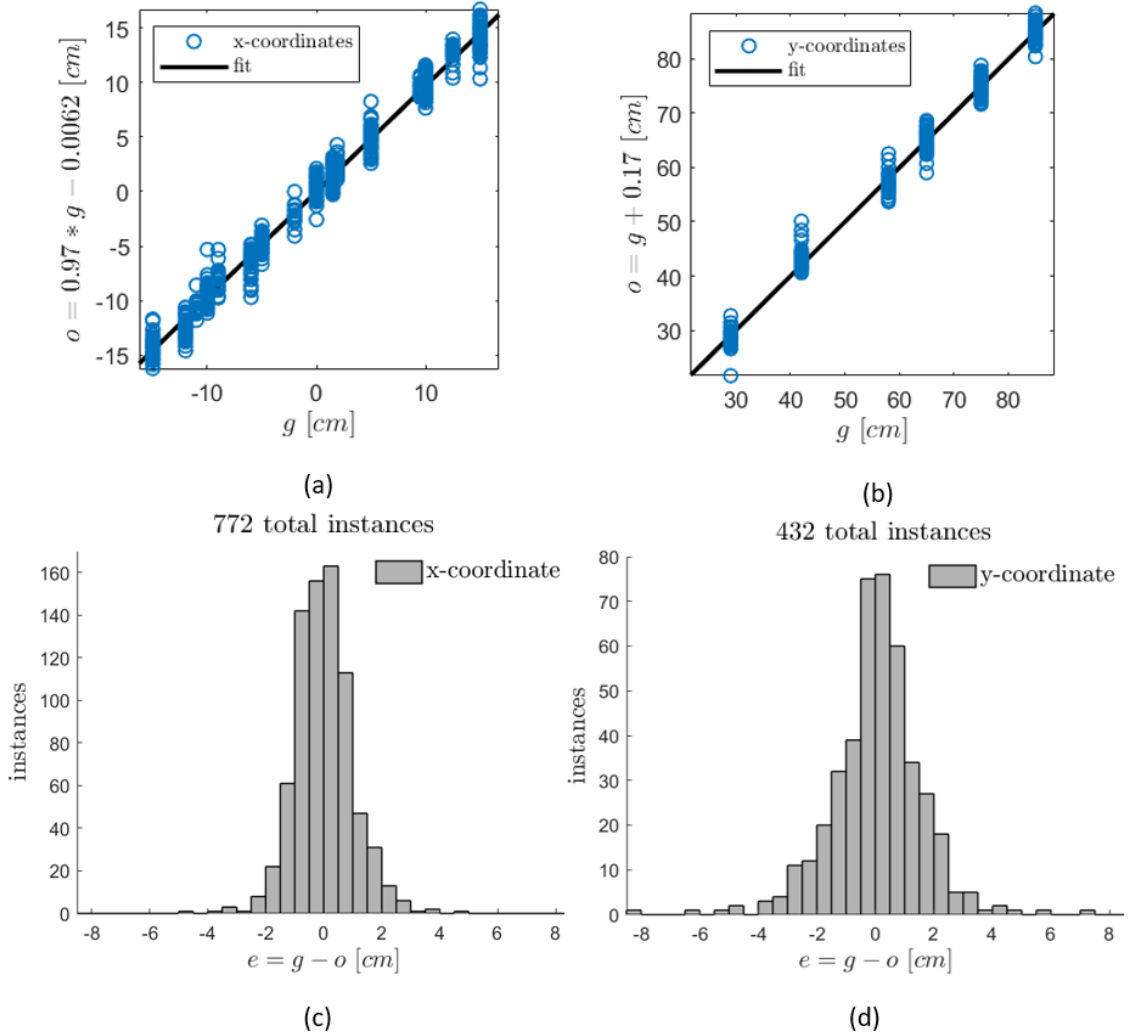


**Figure 3.9:** Results of the NNs predictions of  $(x, y)$  coordinates of different cylinder locations using the input samples of the training dataset. (a,b) predicted outputs of  $(x, y)$  as a linear fitted function of their labeled targets. (c,d) histogram plots of the prediction error instances resulted from both models.

For further validation of the networks' training, the resulted models are tested to predict three positions of the upstream cylinder that have not been included in the training stage. The test datasets of both models are acquired from the processing and reduction of the three extra recordings. Figure 3.10 presents the synchronized

models' prediction results of the test samples. With an average absolute error of about 1 cm and 3 cm for the  $x$  and  $y$  models, respectively, around 85% of the resulted predictions lie in a 2 cm $\times$ 6 cm area around the true value of the cylinder position. However, one can notice that some predictions of the  $y$ -coordinate have larger deviation amounts from the true value (up to a maximum of 12 cm). This might be due to the relatively small size of the  $y$ -model training dataset. It can also be due to the fact that the recordings are not continuous and that the unrealistic discrete changes in the cylinder position are hard to predict for the TDNN model that possesses a dynamic behaviour. Overall, the test results show good agreement with the training validation outcomes in terms of the mean prediction accuracy and the ranges of output error.

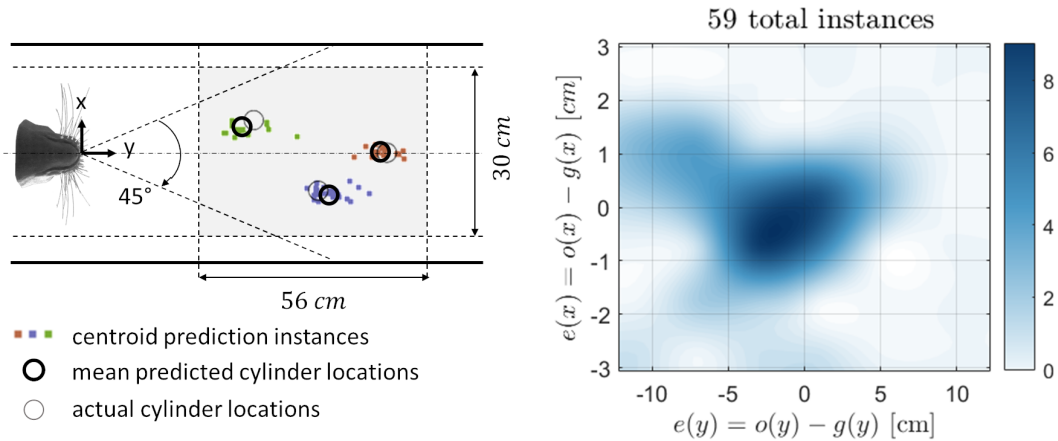


**Figure 3.10:** Results of the NNs predictions of  $(x, y)$  coordinates of three different cylinder locations using the input samples of the test dataset. For a total of 59 input samples and three different locations of the cylinder, the prediction instances of each location and their mean are represented by different colours (left). The two-dimensional (2D) error histogram (algorithm available here (*Efficient 2D histogram, no toolboxes needed, MATLAB Central File Exchange. Retrieved from: n.d.*))) is presented as a colour-contour plot with a total number of 25 bins and a biharmonic interpolant fitting function (right).

By considering the accuracy of the test results, an unbiased estimate of the general accuracy of the NN models can be obtained by merging the test dataset samples with the validation subsets of the 10-fold cross-validation and calculating the correlation coefficient  $R$  between the model response to the merged input data and their given targets. For output-target paired data that consist of  $n$  pairs, the

coefficient  $R$  is calculated as

$$R = \frac{\sum_{b=1}^n (o_b - \bar{o})(g_b - \bar{g})}{\sqrt{\sum_{b=1}^n (o_b - \bar{o})^2} \sqrt{\sum_{b=1}^n (g_b - \bar{g})^2}} \quad (3.8)$$

in which  $o$  represents the output,  $g$  represents the target,  $\bar{o}$  and  $\bar{g}$  are their mean over the given number of pairs, respectively.

Note that the models are still trained with the same training datasets that do not include input samples that correspond to the three test positions of the cylinder. In this case, the mean correlation value at the end of the cross-validation algorithm is found to be 98.68% and 96.15% for the  $x$ -coordinate model and the  $y$ -coordinate model, respectively.

The presented results demonstrate that, in the current set-up, the models' prediction accuracy of the cylinder location does not depend on the distance between the cylinder and the whisker-array sensor, see Fig. 3.9.b. Herein, the cylinder location could be changed within the range  $29 \text{ cm} < y < 85 \text{ cm}$  in which  $y$  is the distance between the cylinder and the lateral axis of the head, see the experimental set-up in Fig. 3.2. The upper limit of the sensor's distance to the cylinder is restricted by the size of the water-tunnel test section. We expect that for very far distances of the cylinder, the wake signature in the flow would become more difficult to be identified. However, similar wake signatures were reported to be clearly detectable in water for distances as far as tens of meters (Dehnhardt et al. 2001). Regarding the very near distances of the cylinder, other sensing techniques (e.g., vision, proximity) can be used for the direct sensing of the cylinder position, similar to how the real seal use its visual ability for spotting near objects.

### 3.3.3 Sensitivity of the predictions to the size of the training dataset

The dependency of the models' prediction accuracy on the size of their training dataset is studied. For each model, the training is restarted with a different number of input/target pairs fed into the NNs. For each size of the training dataset, the accuracy estimate of the models' prediction is calculated. Finally, the scores are

recorded in Table 3.2. The accuracies of both models tend to decrease as the sizes of their training datasets get smaller. However, one can notice that the  $y$ -coordinate model’s accuracy is more sensitive to the training dataset size. Because the TDNN model is used for the  $y$ -coordinate prediction, it is considering  $d+1$  samples of inputs at a given training iteration, where  $d$  is the model’s memory size (i.e., number of input-layer delayed samples). On the other hand, the  $x$ -coordinate model is only considering a single sample of the input vector at a given iteration. Therefore, it is expected that the  $y$ -coordinate prediction can be improved further by increasing the input dataset size. Another reason might be that, although the whiskers’ responses are recorded for 32 different cylinder positions, the  $y$  coordinates of these positions vary on only six discrete levels. Although the current performance of the NN models is satisfying, whiskers’ deflection data that correspond to more  $y$ -levels of the cylinder locations can be used to reduce the  $y$  prediction error ranges.

**Table 3.2:** Sensitivity of the prediction accuracy (mean[ $R$ ]) of the  $(x, y)$  models to the size of the training dataset.

size of training set of x-model [samples]	mean[ $R$ ] for predictions of $x$	size of training set of y-model [samples]	mean[ $R$ ] for predictions of $y$
772	0.9868	432	0.9615
708	0.9795	400	0.9231
644	0.9845	368	0.9332
580	0.9757	336	0.8681
516	0.9734	304	0.8517
452	0.9659	272	0.8099
388	0.9789	240	0.7223
324	0.9718	208	0.6166
260	0.9429	176	0.7367
196	0.9459	144	0.6472

### 3.3.4 Sensitivity of the predictions to the number of whisker-pairs included in the training

Table 3.3 shows the effect of varying the number of whisker pairs used in the preparation of the training datasets on the accuracy results of both models. The number

**Table 3.3:** Sensitivity of the prediction accuracy (mean[ $R$ ]) of the  $(x, y)$  models to the number of whisker pairs included in the training stage. The number is varied in the front-to-rear direction of the whiskers (top) and vice versa (bottom).

number of whisker pairs in the training set	mean[ $R$ ] for predictions of x	mean[ $R$ ] for predictions of y
6	0.9868	0.9615
5	0.964	0.8843
4	0.9851	0.8686
3	0.9738	0.763
2	0.9512	0.8447
1 (front pair)	0.9536	0.6604
6	0.9868	0.9615
5	0.98	0.9120
4	0.978	0.8766
3	0.9781	0.6595
2	0.9583	0.5928
1 (rear pair)	0.9532	0.3305

of whisker pairs is varied, such that one pair indicates the right and left whiskers that have the same index when the whiskers are ordered according to their position on the  $y$ -axis (whiskers that have approximately the same  $y$  position). At first glance, one can say that the accuracy of the models has a direct relation to the number of whisker pairs involved in the training. The more whiskers included, the more accurate the prediction. It is believed that the flow disturbances, including any noise, do not have the same effect on the deflection responses of different whiskers, because they are located at different locations in the 3D space and due to slight variations in their sensitivities. Therefore, increasing the number of whiskers could be providing the NNs with the ability to filter out the noise in the flow and better decode information about the wake source. It is believed that the  $y$ -coordinate model is more sensitive to the variation of the number of whisker pairs included in the training due to the same reasons that are detailed in the paragraph above (while considering the accuracy sensitivity to the training-dataset size).

Table 3.3 also compares the two cases when the number of whisker pairs is firstly varied in the front-to-rear direction and then the other way around. The accuracy

of the  $y$ -coordinate model is noticeably sensitive to the location of the whisker pair. When trained with the front whisker pair, the accuracy of the  $y$ -coordinate model is almost double its value when trained with the rear pair. This can be explained by the fact that the deflection responses of the rear whiskers are not only due to the wake of the cylinder, but could also be due to the wakes of the frontal whiskers that are located in their upstream direction. It is also shown that the effect of varying the whisker-pair location is almost negligible on the accuracy of the  $x$ -coordinate model. A possible explanation is that the corresponding pair of whiskers from both sides of the head are used. Even being affected by the whisker-induced wakes, the network compares the deflection responses of both sides and can successfully encode the information about the lateral position ( $x$ -coordinate) of the upstream cylinder.

### 3.4 Discussion and conclusions

Previous experiments have demonstrated the ability of the real seal to detect and track its prey while using the information acquired by its facial whiskers about the surrounding water disturbances. In this study, an artificial sensor, inspired by the seal's whiskers, is developed using machine learning and tested for underwater 2D position detection of a wake-generating body. The sensor consists of an array of optical fibers that are illuminated from one end and inserted through holes from the backside of a 3D printed model of a pinniped's head and exited from its frontside. The free endings of the fibers act like artificial whiskers that are distributed on both sides of the head. The head, with the artificial whiskers, is mounted inside an open-surface water tunnel that possesses a flow-speed of 30 cm/s. The whiskers are then subjected to the wake that is generated by a cylinder placed at different upstream locations. A high-speed camera, with a special online optical tracking feature, is used to record the wake-induced vibrations of the whiskers at a frame rate of 200 frames per second. The acquired data are processed and reduced in order to generate the input dataset for the neural networks' training. With their targets (output labels) being the separated  $(x, y)$  coordinates of the different cylinder positions, two neural networks are trained using the Marquardt–Levenberg learning algorithm and the

10-fold cross-validation technique to associate between the input/target pairs.

The measured signal herein is the tip deflection of each optical fiber simultaneously, which is directly proportional to the applied bending moment (Euler–Bernoulli beam theory). Although other alternatives to directly measure the bending of the fibers are known and feasible, this path was initially chosen due to the availability of the optical tracking camera. In our future work, we aim to implement Fiber-Bragg-gratings (FBGs) in the optical fibers to estimate the bending fluctuations from the corresponding shifts in the reflected Bragg-wavelength. This method, well established in fiber-optical strain or bending sensors, would allow us to capture the signal from inside an underwater vehicle while the fibers’ free ends protrude from the body as in the current application. FBGs are known for their high measurement sensitivity. Campanella et al. reported that the detection limit of the fiber’s strain using FBG can reach down to the nano-strain range (Campanella et al. 2018). This is expected to improve the measurement resolution compared to the current deflection measurement at the tip using the high-speed camera<sup>1</sup>. Yu et al. presented a bend sensor using an embedded FBG which possessed a curvature measurement resolution<sup>2</sup> of about  $0.0054\text{ m}^{-1}$  (Yu et al. 2004) which corresponds to a deflection value at the tip of our optical fiber of about  $0.027\text{ mm}$  which is also an order of magnitude lower than the current detection limit of the current setup.

Another alternative is the implementation of strain gauges to measure the bending strain of the artificial whiskers. The whiskers in that case can be made from a different material and have a different shape, other than the fiber-optic cables used in the current implementation. Such embedded methodologies would facilitate the integration of the sensor into realistic underwater vehicles.

The trained models can accurately predict the upstream locations of the cylinder that correspond to the training samples of the deflection data as well as the samples of a stranger test dataset, which corresponds to three new cylinder locations. The developed sensor can passively sense the wake and deduce the position of its source with an average absolute error of about 1 cm for the x-coordinate prediction and

---

<sup>1</sup>The current measurement resolution of  $0.294\text{ mm}$  of the deflection at the fiber’s tip corresponds to a strain value in the micro range ( $\simeq 5\text{ }\mu\epsilon$ ).

<sup>2</sup>The curvature resolution represents  $1/R$  where  $R$  is the bend-radius of curvature

3 cm for the y-coordinate prediction. The reported average error is less than the characteristic parameter,  $D$ , of wake-generating body and for distances larger than 25-times  $D$  between the sensor and the body (limited by the size of the water tunnel). The accuracy of the resulted predictions is found to be sensitive to the training dataset size and the number of cylinder locations associated with the recorded deflection data. The accuracy is also found to vary with the number and location of the whisker pairs that are involved in the training process.

The study is limited by the size of the water-tunnel test section and the number of cylinder locations in the performed measurements. Further data collection with more cylinder positions can be performed in the future to minimize the prediction errors of the models. Additionally, as a consequence of the equipment limitation in the water tunnel, the captured recordings of the whisker vibrations is not continuous (i.e., they correspond to discrete changes of the cylinder position). It is expected that, given a continuous variation of the cylinder position in a real-time recording experiment, the NNs can be trained to perform online trajectory-tracking of the upstream cylinder. It is also of interest to test the tracking capability in a larger environment, as we know from previous studies that the wake of a prey can last visible in water for several minutes (more than 3 min. for a small goldfish of a 10 cm body length (Hanke et al. 2000)). The characteristic wake generated by the cylinder in the current implementation of the experiment is comparable to that generated by several fish and cruising submarines. The flow speed used herein is also comparable to the speeds of existing underwater vehicles. Therefore, the responses of the artificial whiskers in such environments are expected not to vary significantly from the current reported ones.

The NN models need to be trained for several scenarios in an otherwise realistic and time-variant environment in order to use the present sensor in underwater-vehicles for tracking applications. The trained network models can then work in real-time with the data acquisition system (i.e., that captures the vibrations of the whiskers and generates the corresponding input data for the models) to continuously update the location of the detected wake's source. Large-scale water currents are not expected to affect the tracking capability of the neural networks, as their

influence would be seen along all the individual whiskers in a coherent manner. In our experiments, when the whisker is placed in the water flow (independent of the existence of the upstream cylinder rod), vortices are shed from the body of the whisker itself (as the whisker is nothing but a cylinder with a relatively-small diameter). Those vortices produce a time-variant force acting on the whisker that leads to oscillations that we call the vortex-induced vibrations of the whisker (also called self-induced vibrations) (Beem & Triantafyllou 2015). These oscillations, with a relatively-high frequency component (the unique frequency of the vortex shedding behind whisker) and a relatively-low amplitude, are different from the wake-induced vibrations of the whiskers resulted from their interaction with the cylinder rod's wake, refer to section 3.7.2 for more information about the vortex-induced and the wake-induced vibrations of the whiskers. In (Muthuramalingam & Bruecker 2019), a detailed analysis of the vibrations spectrum of the whisker in the flow was presented for the same experimental-setup used here, where it was shown that the two components of vibrations (wake-induced and vortex-induced) are clearly separable and that the vortex-induced vibrations are hardly captured in the  $y$  component of deflection which is recorded in the present setup. Herein, the NN models could show a high degree of accuracy in estimating the cylinder position, which suggests that the effect of that unwanted high-frequency noise on the current measurements, if any, is suppressed. As the NNs receive their inputs from all whiskers, they possibly can filter out any minor noise that is simultaneously-detected in the input measurements of different whiskers, allowing the present sensor to be trained and used in an otherwise noisy environment.

In light of the challenges that face the current techniques of underwater surveillance, the presented sensor demonstrates an alternative methodology of target-tracking that can be utilized in autonomous-underwater-vehicles. The sensor implements a stealthy and passive way of perception that is suitable for use in dark or muddy underwater environments. It possesses a minimum level of environmental impact by featuring a lifelike and safe way of sensing, which facilitates smooth integration with the surrounding marine life.

### 3.5 Appendix A

## Structures of the neural-network models

The structures of both the x-coordinate and y-coordinate networks can be described by the schematic in Figure 3.11. The diagram represents a feedforward network structure with  $M$  layers;  $(M-1)$  hidden layers and one output layer, and an optional input-memory function  $\Pi_d$ .

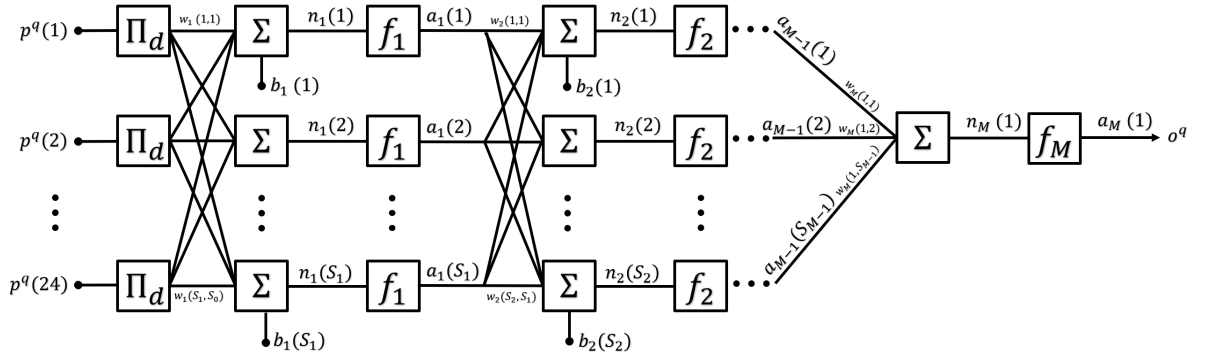


**Figure 3.11:** Structure of the  $M$ -layer feedforward neural networks used for the prediction of the  $x$  and  $y$  coordinates of the cylinder position.

The network input  $\underline{n}$  to the layer  $k + 1$  is a linear function of the output  $\underline{a}$  of its preceding layer  $k$ . In the following analysis until the end of this section, the sample indexes and the layer indexes are represented by superscripts and subscripts respectively.

$$\underline{n}_{k+1} = W_{k+1}\underline{a}_k + \underline{b}_{k+1}, \quad W_{k+1}\underline{a}_k = \sum_{j=1}^{S_k} w_{k+1}(i, j) a_k(j) \quad (3.9)$$

where  $S_k$  is the size of the layer  $k$  (i.e., number of elements of vector  $\underline{a}_k$ ),  $k \in \{0, 1..M - 1\}$  is the layer index,  $\underline{b}_{k+1}$  is the biases vector and  $W_{k+1}$  is the weights matrix of layer  $k + 1$ .

The network output  $\underline{a}$  of the layer  $k + 1$  is

$$\underline{a}_{k+1} = f_{k+1}(\underline{n}_{k+1}), \quad f_{1,2..M-1}(n) = \frac{2}{1 + e^{-2n}} - 1, \quad f_M(n) = n \quad (3.10)$$

$\underline{a}^0$  is connected to the input vector  $\underline{p}$ , that represent the deflection data of the whisker tips, via the input-memory function  $\Pi_d$  of which  $d=0$  for x-coordinate prediction (direct connection) and  $d=4$  for y-coordinate prediction.

$$\Pi_0(p^q) = p^q, \Pi_{\{d|d \in \mathbb{N}\}}(p^q) = [p^q \dots p^{q-d}]^T, \quad (3.11)$$

$$\underline{a}_0 = \Pi_d(\underline{p}) \quad (3.12)$$

$a_M$  is connected to the network output  $o$  and the error  $e$  is defined as the difference between the target label  $g$ , that represents one of the two coordinates of the cylinder position  $(x, y)$ , and the output of the network  $o$ .

$$a_M = o^q, e^q = g^q - o^q \quad (3.13)$$

where  $q$  is the sample index and  $d$  is the memory size of successive input samples. The addition of a  $d$ -sample input-memory provides the model with a dynamic response which could add a noticeable gain to its efficiency. Such networks with a finite-time input-memory are known as time-delay neural networks (TDNN) and have been reported to be particularly efficient in speech-recognition, property-prediction and automatic-control applications (Waibel et al. 1989, Han et al. 1999, Vančura et al. 2008).

## 3.6 Appendix B

### Learning algorithm

The goal of the NN is to map each sample of its input vector to its corresponding given output label (Anderson 1995). The performance of each network model is evaluated by the cost function  $C$  which is defined as the mean squared error (MSE) of all output-target pairs.

$$C = \frac{1}{Q} \sum_{q=1}^Q (e^q)^2 \quad (3.14)$$

in which  $Q$  is the total number of samples.

In order to minimize the cost function, the Marquardt-Levenberg algorithm (Marquardt 1963) (i.e., an optimization of the of the steepest descent method (Rosenbloom 1956) used in the standard backpropagation NN learning (Anderson 1995)) is used to update the weights and biases of the NNs. It updates the network weights and biases in each iteration as follows (Hagan & Menhaj 1994):

$$\Delta \underline{z} = [J^T J + \mu I]^{-1} \underline{\nabla} C, \quad J(i, j) = \frac{\partial e(i)}{\partial z(j)} \quad (3.15)$$

where  $\underline{z}$  is the parameter vector which contains all weights and biases,  $\underline{e}$  is the error vector;  $\underline{e} = [e^1 .. e^Q]^T$  and  $J$  is the Jacobian matrix of the network error. The term  $[J^T J + \mu I]^{-1}$  substitutes the learning rate of the original steepest decent algorithm. The separate term  $J^T J$  is the Gauss-Newton approximation of the Hessian matrix of the cost function;  $H(C)$ . The parameter  $\mu$  is initialized with a small value and is multiplied by a factor  $\beta$  each time the update of  $\underline{z}$  results in an increase in the value of  $C$ . As  $\mu$  gets larger, the algorithm approaches a steepest descent algorithm with a learning rate of  $1/\mu$ .

## 3.7 Critical Analysis

### 3.7.1 Overview and study contributions

The study demonstrates the use of optical fibers to mimics seal’s whiskers to localize underwater wake-generating preys or bodies. It presents a novel type of sensing that allows underwater robotic systems to perceive the underwater disturbances safely and passively. The sensors detects the hydrodynamic vibrations in the object trail and hence identify its two-dimensional location parallel to the water surface.

Using learning models, the study demonstrates how the vibrations of artificial whiskers can be interpreted as useful information such as the position of the disturbance source. By training two neural-network models the sensor could locate the position of an upstream cylinder with high precision. Despite a few recognized limitations of the study, it seam adequate for an exploratory phase of research in underwater surveillance. In general, the main problem addressed in the study – underwater localization using learning models – is appealing and worth being researched given its potential to implement an affordable, passive and safe solution of underwater sensing.

### 3.7.2 Exploratory discussion and future work

The subject of this study is implementing an underwater wake-tracking sensor inspired by pinniped’s whiskers. Other applications of whisker-like system (e.g., tactile sensors inspired by mammals whiskers) were not detailed in this chapter. Instead, previous experiments studying the seal’s tracking capabilities using its whiskers as well as underwater bio-inspired sensors were given particular attention. In section 2.1.3 in the Background chapter, the light is spotted on some previous implementations of whisker-type engineering systems

#### 3.7.2.1 Whisker-Flow interaction

As discussed in section 3.4, each whisker, being nothing but a cylinder placed in a water flow, produces a local wake composed of shed vortices with a frequency much

higher than the cylinder rod’s shedding frequency. That local wake produces what is called the vortex-induced vibrations of the whiskers, which has a low amplitude and a high frequency relative to the wake-induced vibrations of that same whisker due to the presence of the cylinder rod in front of it. Fig. 3.12 demonstrates the difference between the vortex-induced and the wake-induced vibrations of the whiskers (the cylinder in the figure represents the whisker).

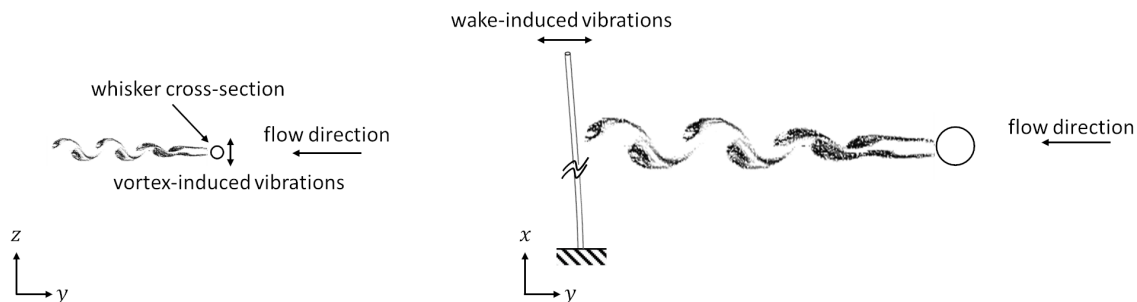


**Figure 3.12:** Schematic showing the difference between the vortex-induced vibrations (left) and the wake-induced vibrations (right) of the whisker.

In Fig. 3.12 (left), the produced vortices behind the whisker induce a time-variant force that acts on the whisker body which leads to the vortex-induced vibrations of the whisker. The frequency of these vibrations is noticeably higher than that of the wake-induced vibrations. The reason is that the frequency of the vortex-street behind the whisker, in Fig. 3.12 (left), is approximately  $D_{rod}/D_{whisker} \simeq 47$  times higher than that behind the cylinder rod in Fig. 3.12 (right). It is important to note that the high-frequency component of the whisker oscillations is the dominant mode of vibration in the free flow (without the existence of the cylinder rod) (Muthuralingam & Bruecker 2019). The vortex-induced vibrations are mainly detected in the measurements of the  $z$  component of whisker deflection which is not captured in the current measurement setup.

### Complexity of computational-fluid-dynamics simulations

The whisker interacts with the surrounding flow in form of in-line and cross-flow vibrations of its body. In order to simulate the whisker dynamics in reaction to the flow, direct numerical simulations can be used. The simulation of the whisker-fluid interaction in complex shear-flow situations would provide a better understanding

to the relation between the whisker’s vibrations and the surrounding flow characteristics, which could be also related to the wake-generating body’s geometry and position. However, to capture the dynamics of a single whisker, multiple servers may be needed to perform the required computations. The time step of the computations, even in a clean-flow case, needs to be small enough to capture the whisker flow-induced vibrations (Violette et al. 2007). Introducing the rod’s wake in the flow adds an additional degree of complexity to the problem. For each computational step, the flow field in between the rod and the whisker needs to be rendered. This will increase the required computational power substantially for simulating the dynamics of a single whisker. In our case, if we consider multiple whiskers, it would be very difficult to resolve such a problem.

The advantage of using machine learning is that there is no need to study the detailed flow-field between the rod and the whisker or around the whisker itself. The only required information to predict the cylinder’s location is the measured vibrations of the whisker tip. The neural-network models, that mimic the whisker-trigeminal system in the brain, can then extract the important features in these vibrations and relate them directly to the upstream wake-generating body.

### **3.7.2.2 Usage of the whisker-array sensor in real-life applications**

The characteristic wake generated by the cylinder in the current set-up, despite being in a controlled environment, is comparable to the wake generated by seal preys (fish) (Beem & Triantafyllou 2015). It is also comparable to the wake usually generated by the fin of submarines (Lee et al. 2016). However, future work (e.g. testing the sensor and training the networks in time-variant and complex environments) is still required to validate the sensor for use in robotic navigation/tracking applications.

In our experimental facility, using the water flow in the water-tunnel enables us to use a fixed cylinder as the wake-generating source. In real-life applications, the prey (e.g., fish) produces the wake by swimming with a relative speed to the background water. The use of a swimming object as the disturbance source requires a wide facility with the wake-generating body and the sensor both moving inside it (such as a swimming pool). However, that is not necessary in the current imple-

mentation as the background water is moving instead of the cylinder and the sensor themselves, simulating the required relative motion situation. That enabled us to conduct a fairly-similar study in our available lab facilities and using the fixed setup. The important feature herein that is required for the NN models to perform their predictions is the recorded vibrations of the whisker-array sensor in response to the wake.

The NN models are currently trained within a constant-speed flow situation. Changing the speed of the flow in the water-tunnel would cause a change in the frequency of the shed vortices from the cylinder rod (i.e., a shift in the Strouhal frequency of the cylinder's vortex street) which would be reflected, in a coherent manner, on the measurements of the whiskers' vibrations. Likewise, in case of changing the speed of the wake-inducing body and the sensor or in case they have different speeds (in a real-life application where the target and the sensor are moving in a relatively-still background), a shift in the frequency spectrum of the recorded wake-induced vibrations of the whiskers is also expected. Since these changes (either in the current setup or in a real-scenario) would affect all whiskers simultaneously, I expect the NN models to still be able to compare the deflection responses of different whiskers, located at different locations on the head and on both sides, and hence deduce accurate cylinder locations. Similarly, in case of existing water currents, their effect would be mainly detected in the deflection measurements of all whiskers simultaneously and is not expected to substantially impact the final prediction accuracy.

Indeed, some difficulties will to rise while testing the sensor's integration into an underwater vehicle in a realistic environment as the network training would then need to be expanded for different new situations. Nevertheless, the present study can establish the basis for the models' training in such future applications.

### **3.7.2.3 Implementation of the deep-learning sensor in real-time applications**

The current data-acquisition technique using the high-speed camera allows for feeding the neural models with the recoded deflection data of the whiskers after the

experiments are concluded. Once the NNs are trained in a given environment, the data acquisition process and the predictions of the trained models can run simultaneously in real-time. However, in order to perform such online data-acquisition, a different measurement technique of the deflection data of the whiskers will be more suitable. In future work, it is intended to use strain gauges or fiber Bragg-Gratings as embedded methodologies to capture the vibrations of the whiskers from inside the implemented sensor and feed them directly into the neural models in real-time (described in the Discussion section 3.4).

Currently, the Neural models require a time-series of the vibration data that has a period of 3–5 seconds to predict a new position of the cylinder. I expect that this period can be minimized by expanding the training dataset used for the neural models' training (i.e., by training the networks for more cylinder locations). The selection criterion of this period for the optimum prediction performance is illustrated in section 3.7.3. That said, a shorter time period can still be selected while keeping the resulted accuracy of predictions sufficiently high, see Fig. 3.14.

#### **3.7.2.4 Optimization of the neural network parameters such as the hidden-layer size**

Since the whisker's vibration response varies differently due to changes in the  $x$  and  $y$  coordinates of the upstream cylinder, the parameters of each neural model associated with the prediction of a separate coordinate are expected to be different from those of the other model. In other words, the hidden layer sizes and the number of neurons of the neural models depend, in a direct manner, on the predicted quantity. Accordingly, the selected parameter values herein are only suitable for the current application (i.e., prediction of the position of a wake-generating body using the wake-induced deflection of the whiskers) and for the specific quantity ( $x$  or  $y$ ) associated with the model.

The selection of the NN parameters was performed based on the achieved performance of the associated NN models. Several parameter values were tested, and the corresponding prediction performances of the models were estimated. Finally, the parameters associated with the models of the most accurate predictions were

selected.

The choice of the NN architecture came down to multiple trials. During the various tests to finally select the hidden-layer sizes, the NN models were initialized with a single hidden layer with 15 neurons. Then, every possible configuration was tested (increasing the number of neurons/hidden layers by one per each trial) until the hidden-layer size reached: 3 hidden layers, 30 neurons each (every time a new hidden layer was added, the number of neurons in that layer was initialized with 10). After reaching that size, the number of neurons per each of the three hidden layers was increased by amounts of 2 until it reached 40. Larger values of increments were chosen in this stage because the networks clearly showed overfitted behaviours resulting in less validation accuracies as the number of neurons got higher. Bigger hidden-layer sizes were tried (until the number of neurons reached 40) only to verify that the overfitted behaviour continues. Finally, the hidden layer size associated with the model that scored the highest prediction accuracy is selected.

The chosen approach and the choice of the increment values agree with the suggestions in the literature:

- to reach a small-size network that successfully performs the required task, you start with a small structure, growing additional neurons until the satisfactory solution is reached (Neural Networks: An Introduction. By Berndt Müller, Joachim Reinhardt, Michael T. Strickland)
- the number of neurons per a hidden layer should usually be between the size of the input layer and the size of the output layer – less than twice the size of the input layer (Introduction to Neural Networks with Java. By Jeff Heaton)

### **3.7.3 Prediction of the direction of the disturbance source and selection of the parameter $T$**

In this section, a third neural-network model is developed to predict the direction of the upstream wake-generating body. The angle that the position vector of the body makes with the anteroposterior axis of the head (the  $y$  axis in Fig. 3.2) is defined as  $\psi = \tan^{-1}(x/y)$ , in which  $x$  and  $y$  are the position coordinates of the upstream

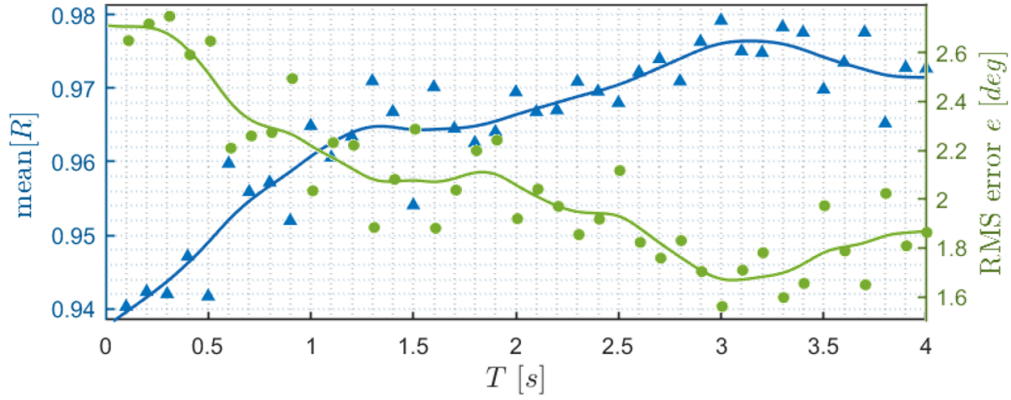
body in the head reference frame. Although the angle  $\psi$  can be derived directly from the network outputs of the two developed models for the  $x$  and  $y$  coordinates, the period of the deflection data time-series required to predict  $y$  is 5 seconds. The aim here is to investigate if a model can be developed for the prediction of the angle separately whose input data can be derived from a smaller time-series ( $T < 5s$ ). I will also demonstrate in this section the detailed procedure followed to select the parameter  $T$  for sampling the input datasets of the neural models.

The feedforward network structure is again used for the prediction of the angle  $\psi$  (the same structure as the one used for the x-coordinate prediction). The input data for training and testing the model are derived from the same recordings of the wake-induced deflection data used for the two previous models and using Eqs. 3.3 and 3.4. In the following analysis, the procedure followed to select the value of the period  $T$  used for generating the input dataset is illustrated.

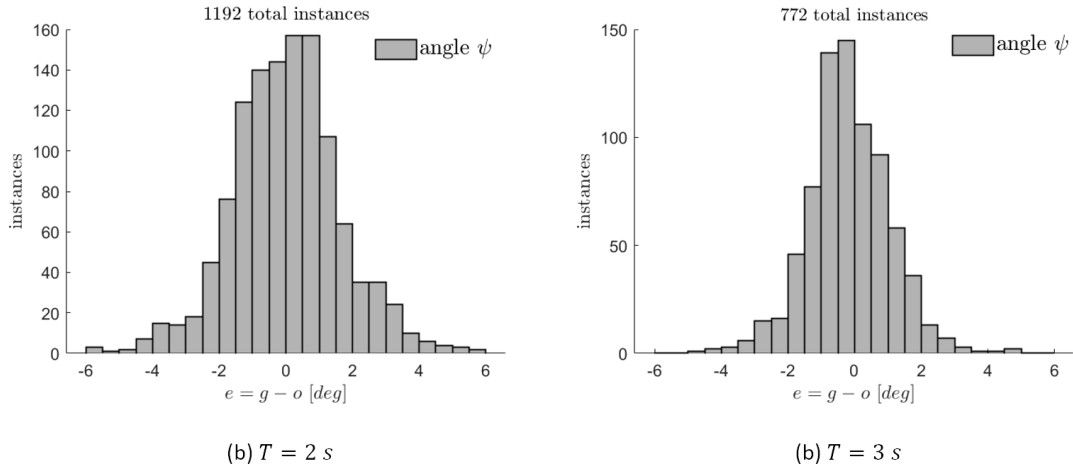
1. Firstly, the lower limit for  $T$  is set to a small enough value. Here, I start with  $T = 0.1 s$
2. The selected value of  $T$  is used to generate the training data of the NN model and hence the network is trained to predict the value of  $\psi$
3. The accuracy and the RMS error level of the trained model is recorded
4. the value of  $T$  is incremented by a discrete amount (in this case 0.1 s) and then the two steps (2 and 3) are repeated
5. the process is stopped when a saturated performance is achieved

Fig 3.13 shows the performance values of the trained models for  $\psi$  prediction (mean[ $R$ ], maximum error – max[ $e$ ] – and root-mean-squared error – RMSE – of the predictions) in response to varying the parameter  $T$ .

As shown in the plot, the best prediction performance of the angle  $\psi$  is achieved when the input training data are derived from 3-second time-series data of the whiskers vibrations. That said, the performance of the direction prediction is also satisfying for lower value of  $T$ . For example at  $T = 2 s$ , the correlation mean is 96%



**Figure 3.13:** Performance results of the trained neural-network models for the prediction of the disturbance source direction (the angle  $\psi$ ) for varying values of  $T$ .



**Figure 3.14:** Error histogram plots of the angle  $\psi$  predictions of the associated neural network models for: (a)  $T = 2$  s and (b)  $T = 3$  s.

and the RMSE is below 2 *deg*. Choosing a lower value of  $T$  would allow for using smaller amount of data in the control of the orientation while running the networks online in the assumed situations. This would in turn give the opportunity to track the direction of targets that are varying their location quickly relative to the head model. The error histogram of the angle  $\psi$  prediction of both the  $T = 2$  s and  $T = 3$  s models is plotted in Fig 3.14.

# Chapter 4

## Spontaneous Synchronization of Beating Cilia: An Experimental Proof Using Vision-Based Control

### Abstract

This article investigates the formation of spontaneous coordination in a row of flexible 2D flaplets (artificial cilia) in a chamber filled with a high viscous liquid ( $Re = 0.12$ ). Each flaplet is driven individually to oscillate by a rotary motor with the root of the flaplet attached to its spindle axle. A computer-vision based control loop tracks the flaplet tips online and toggles the axle rotation direction when the tips reach a pre-defined maximum excursion. This is a vision-controlled implementation of the so-called “geometric clutch” hypothesis. While running the control loop with the flaplets in an inviscid reference situation (air), they remain in their individual phases for a long term. Then, the flaplets are studied in a chamber filled with a highly viscous liquid, and the same control loop is started. The flexible flaplets now undergo bending due to hydrodynamic coupling and gradually form a pattern of metachronal coordination. The study proves in a macroscopic lab experiment that viscous coupling is sufficient to achieve spontaneous synchronization, even for a symmetric cilia shape and beat pattern.

## 4.1 Introduction

A wide range of biological systems use synchronization in their movement patterns (Pikovsky et al. 2003, Strogatz 2012), ranging from small-scale unicellular organisms to larger scale sperms and microswimmers. At low Reynolds numbers, this coordination is crucial for the propulsion of microswimmers or the generation of transport on ciliated walls (Knight-Jones 1954, Elgeti et al. 2015). Motile cilia are found in many different tissues, from the brain (Sawamoto et al. 2006) to the lung and the oviduct, and in many organisms, from *Chlamydomonas* (Rüffer & Nultsch 1997) and *Volvox* (Short et al. 2006, Drescher et al. 2010) algae to *Paramecium*. It is the beat coordination of the individual cilia in the array that plays an essential role in the locomotion of sperm, the cleaning of breathing air, and the movement of oocytes in the fallopian tube (Fulford & Blake 1986*b*, Blake et al. 1983, Smith et al. 2008, Brokaw 1972). Metachronal synchronization results when cilia beat with a certain constant phase shift between each other. Similar coordination was imposed among artificial cilia and flagella for microswimmer propulsion. Many studies have proposed ways to use the cilia propulsion mechanism in nanomechanics and microfluidic devices (Dreyfus, Baudry, Roper, Fermigier, Stone & Bibette 2005, Gauger et al. 2009, Sanchez et al. 2011). Inspired by the progress made in the fabrication of small-scale flexible structures, the hydrodynamic interaction of artificial cilia has become again of interest to optimize such engineered systems. At low Reynolds numbers, the inertial terms in the Navier–Stokes equation can be neglected (section 2.2.5), simplifying the momentum equation to the linear Stokes equation

$$\mu \nabla^2 u - \nabla p = 0, \quad \nabla \cdot u = 0 \quad (4.1)$$

with the pressure  $p$ , the velocity  $u$  and the dynamic viscosity  $\mu$  of the fluid. As the right-hand side in Eq. 4.1 is time-independent, it suggests that for symmetric beating patterns it may not be possible to spontaneously come into a synchronized beating pattern (Kim & Powers 2004, Elfring & Lauga 2009). However, the flexibility of the cilia adds another degree of freedom to the equation (Reichert & Stark 2005,

Bennett & Golestanian 2013). Typically, the beating pattern of natural cilia is non-symmetric in time; i.e., during the power stroke, the cilium moves forward while stretched out straight, and during the return stroke it moves back while retraced (bent) near the wall (see Fig. 2.1a). This was adopted by computer-simulation studies for 2D arrays of cilia (Elgeti & Gompper 2013, Gueron & Levit-Gurevich 2001), together with the “geometric clutch” hypothesis that was first introduced by Lindemann (Lindemann 1994, 2007). The results suggested that hydrodynamic interactions are sufficient to achieve spontaneous synchronization for such models of natural cilia.

Synchronization of model flagella was studied for macroscopic rotating helices (Kim & Powers 2004) and colloidal spheres driven by optical traps (Kotar et al. 2010, Di Leonardo et al. 2012). However, up to now simple 2D symmetric flaplets have not been tested for their possible self-synchronization. Often in such 2D systems, synchronization was just imposed by the control of the actuators to achieve maximum efficiency of the transport (Brücker et al. 2017). Therefore, the process of spontaneous synchronization has not been studied in such experiments under well-defined conditions so far. The aim of the present work is to introduce such an experiment and to test the conditions that lead to spontaneous synchronization. Therefore, we use silicon rubber flaplets as artificial, macroscopic cilia that are driven by motor-controlled rotating axles in which the flaplets are clamped at one end and are forced to undergo a symmetric beating motion at a predefined frequency. The integration of the fluidic system with a feedback control loop is done by vision-controlled implementation of the “geometric clutch” hypothesis. Bending deflections of the flaplets’ tips are tracked while applying geometric thresholds for the toggling of the rotating direction of each individual motor separately. Hereby, we will experimentally prove that viscous coupling can force a row of individually beating flaplets from random initial conditions into a synchronized beating pattern, forming a metachronal wave. The chapter is structured as follows: Section 2 describes the methods, and results are shown in Section 3. Finally, discussion and conclusions are given in Section 4.

## 4.2 Materials and methods

### 4.2.1 Fluidic chamber and artificial cilia

The experimental setup is designed to mimic a row of five artificial cilia ( $n = 5$ ) with individual beating actuations at their roots. Each of the flexible cilia with a length  $l = 40 \text{ mm}$  and width  $w = 20 \text{ mm}$  is made of a silicon rubber sheet of thickness  $t = 2 \text{ mm}$  (material polydimethylsiloxane (PDMS), Young's modulus  $E = 5.96 \text{ MPa}$ ). The Young's modulus was qualified with an impulse-response test as described in Favier et al. (Favier et al. 2017). The obtained value is well within the range documented for standard silicon rubber (Young's modulus  $1 - 50 \text{ MPa}$ ).

Each of the flaplets (indicated with index  $i$  from 1 to 5) is clamped with one short end to the spindle axle of a rotary DC servo motor. The individual DC motors with the flaplets are fixed on a support frame in a horizontal row such that the flaplets' free ends point vertically down with an interspacing between each of the spindles of  $b = 22 \text{ mm}$ . The row is inserted from top in the center of a closed chamber with a squared ( $60 \text{ mm} \times 60 \text{ mm}$ ) cross section, see Fig. 4.1. The chamber is made out of transparent Perspex to allow optical access to the system. Both lateral sides of the chamber can be closed and liquid can be filled such that the flaplets are fully submerged up to the top wall of the chamber. As working liquid, pure glycerol is used with a density of  $\rho = 1260 \text{ kg} \cdot \text{m}^{-3}$  and a viscosity of  $\mu = 0.95 \text{ Pa} \cdot \text{s}$  at room temperature.

For the present study, the flaplet beating cycle is initiated with a beating frequency

$$f_{beat} = \frac{1}{T_c} = 0.3 \text{ beat } s^{-1} \quad (4.2)$$

The beat amplitude  $A = 9 \text{ mm}$ , which is set to ensure that each two neighbouring flaplets do not just touch each other at an angle of  $|\theta| \leq 0.22 \text{ rad}$ . The tip speed  $v$  is given by the rotary velocity of the DC motor  $\omega = 0.267 \text{ rad/s}$ . Small adjustments of the individual amplitudes  $A_i$  are necessary to take into account small uncertainties in the DC motors controller response between programmed angular speed and the actual measured ones. Therefore, a calibration procedure is done for the individual

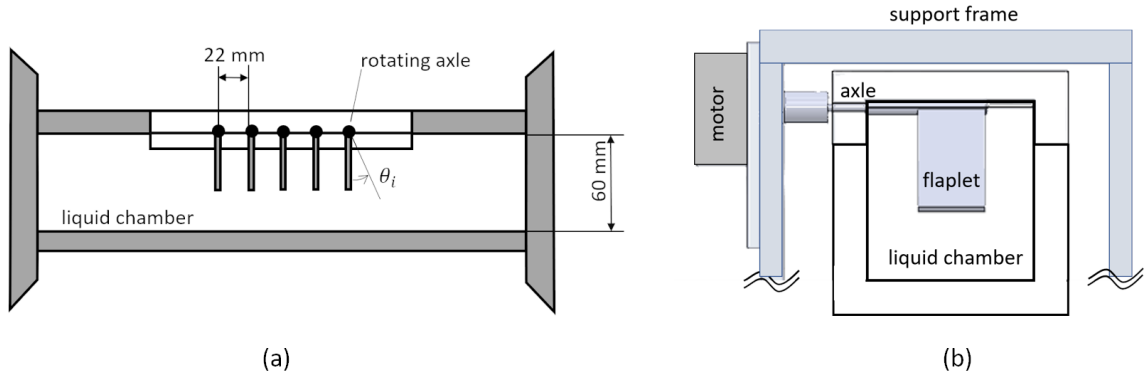


**Figure 4.1:** Schematic view of the closed working chamber: (a) front view of the chamber with the five flexible flaplets at resting conditions and (b) side view of one flaplet clamped on the short side to the axle of one of the five motors.

amplitudes  $A_i$  to end up with the same frequency  $f_{beat}$  for each individual flaplet  $i$ . The characteristic parameter of the flow is the Reynolds number, which is defined with the preset amplitude  $A$  and the tip speed  $v$

$$Re = \frac{\rho v A}{\mu} \simeq 0.12 \quad (4.3)$$

For reference measurements with the control loop in an inviscid environment, the chamber is emptied to ensure that no viscous coupling affects the flaplets' motion.

## 4.2.2 Computer-vision system

The control loop presented herein requires the online tracking of the tips of the flaplets and the feedback of the position to the main control processor and the motors (see Section 4.2.3). Therefore, a high-speed camera (ProcImage 500-Eagle high-speed camera,  $1280 \times 1024 \text{ px}^2$ , Photon Lines Ltd, Bloxham, UK) is monitoring the tips of the five flaplets recognized by a fluorescent marker glued onto each tip. Two mirrors are used to facilitate the illumination and imaging of the system, as shown in Fig. 4.2. An LED light source (IL-106G Green LED Illuminator, HARD-Soft, Krakow, Poland) is adjusted to continuous illumination mode. The fluorescent material glued onto each tip scatters the emitted light back to the camera. An optical filter (optical edge filter, cut-off wavelength 550 nm, Novasoft, Aarhus, Den-

mark) is used to reduce stray light from the back of the frame, which is painted in black. The markers are arranged in a zigzag pattern to help identify the tips separately as single objects in the image processing phase, even when the flaplets are getting close to each other. The scene is recorded with a rate of 505 fps at  $700 \times 225 \text{ px}^2$  image format, and a typical image of the 5 visible marker dots is shown in Fig. 4.3. Each image is processed online to extract the tips coordinates using image binarization and centroid detection. The resulting coordinates of the tip markers are then fed to the main controller at a sampling frequency of  $f_s = 15 \text{ Hz}$ . The current implementation allows a maximum observation period of approximately 1 min, corresponding to a total number of 18–20 cycles.

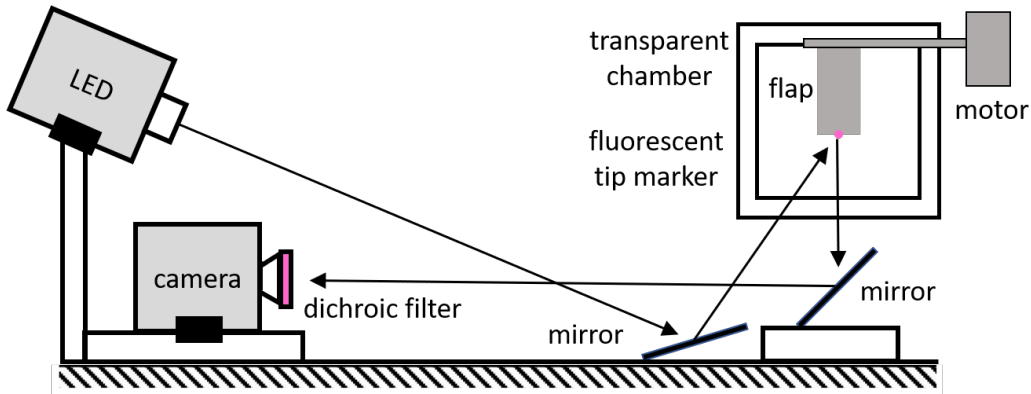


**Figure 4.2:** Schematic view of the optical set-up to record the tip motion of the artificial cilia.

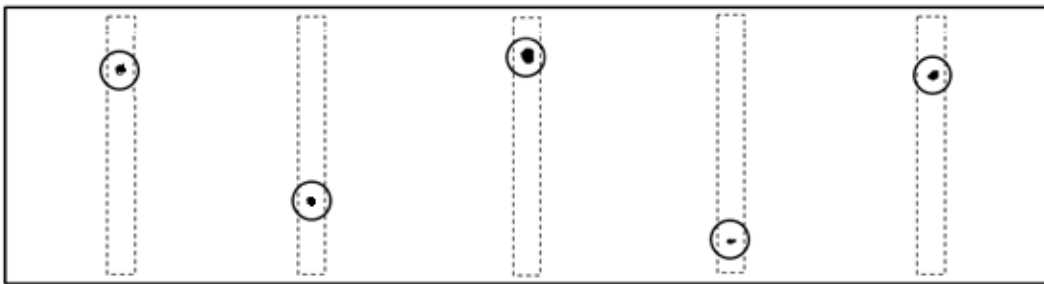


**Figure 4.3:** Original image of the flaplet tips after binarization and color inversion for a single instant in the process of self-organization. For reference, we overlaid circles marking the centroids and the flaplet tip contours (dashed lines). The oscillatory motion is along the horizontal image axis, perpendicular to the flaplet span. The left-most flaplet is  $i = 1$ , and the right most is  $i = 5$  in rising order. Note that the roots of the model cilia are uniformly spaced, as shown in Fig. 4.1.

### 4.2.3 Feedback control-loop

A mechatronic system is designed to actuate, monitor, and control the row of flaplets. The system shown in Fig. 4.4 is composed of three subsystems: (i) the main plant, which consists of the chamber, the flaplets, and the five motors; (ii) the supervisor controller for monitoring the flaplets and controlling the servo motors with the desired speed and direction; and (iii) the optical recording system, which consists of the high-speed camera and the illumination. The energy flows into and out of the control system as follows: The five flaplets are controlled to start beating from random initial positions at  $t = 0$ . The motors' speeds and beating amplitudes are set by the controllers to the same calibrated values. Then, the motion is started and continuously monitored by tracking the tip markers. Each motor is advised to reverse direction once the attached flaplet's tip reaches its predefined maximum position.

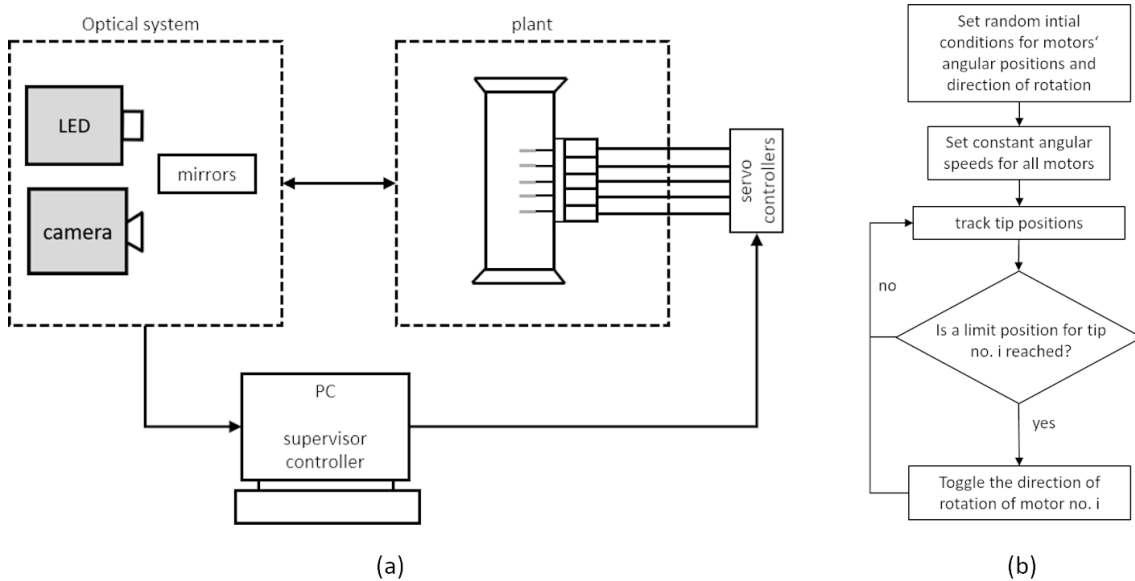


**Figure 4.4:** Schematic view of the integrated mechatronic system (a) and the feedback control-loop flow chart (b).

This implementation in the control loop is equivalent to the geometric clutch hypothesis introduced by Lindemann (Lindemann 1994, 2007), which suggests that the cilium motor reverses the beating direction once a certain terminal position is reached. Herein, the bending deformation is induced by the viscous coupling of the surrounding liquid and neighbouring flaplets and causes the tip of the flaplet

to deviate from the simple zig-zag trajectory prescribed by the rotating axle. This allows for phase variations in the system due to force-induced bending deformation of the flexible cilia.

#### 4.2.4 Reference test in an inviscid environment

This step is required to guarantee that the measured time-variant phase differences among neighbouring beating flaplets in the presence of the liquid can be regarded as a reaction to the hydrodynamic forces of the surrounding fluid and the viscous coupling among the flaplets and are not imposed by timing issues raised by uncertainties in the image processing and motor control. Therefore, the control loop is first run in an inviscid environment with the liquid chamber fully emptied. Theoretically, in the reference case the phase relationship between the flaplets in the row should remain exactly the same for infinite number of beats after the start of the control loop. All uncertainties such as those in the imaging processing to detect the tips centroids and in the calibrated motor speeds can accumulate to an observable variability of the phase, which can then be used to quantify an upper limit within the observation period. The performance in air is then compared to the control loop run with the flaplets in the liquid. The coordinates of the tips are by-passed to a recorder during the motion tracking while the control loop is running.

### 4.3 Results

Figure 5 shows the recorded position trajectories for both situations: the control loop in reference situation and the control loop in the existence of strong viscous coupling. Indeed, the results for the reference situation demonstrate that the phase relationship between the flaplets in the row remains approximately constant over the number of recorded cycles. A small variation of flaplet  $i = 3$  is witnessed after 15 cycles, which is less than a 10% phase drift. All flaplets perform a zig-zag-type oscillatory motion while they remain in straight shape. In contrast, for the system with high viscous coupling, the phase differences are time-variant. The flexible flaplets start bending as a reaction to the stronger fluid forces, which leads to a

deviation of tip location relative to the position prescribed by the angle of the motor with the flaplet in straight shape. Maximum values of about 2 *mm* were observed, which corresponded to roughly 25% of the beat amplitude. The system comes after about 15 cycles into a coordinated synchronous motion when the phase lag among the tips remains approximately constant in space (between pairs) and in time. The straight black lines in Fig. 4.5 (bottom) show this observation clearly. The lines are passing through the instants where the individual beats reach their peak position. Only flaplet  $i = 1$  appears to be lagging behind the other tips. There are some possible explanations for this observation, which are discussed in the next section.

For further characterization of the metachronal coordination between neighbouring beating flaplets  $i$  and  $i - 1$ , we define the cycle ratio  $CR$  from the phase differences of reversal times  $T_{peak}$  in the corresponding beat cycles:

$$CR_{ni}(T_{peak}) = \frac{T_{peak\ i} - T_{peak\ i-1}}{T_c}$$

Fig. 4.6 shows the temporal evolution of the phase differences between each couple of neighbouring flaplet tips for flaplet  $i = 2-5$ . The non-dimensional phase differences  $CR_{ni}$  of the four synchronized flaplets are found to converge to 15–25% of the cycle period between each neighbouring couple. This is close to the phase lag observed in natural cilia models to obtain optimum transport conditions (Gauger et al. 2009). For comparison, the black line shows the behavior of one pair of flaplets  $CR_{n4}$  for the reference case in air.

## 4.4 Discussion and conclusions

Previous numerical models of the cilia beating patterns have simulated the spontaneous emergence of metachronal waves due to hydrodynamic interactions (Niedermayer et al. 2008, Elgeti & Gompper 2013). Implemented in these models is often the geometrical clutch hypothesis, which was introduced by Lindemann (Lindemann 1994, 2007) to explain how the cilium motor reverses the direction. Up to now, there has been no experimental proof of this spontaneous synchronization for rows of arti-

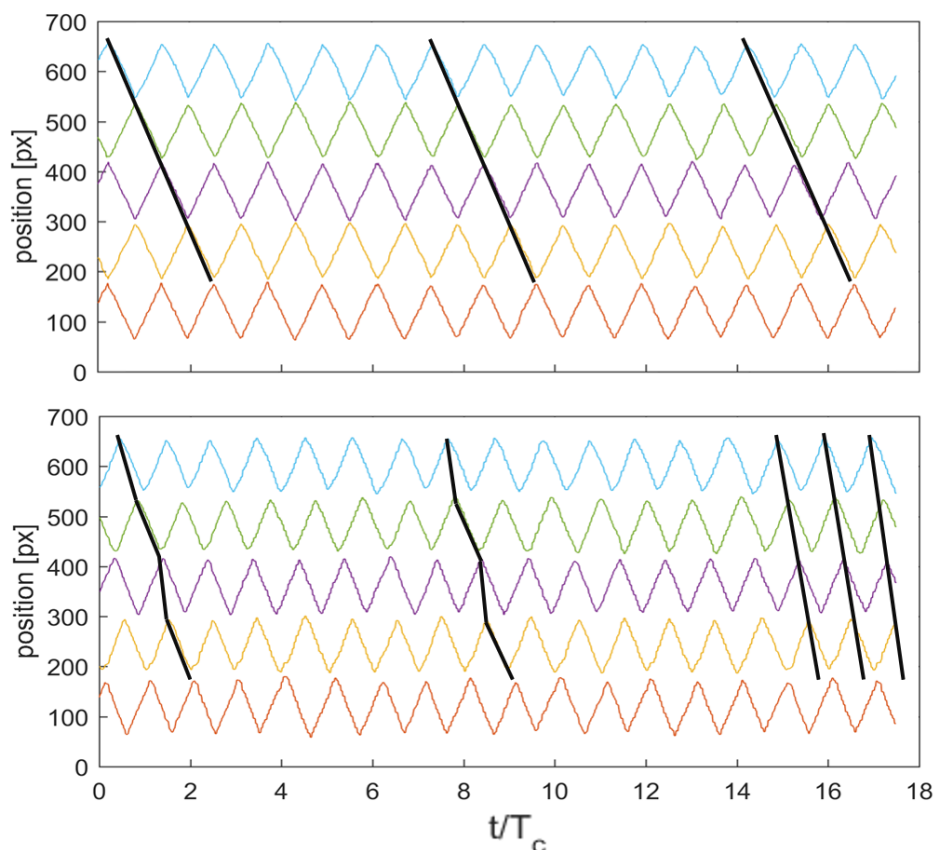


**Figure 4.5:** Position trajectories of the five flaplet tips while applying the feedback control loop; (top): flaplets in reference case (air); (bottom): flaplets in highly viscous liquid. The black lines indicate the phase relationships between maxima of neighbouring flaplets over time. The position corresponds to the centroid coordinate of the flaplet tip marker in pixel units along the horizontal image axis in Fig. 4.3. The colors indicate the different flaplets (red: flaplet  $i = 1$ , blue: flaplet  $i = 5$ ). Note that we selected for visibility reasons in the plot for air the initial phase shift between pairs of cilia to be at the extreme value of  $180^\circ$ , which results in out-of-phase beating. Therefore, the black lines in the upper plot do not indicate any synchronization, as there is no interaction between the flaplets.

ficial 2D cilia under controlled conditions. In our study, we have verified the previous hypotheses in a macroscopic experiment by documenting the spontaneous synchronization in a row of flaplets due to their hydrodynamic interaction. This has been made possible by (i) introducing system flexibility through the use of silicon rubber flaplets as artificial cilia, which undergo bending in the highly viscous environment at  $Re = 0.12$  and (ii) introducing online computer vision as the feedback methodology within the control loop that mimics the geometric clutch hypothesis. Since the silicon flaplets bend as a reaction to the hydrodynamic coupling, it was important to optically track the flaplet tips for control of the beat reversal commands. This

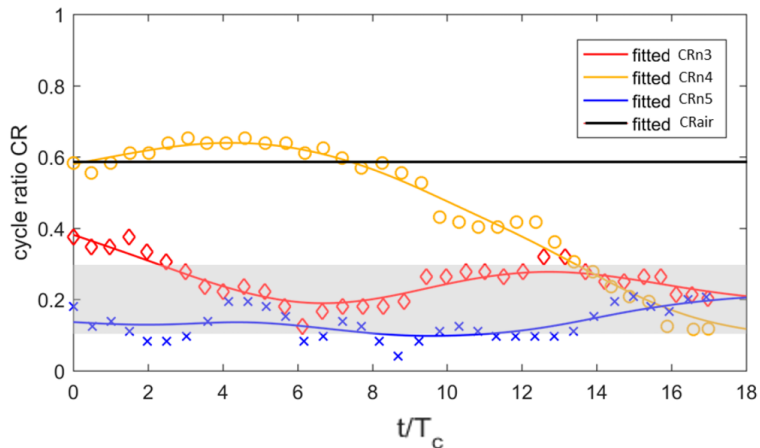


**Figure 4.6:** Evolution of the flaplet-to-flaplet phase relationship in the first 18 cycles, shown in terms of the cycle ratio CRn3–5 between pairs of flaplets 2–5. For comparison, the black line shows the behavior of one pair of flaplets CRn4 for the reference case in air. The curve fitting is done with a smoothing spline. The gray shaded region is the range of cycle ratios reported in literature for metachronal waves of model cilia to achieve optimum fluid transport (Gauger et al. 2009).

additional degree of freedom in the cilium tip motion relative to the imposed motor trajectory allows coordination to take place. This load response has been measured and discussed for natural cilia and flagella in (Klindt et al. 2016). Our system is therefore equivalent to the key property of natural cilia required for synchronization, as they are able to change speed (or tip speed) in response to hydrodynamic load. Hydrodynamic coupling is herein the source driving the system to synchronization, as nothing has changed between the two control experiments except the fluid. This agrees with the conclusions given in (Gueron et al. 1997).

The results show that a system of 5 individually beating flaplets can form spontaneous synchronization after several cycles, while the same system in an inviscid environment remains fixed in its initial phase relationships. The observed convergence to phase differences of 15–25% of cycle duration agrees with the range found in natural cilia coordination for optimum flow transport (Gauger et al. 2009). This hints at a possible relaxation of the control system to a minimum of dissipation in the liquid mixing. Additional flow measurements in our experiment are planned to gain details of the flow field during synchronization (see chapter 5).

Changing the stiffness of the flaplets is expected to affect the emergence of spontaneous synchronization. In case the flaplets were made from a rigid material, the

viscous-coupling effect would disappear completely, as it depends on the cross-talk among the flaplets in from of the bending deflections at their tips. on the other hand, the flaplets cannot be too flexible for the following reasons: (i) The amount of the flaplet bending at the tip needs to be within a reasonable range as a fraction of the beat amplitude so that the current implementation of the clutch control loop can work. (ii) The flaplets need to remain untouched by their beating neighbours during the process of self-synchronization which limits the bending allowance at the tip. (iii) The more flexible the flaplet would be, the less momentum it would transfer to the surrounding fluid, therefore, generating effective propulsion would not be possible. The question of the optimum stiffness of the flaplets is not discussed in the present study. However, the present stiffness was chosen according to the flaplet's geometry and the applied viscous forces such that the maximum deflection at the tip during the self-synchronization process is approximately 25% of the beat amplitude.

As seen from the results, the synchronization is not perfect, as the differences in phase do not converge to the exact same values. Flaplet number  $i = 1$  could not reach the phase relationship to the next as close as the others during the recording period of total number of 18 cycles. This could be related to the non-symmetric boundary effects for flaplet number  $i = 1$  and  $i = 5$ . For both, the beating in direction away from the inner neighbouring flaplets is less influenced by viscous coupling than it is for the inner ones. As a result, the phase synchronization therefore may drift towards lock-on to either of the end flaplets. A definite answer to the boundary effects can only be found by testing a chamber with a circular row of flaplets, which eliminates these effects. However, variations in the phase shifts were also observed in the numerical simulations, even for imposed periodic boundary conditions (Niedermayer et al. 2008, Elgeti & Gompper 2013). Real-time control is, in general, sensitive to time constrains and system internal delays, which may lead to aliasing effects (Grenander 1959). It may take around 0.067 s from reaching the terminal position of the flaplet tip to the action of the flaplet reversing the beat, given by the sampling frequency. At the current tip speed, this delay equates to a possible variability of the amplitude of  $\Delta A/A_i = 0.06$ . This uncertainty introduces a time variant parameter in the system synchronization. However, this random

effect can be fairly neglected compared to the phase shift introduced by the bending of the flaplets due to hydrodynamic interactions, as proven by comparison to the reference measurements in air, see also Fig. 4.6. In addition, during the calibration stage, the five motors were found to have slightly different speeds. Nevertheless, synchronization can even emerge in the presence of different intrinsic beat properties and oscillator noise as long as hydrodynamic coupling is strong enough, see ref (Brumley et al. 2014).

A number of additional results is shown here to address several questions of importance regarding statistics and reproducibility of the results. Fig. 4.7 shows another experiment in the viscous liquid at random initial conditions.

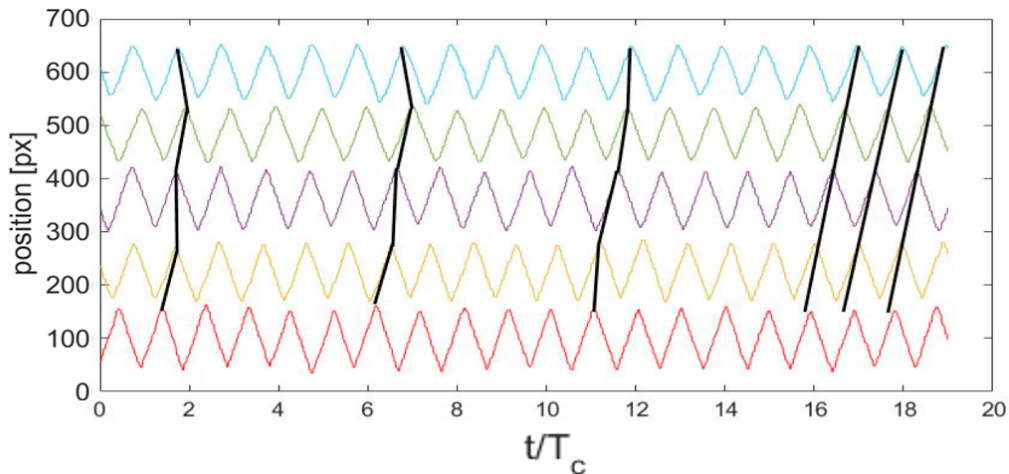


**Figure 4.7:** Repetition of the control experiment in glycerol; compare this to Figure 5b. Note, again, emergence of metachronal coordination after about 15 cycles. Herein, the observed metachronal wave runs in opposite direction to the one documented in Figure 5, bottom. For explanation of the lines see the figure caption in Figure 5.

The results prove that the system again gets into metachronal synchronization after about 15 cycles. Interestingly, while in Fig. 4.5 the metachronal wave runs from left to right (or from flaplet  $i = 5$  to  $i = 1$ ), it is the opposite for the other experiment shown in Fig. 4.7. As the beating profile of the cilia is in principle time-reversible and the cilia shape is symmetric, and all cilia are uniformly spaced, we assume that small deviations from symmetry in the motor response or in the shape of the flaplets or the initial conditions play a role in selection of direction. We even could observe spontaneous symmetry breaking at times larger than 1 min.

However, we could not judge these observations as physically relevant, as they only appeared at much later times, and possible accumulations and aliasing effects as discussed above may then play a role. We believe that the number of cycles to get into synchronization depends on the initial conditions. We also expect a dependency on the Reynolds-number, which is left open for future studies with liquids of varying viscosities.

For further illustration of the variability in the motion pattern, we calculated the variance in the zig-zag type motion by superposition of the individual “triangular cycles” in the zig-zag pattern. For reference, we fixed the tip of each tooth at the position of cycle time equal to 0. From the data superposed in this way, we calculated the probability function to be within a certain radial distance to the mean of the triangular shape using a box-counting method. The resulting distribution is shown as color plot in Fig. 4.8 for flaplet  $i = 2$ . Dark red color means a probability of 1 that this position is reached in all successive cycles in a similar time relative to the cycle maximum (defined by the search radius).

As demonstrated, the air experiment shows a rather sharp-edged triangle with small variations between individual beats. In comparison, the synchronization process in the viscous environment causes larger deviations, especially at the flaplet reversals, where neighbouring flaplets get closer to each other. Further evidence of this variability is demonstrated by comparing the normalized auto-correlation profiles of the flaplet motion as given in Fig. 4.9. The normalized autocorrelation of a perfect zig-zag motion pattern would result in extrema of 1 and -1 at time-lags of even and odd multiples of half of the cycle ratio. For the air experiments, the positive peaks are all above a correlation value of 0.95, shown by the “+” type symbols in the plot. In comparison, in the viscous case successive cycles underlie the documented small variability during the synchronization process; therefore, the correlation peaks decrease with larger time-lags until correlation is fully lost after 8-9 cycles. Similar profiles can be shown also for other flaplets in the row.

In the future, further improvements will be possible on the control loop timing to increase the sampling frequency and thus allow longer periods of study. This can be achieved by embedding the PC monitoring and control logic into the high-speed

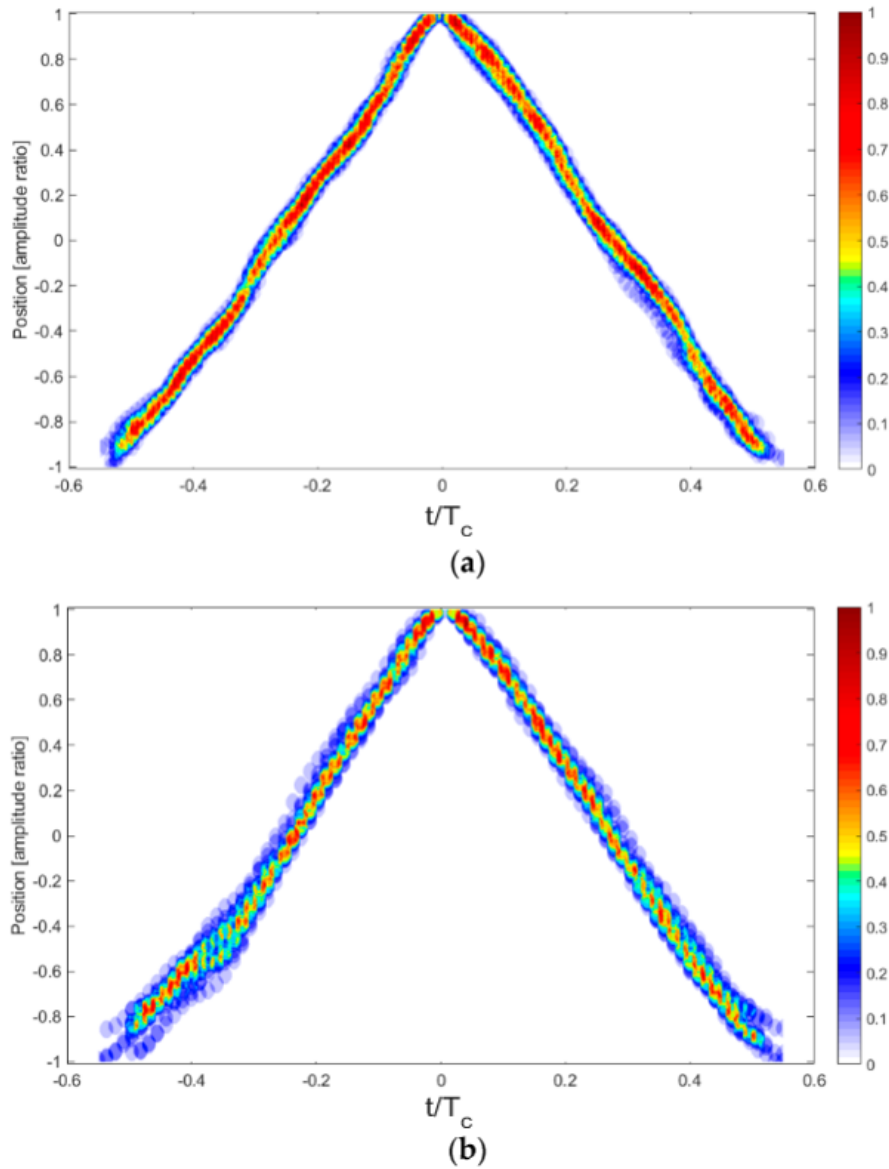


**Figure 4.8:** PDF of the individual “teeth” to overlap with the mean in the zig-zag motion profile for a selected flaplet in air (a) and glycerol (b) for a total period of 1 min. Blue values show a larger deviation from the mean, while red is aligned with the mean of all teeth. Note that all teeth are fixed with their maximum position at beginning of cycle time 0.

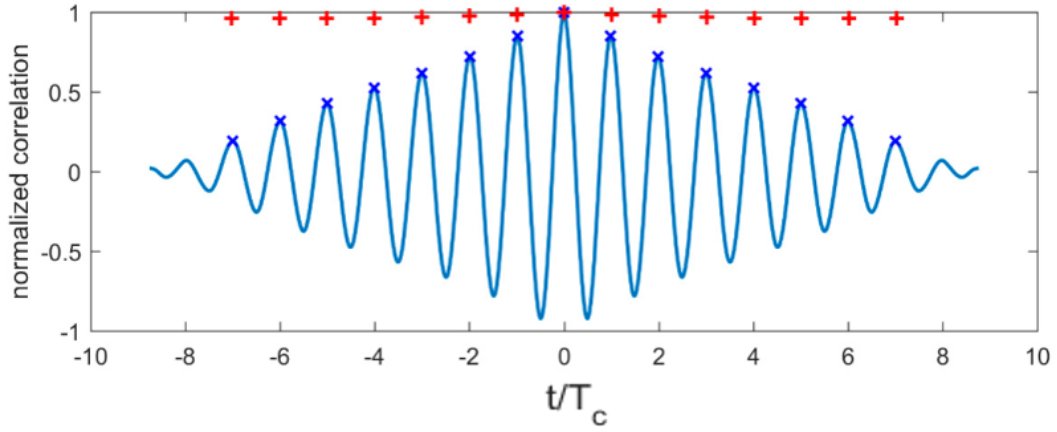


**Figure 4.9:** Peaks of normalized autocorrelation function of the zig-zag motion profile for a selected flaplet in air (red symbol “+”) and glycerol (blue symbol “x”) for a total period of 1 min. For illustration, the continuous auto-correlation profile is added for the case of glycerol as a solid line in blue.

camera processor itself. It will allow for the extension of the studies to a wider range of Reynolds-numbers and parametric variations of the geometry of the cilia. A major difference between biological cilia and the flaplets in our study is their 2D shape with rectangular cross-section. Nevertheless, we expect similar synchronization for cylinders as long as we are in the low-Reynolds regime where the shape of the body loses importance in the presence of viscous forces. Furthermore, the chamber offers optical access to capture the flow details using Particle Image Velocimetry. It might help to further investigate flow field around the flaplets while in coordination.

## 4.5 Critical analysis

### 4.5.1 Overview and study contributions

The study presents the use of flexible two-dimensional flaplets (i.e., rectangular flat plates) to resemble the emergence of spontaneous metachronal coordination of cilia. The conditions to reach synchronization are tested (represented by the bending of the flaplets in response to viscous loads and the control hypothesis that allows the bending to slightly vary the period of individual beats of the flaplets oscillations). Despite the symmetric shape of artificial cilia and the time-reversible actuation of the individual oscillators, a pattern of metachronal coordination of the beating system of five flaplets was reached. A part of the study's results illustrates the variations of the individual beat cycles due to the viscous coupling and compares that to reference conditions when the flaplets beat in an inviscid medium. Further analysis and flow measurements are required to reveal the collective role of the coordination on the surrounding fluid.

### 4.5.2 Exploratory discussion and future work

#### 4.5.2.1 Emergence of metachronal coordination for different shapes of cilia

One major difference between biological cilia and the flaplets in this study is shape. The initial interest was to study a simple 2D system. I expect similar synchronization for other shapes such as cylinders as long as we are in the low-Reynolds regime. The viscous coupling among the cilia, in the presence of a control hypothesis that allows the individual beats to vary according to the applied load, is expected to be the main condition of the emergence in this case. The same behaviour can be replicated for other shapes as well.

#### 4.5.2.2 Dependency of the self-synchronization results on Reynolds number

In general, the spontaneous synchronization of cilia is not confined to a specific Reynolds number. One can witness the natural synchronization of cilia on different scales, ranging from unicellular ciliates such as *Paramecium* to macro-scale Ctenophora such as *Pleurobrachia*. In the current experiment, the variation of the Reynolds number (for example by changing the fluid's viscosity) is expected to affect the degree of viscous coupling of the flaplets. That change may affect the current time-scale to reach synchronization and may also lead to situations where self-synchronization cannot be reached at all due to the current limitations of study period and overshoot accumulations. It would be interesting in a future study to quantify the changes in that time-scale and the resulted steady-state phase shift among the flaplets due to the variation of the Reynolds number. For very high Reynolds numbers, it is expected to lose the synchronization of the flaplets, as their viscous-coupling will then deteriorate in the presence of the strong inertial effects.

#### 4.5.2.3 Limitation of the study period

As explained in section 4.4, the current implementation of the control system has a sampling frequency of 15 *Hz* (i.e., a latency of about 2% cycle time), limited by the hardware and lack of the direct FPGA implementation of the computer-vision code. Therefore, we could quantify a possible error accumulation, which limited the total recording time to about 18–20 cycles, where the observed phase differences in an inviscid medium due to the sampling frequency of the control loop could be neglected in comparison to the phase shifts induced by the viscous coupling in glycerol. We could run the control loop beyond this time, however, we could not guarantee that – from there on – the observed change in phase relationships is physical or induced by the level of overshoot-error accumulations. Following the present study, the beating system of the flaplets along with the surrounding hydrodynamic interaction forces were mathematically modelled thus allowing long periods of study. These results are illustrated in chapter 5.

#### **4.5.2.4 Parameters affecting the deflection values of the flaplets**

The deflection values of the flaplets are expected to depend on the flaplet material, the speed of their oscillations and the viscosity of the surrounding fluid. If we change the level of maximum deflection to lower values relative to the spacing of the flaps, we might lose viscous coupling, thus the observed effect is expected to deteriorate. The chosen value is such that the flap tips just don't touch in the most critical situation when the phase is  $180^\circ$ , i.e. anti-phase motion between pairs, plus a safety distance due to the small latency in the online image processing.

#### **4.5.2.5 Two-dimensionality of the study's dynamics**

The displacements of the flaplets' tips are nearly homogeneous along the span of the flaps. The flow resulted from coordination is expected to be three-dimensional along the lateral edges of the flaplets while it is nearly two-dimensional at the centre of the flaplets. This can be further investigated by direct flow measurements of the flow field in the coordinated state of the system. The flow visualization results are discussed in chapter 5.

#### **4.5.2.6 Breaks in the spontaneous coordination**

We could observe a spontaneous process of breaking of the synchronization after it had been formed. However, we cannot judge this observation since it may be affected by the accumulation of the overshoot errors and the variations in the motors' speed responses reported earlier. A definite answer is given by the development of a mathematical model that fairly describes the system dynamics and behaviour with time and then investigating the stability of the emerged coordination. The model is introduced in chapter 5.

On the other hand, the fluctuations in the control loop and the resulted coordination can be subsumed as fluctuations in the flaplets' driving forces. In fact, natural flagellar driving forces also possess fluctuations that had been observed experimentally (Ma et al. 2014). Overshoots in the individual beats and breaking of symmetry have been reported both in experiments and numerical models of self-

synchronization (an example is presented in section 2.2.4).

### 4.5.3 Flow propulsion as a consequence of metachronal self-coordination

At viscous environments, time-reversible gait of the swimmer as a whole cannot induce net propulsion. However, time-symmetric actuation of individual oscillators in our system does not necessarily result in a time-reversible gait of the system as a unit. In order for the system gait to be time-symmetric, the system needs to undergo a sequence of motions in a given stroke and reverts back to the starting configuration by going through the same sequence in reverse (this part is explained in detail in section 2.2.5). In this way the time-reversed recording of the system motion does not vary from the original (the property of time-reversibility). In the present system, this is the case for in-phase  $\Delta\phi = 0$  and out-of-phase synchrony  $\Delta\phi = 180$  of the beating flaplets. In these two special cases, if the experiment is stopped when one of the flaplets reaches its limit amplitude and then the motion is reversed, it would not be different from continuing with the original motion without stopping the experiment, see Fig 4.10a.

On the other hand, if the emerged coordination is found to have a pattern that is neither an in-phase nor out-of-phase coordination  $0 < \Delta\phi < 180$ , there will exist a running wave on the flaplets' surface whose direction would be reversed in case the experiment is stopped at any moment and the motion sequence is reversed, see Fig. 4.10b. Therefore, I expect the system as a unit to violate the symmetry argument of the scallop theorem and hence generate propulsion in such cases of metachronal coordination. A definite answer would be possible by examining the forces build-up on the oscillators during self-synchronization and measuring the flow field after reaching the coordinated state, both of which is presented in chapter 5. It is also worthy to mention that micro-swimmer examples have been already realized that use time-symmetric actuation of individual oscillators and yet could violate Purcell's symmetry arguments using strategies other than metachronal coordination (Lauga 2011).

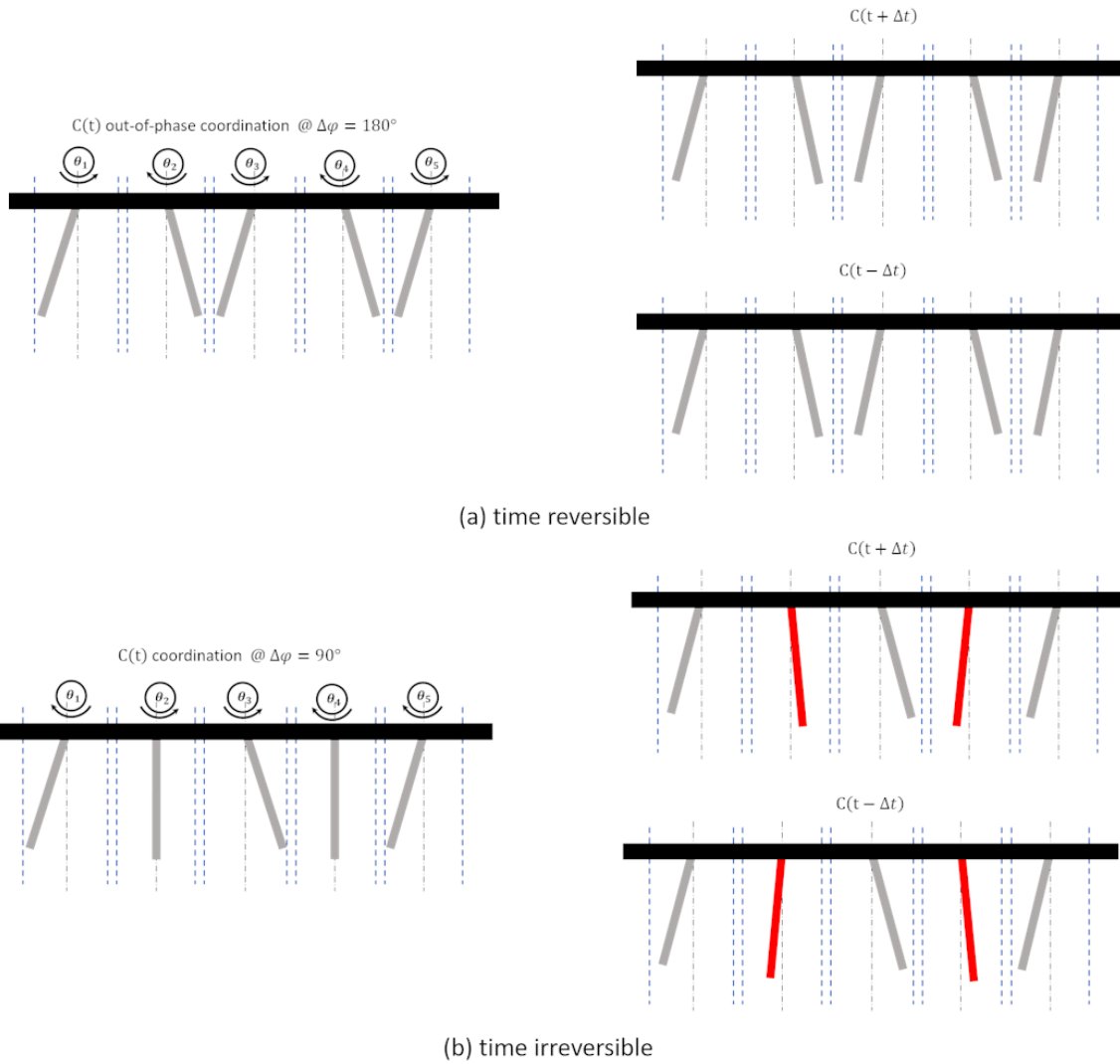


**Figure 4.10:** Illustration of the time-reversibility principle for the phase-coordination of five flaplets; (a) out-of-phase  $\Delta\phi = 180^\circ$  coordination of the flaplets as a time-reversible gait sequence; (b)  $\Delta\phi = 90^\circ$  coordination of the flaplets as a time-irreversible gait sequence. The sequence in (b) violates the Purcell's symmetry arguments and therefore is expected to generate uni-directional net transport of the surrounding fluid.

# Chapter 5

## Simulation of Self-Coordination in a Row of Beating Flexible Flaplets for Micro-Swimmer Applications: Model and Experiment Study

### Abstract

In this study we present a model that simulates hydrodynamic self-coordination in a row of flexible flaplets. We control the flaplets in order that their tips follow a fixed-amplitude oscillatory motion profile. When brought together at a low Reynolds-number environment, the flaplets interact with each other in the form of bending deflections at their tips, which causes the frequency of the individual oscillations to vary until a coordinated steady state is reached. The model design steps are experimentally verified and the coordination results of both the experiment and the model are compared. The model's internal states are then analysed for a better understanding of the synchronization collective effect. The coordination of the flaplets is found to settle in the direction of propulsion forces ascent. The stability of the resulted synchronization and propulsion forces are examined over long periods. The model is meant to be simplified and mostly linear so that it can be utilized for state forecasting in a real-time control application of a swimmer robot. Finally, we experimentally study the propulsion performance of five beating flaplets that follow prescribed oscillation profiles forming a metachronal wave. The flow results show that the flaplets, that beat in coordination, are efficient at generating

a uni-directional steady-streaming transport of the fluid at their surface.

## 5.1 Introduction

Nature is full of examples where a collaborative behaviour rises due to different body reactions and surrounding environmental properties (Beckers et al. 1989, Allan et al. 1996, Ball 2013). One of these examples is the hydrodynamic coordination of flagella and cilia in biology. Sperms while swimming interact with the surrounding semen and with each other forming a kind of cluster (Yang et al. 2008). In human windpipes, cilia beat in a coordinated pattern while sweeping mucus and dirt outside of the lungs (Shih et al. 1977). Similar coordination of cilia is witnessed at the surface of many ciliated organisms (Ricci 1990, Machemer 1974, TAMM 1973). Each cilium is found to maintain a certain phase shift to its neighbours while beating, forming a pattern that is known as a metachronal wave (Eshel & Priel 1987). It is believed that when brought together, cilia are coupled by the surrounding viscous forces of the fluid and over time they appear to organize their oscillations allowing this collective state to spontaneously emerge (TAMM 1973, Niedermayer et al. 2008, Golestanian et al. 2011, Brumley et al. 2014, Bruot & Cicuta 2016). Previous numerical models and experiments have shown that hydrodynamic forces can bring different types of oscillators that are close to each other to various forms of self-organization (Kotar et al. 2010, Di Leonardo et al. 2012, Putz & Yeomans 2009, Niedermayer et al. 2008, Elgeti & Gompper 2013, Elshalakani & Brückner 2018), even with breaks in their steady-state phase relationships (Niedermayer et al. 2008, Elgeti & Gompper 2013).

In the world of ciliated micro-swimmers, the viscous forces are dominant and fluid propulsion cannot be created by a time-symmetric oscillator as explained by the scallop theorem (Purcell 1977). Consequently, most of the developed swimmer models or designs at low Reynolds numbers adopt the actuation of non-reciprocal motion profiles. Some examples of these designs are swimmers made of: (1) asymmetric rod joints (Becker et al. 2003) (2) soft deformable interfaces (Mason & Burdick 1999, Trouilloud et al. 2008) (3) connected spheres with certain kinematic inter-relations (Earl et al. 2007, Dreyfus, Baudry & Stone 2005, Najafi & Golestanian 2004). (4) helical vibrating interfaces (Gao et al. 2014, Xu et al. 2014). In such non-reciprocal motion profiles, the asymmetry of the generated viscous forces in-

duce a net propulsion force in a certain direction (Kim et al. 2016, Abbott et al. 2009). That said, when a model of artificial cilia, that can be magnetically actuated to follow non-reciprocal beating profiles, was examined in (Gauger et al. 2009), it was shown that the pumping performance of interacting coordinated cilia was significantly higher than that of separate ones. Similarly, in (Blake & Sleight 1974, Bruot & Cicuta 2016), it is stated that the coordinated beating of cilia is particularly effective at maintaining more directed surface propulsion. It has been also shown that the propulsive effect of a system of pneumatically controlled flexible oscillators is strongly affected by their phase relationships (Rockenbach et al. 2015). Accordingly, we suggest that the metachronal coordination of a system of individual oscillators can itself result in collective propulsion if the oscillators are brought together in a sufficiently-viscous environment.

Generally, further progression to realistic micro-swimmer robotic applications faces two main challenges; (1) the design and control of applicable propulsion mechanisms and (2) the minimization of the actuation power (Cho et al. 2014). In case of using oscillating elements to generate propulsion, a minimum of two degrees of freedom per each element is required to be controlled to satisfy the desired non-reciprocal motion profiles (Kim et al. 2016). In some models, even the shape of the elements is required to be changed during different parts of the beating cycle which brings more complexity to the system and control (Gauger et al. 2009). Additionally, most of the micro-swimmer models are usually developed using multi-particle collision dynamics (MPC) (Kapral 2008, Elgeti & Gompper 2013) or other numerical solutions. Since the computations of finite element models are time-consuming, the real-time tracking of the robot's internal states using such models is not possible. Hence, we claim that swimmer designs with linearized and fast-computed models could facilitate better control and observation of such systems.

In this article, we firstly test the emergence of metachronal coordination in a row of flexible flaplets at a low Reynolds number by means of an experimentally-validated model. A single-degree-of-freedom oscillatory motion is controlled by an algorithm that is based on the geometric clutch hypothesis (Lindemann 1994) where the individual oscillations are bounded in amplitudes and free in phase and frequency. The

induced bending of the flexible flaplets in the presence of a viscous medium allows for the crosstalk to take place within the beating system. The net swimming force that acts on the system is derived from the introduced model. The force response shows that the resulted synchronization can be accompanied by a net swimming effect. Then, the stability of the emerged synchronization is analysed over long periods showing that the emergence of synchronization can have a predictable steady-state behaviour. Finally, we experimentally visualize the flow field around the physical system using Particle Image Velocimetry (PIV) while the flaplets are beating in metachronal coordination. The measurement of the flow velocity field allows us to quantify the net pumping effect due to the coordinated beating of the flaplets.

## **5.2 Concept formulation**

### **5.2.1 Model objective**

We aim at studying the transformation of an oscillating system of beating flaplets from a chaotic to a coordinated pattern by means of an experimentally identified model. The key factors to get into coordination are the flexibility of the structures and the viscous coupling among them. A biological control hypothesis introduced by Lindemann (1994) is implemented as the control algorithm, which follows the “geometric clutch”. From there on, we look forward to highlighting the collaborative swimming effect of the resulted coordination and study its stability.

### **5.2.2 Material and environment**

The proof-of-concept experiment of self-synchronization in a row of flexible flaplets was reported in detail in chapter 4 and the reader is referred to it. Herein, the experiments are used to identify the parameters of the lumped element model of the flaplets. The physical problem of the bending of a thin flexible plate in a viscous environment is described by the two non-dimensional numbers, the Reynolds-number

$Re$  and the Cauchy number  $C_Y$ :

$$Re = \frac{UL_c}{\nu} \quad (5.1)$$

$$C_Y = \frac{\frac{1}{2}\rho U^2}{EI} \quad (5.2)$$

with  $\nu$  being the fluid's kinematic viscosity,  $U$  the relative speed scale between the oscillator and the fluid,  $L_c$  the characteristic length in the problem geometry,  $EI$  the flexural rigidity of the flaplet and  $\frac{1}{2}\rho U^2$  the dynamic pressure in the given problem. The Cauchy number characterizes the deformation of an elastic solid under the effect of a surrounding flow (De Langre 2001). It is defined as the ratio between the force produced by the dynamic pressure of a flow on the flaplet surface and the bending rigidity of the rectangular flaplet.

The configuration under investigation herein is for a Re-number in the range of  $Re \in [0.1, 1]$  and a Cauchy-number of order  $C_Y = O(10^{-1})$ . The method of dynamical similarity (Batchelor & Batchelor 2000) enables us to use the results of an enlarged experimental model to investigate an observation that happens at a much smaller scale. It also enable us to use normalized quantities of size and speed in our theoretical model.

## 5.3 Experiment description

### 5.3.1 Set-up and control loop

The laboratory experiments were conducted with a row of five rectangular flaplets. The experimental set-up is illustrated in detail in section 4.2 in the previous chapter. In order to further highlight the geometrical parameters used in modelling, we present Fig. 5.1 showing different views and schematic drawings of the experimental facility and the flaplet.

Each flaplet is controller to perform an oscillatory motion profile around its equilibrium position (where all oscillators are vertical). The amplitude of oscillations is selected so that the flaplets are not allowed to touch each others while beating.

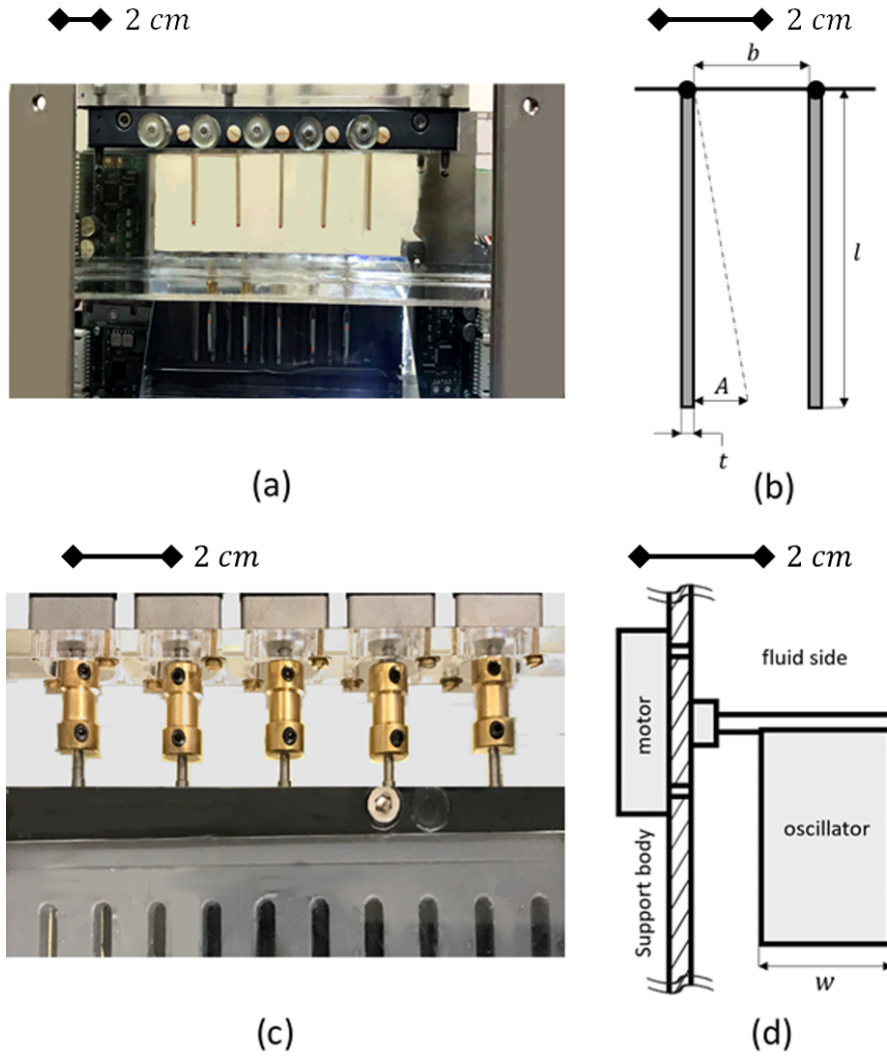


**Figure 5.1:** The experimental set-up of the five flexible flaplets in the viscous chamber. Each flaplet is clamped from one end to the spindle axle of a rotary motor. (a,b) front view (c) top view (d) side view (b,d) schematic drawings that show the geometrical parameters of the flaplets.

Therefore, a minimum distance,  $r_{min} \simeq 0.2A$ , between the tips is set at the nearest angular positions of a neighbouring couple of flaplets to allow for their bending deflections. We represent the distance  $r$  between the tips with an offset equal to the value of  $r_{min}$  so that;  $r = 0$  when the tips are  $|r_{min}|$  apart.

The optical set-up and the control algorithm are detailed in sections 4.2.2 and 4.2.3 in the previous chapter. Fig. 5.2 shows a graphical description of the implementation of the control loop. It is important to note that the control algorithm is a vision-based implementation of the geometric clutch hypothesis that provides a geometrical mechanism of oscillations in biological swimmers (Lindemann 1994).

As an alternative to the camera, strain gauges can be also used to measure the deflection values at the tips used for the control of the flaplets' oscillations.

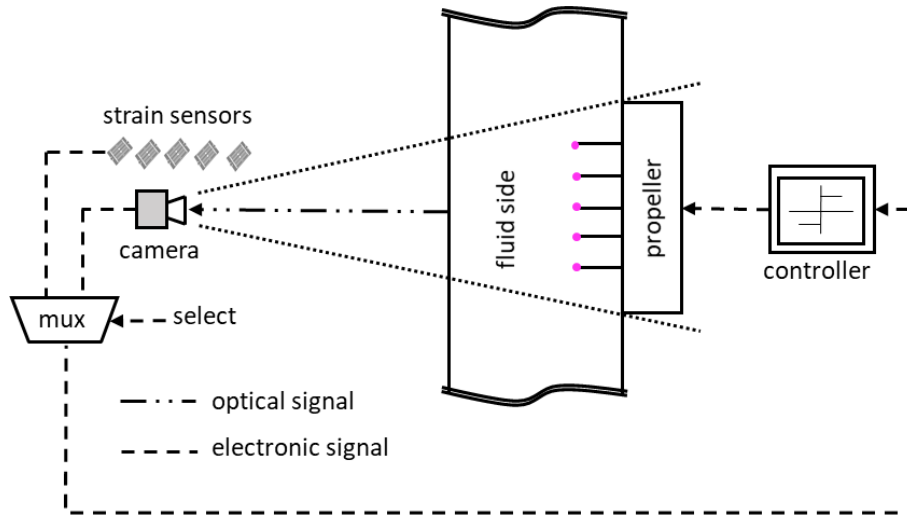


**Figure 5.2:** Physical implementation of the control closed-loop based on the geometric clutch hypothesis. The feedback signal is the position of the oscillators' tips that are marked with florescent dyes which can be captured by the high-speed camera. Another measurement of the feedback signal is applicable by the use of strain gauges that can capture the tips' deflection.

## 5.4 Theoretical modelling

We aim to introduce a simplified model of the experiment to study the synchronization behaviour for longer periods and a larger number of flaplets. The fluid–structure interaction is approximated by a representation of the individual flaplets as flexible cantilever beams (Euler–Bernoulli beam) actuated by the individual motors and reacting to the surrounding viscous forces. Each flaplet is modelled as a second-order system with a lumped element model while the build-up of the viscous interaction forces in the fluid is modelled as a first-order system with a relatively small time constant. The model is simplified and aligned with the experimental results. We expect that the simplicity of the model would be a significant advantage because, as elaborated later, the resulting coordination is found to be accompanied with the emergence of propulsion forces which qualifies the model for micro-swimmer applications. Hence, the observability and fastness would allow the model to be used for control design optimization and online state forecasting of swimmer robots in future applications.

### 5.4.1 Mathematical description

In this section, we introduce the analytical equations that describe the behaviour of each oscillator while beating. Since the flaplets are identical, we can expand this model to describe a row of beating flaplets. The model equations are deduced and identified with the help of experimental and numerical data perceived from literature and tests in the experimental setup. The modelling design steps are comprehensively and experimentally validated. A detailed derivation of the mathematical model is provided in appendix A.

Table 5.1 and Fig. 5.3 illustrate the system parameters that come from the theoretical model of a single flaplet. The parameters are divided into the following four categories:

1. **Set parameters:** these are the nominal constants that are given by the experimental setup and geometry.
2. **Input variables:** these are the variables that are controlled by the operator or changed according to the states of the neighbouring flaplets. The flaplet perceives the inputs and responds accordingly in the form of rotation and bending deflection.
3. **System states:** these form a set of variables that fully describe the flaplet at a given instance in time.
4. **Output variables:** the response of the oscillator derived from the system states at a given instance.

In this case, we are particularly interested in the position trajectory of the flaplets' tip because the control loop uses this position as the feedback signal. Before we start, we normalize all the system parameters against their nominal values to obtain a scalable dimensionless system of equations. The parameters of length units are divided by the amplitude of oscillation,  $A$ . The angular velocities are divided by the nominal speed,  $\omega_0$ . We represent the normalized parameters in the equations with the superscript notation  $^{*}$ .

**Table 5.1:** Description of the parameters of the mathematical model

Symbol	Description	value
<b>Set Parameters</b>		
$\omega_0$ [ $rad \cdot s^{-1}$ ]	angular speed of the attached motor	0.267
$A$ [ $m$ ]	limit amplitude of the tip position trajectory	$9 \times 10^{-3}$
$T_c$ [ $s$ ]	nominal cycle period of the oscillatory motion	$4A/(\omega l)$
<b>Input Variables</b>		
$\omega$ [ $rad \cdot s^{-1}$ ]	angular velocity of the flaplet	$\pm\omega_0$
$\omega_{r,l}$ [ $rad \cdot s^{-1}$ ]	angular velocity of the right/left neighbour	$\pm\omega_0$
$d_{r,l}$ [ $-$ ]	normalized relative angular velocity of the right/left neighbour	$(\omega_{r,l} - \omega)/\omega_0$
$r_{r,l}$ [ $m$ ]	absolute distance from the oscillator's tip to the right/left neighbour's tip	
<b>System States</b>		
$\theta$ [ $rad$ ]	angular position of the straight oscillator (without accounting for the bending)	
$\gamma_o$ [ $m$ ]	deflection of the tip due to its rotation in the viscous liquid	
$\gamma_{r,l}$ [ $m$ ]	deflection of the tip due to interaction with the right/ left neighbour neighbour	
$\gamma_t$ [ $m$ ]	total dynamic deflection at the oscillator's tip	
<b>Output Variables</b>		
$y$ [ $m$ ]	position of the oscillator's tip at a given set of states	
<b>Identified Parameters</b>		
$C$ [ $m^{-5}$ ]	constant relating the deflection of the tip to the rotation velocity; given by Eq. 3	$1.4 \times 10^5$
$T$ [ $s$ ]	time constant of the first order lag given by Eq. 3, 4	$0.02T_c$
$m$ [ $kg$ ]	mass of the second-order system given by Eq. 5	$3.4 \times 10^{-3}$
$b$ [ $kg \cdot s^{-1}$ ]	damper factor of the second-order system given by Eq. 5	0.22
$k$ [ $N \cdot m^{-1}$ ]	spring stiffness of the second-order system given by Eq. 5	3.54

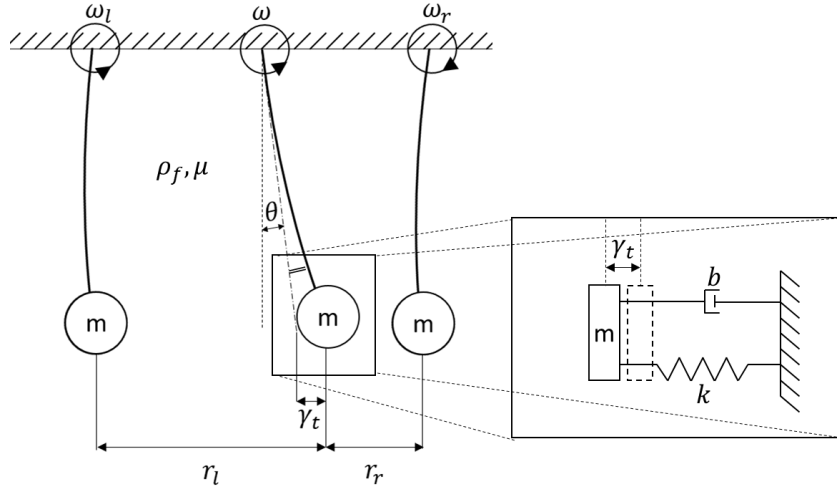


**Figure 5.3:** Lumped element model of the flaplet highlighting the viscous-coupling parameters. The description of the model parameters is provided in Table 5.1.

The material of the oscillators is flexible in order to allow bending to take place as a result of the applied viscous forces. In the experiment, the viscous forces acting on the oscillator induce dynamic deflection,  $\gamma_t$ , at the tip. The magnitude of that deflection is always small enough compared to the length;  $\gamma_t \leq 0.05l$ . By neglecting the shear and torsion stresses on the flexible flaplet, it can be modelled as a simple beam that experiences bending deflections while rotating.

In order to obtain the position of the tip as a function of time, we present the following set of differential equations. The description of the model parameters is given in Table 5.1. References to the corresponding equations in appendix A is provided in bold font after each equation.

$$T\dot{\gamma}_o^* = -Cl^5\omega^* - \gamma_o^* \quad (\mathbf{Eq. 16, 18}) \quad (5.3)$$

$$T\dot{\gamma}_{r,l}^* = u_{r,l} - \gamma_{r,l}^* \quad (\mathbf{Eq. 17, 18}) \quad (5.4)$$

$$u_{r,l} = \begin{cases} 0.013d_{r,l} & r_{r,l}^* > 1 \\ d_{r,l}(-0.082r_{r,l}^* + 0.095) & r_{r,l}^* \leq 1 \end{cases}$$

$$m\ddot{\gamma}_t^* = k(\gamma_o^* + \gamma_r^* + \gamma_l^*) - b\dot{\gamma}_t^* - k\gamma_t^* \quad (\mathbf{Eq. 19}) \quad (5.5)$$

$$y^* = \frac{l}{A}\theta + \gamma_t^* \quad (5.6)$$

## 5.4.2 State-space model

The above illustrated mathematical equations are gathered into a MISO state-space model that fully describes the dynamics of each oscillator. The model is given in the state-space standard form as described by Eqs. 5.7, 5.8. Since all equations are dimensionless, we then represent the normalized parameters in the state-space model without the superscript notation ‘\*’, for the sake of simplicity.

$$\begin{bmatrix} \dot{\theta} \\ \dot{\gamma}_o \\ \dot{\gamma}_r \\ \dot{\gamma}_l \\ \dot{\gamma}_t \\ \ddot{\gamma}_t \end{bmatrix} = \begin{bmatrix} 0 & 0 & 0 & 0 & 0 & 0 \\ 0 & \frac{-1}{T} & 0 & 0 & 0 & 0 \\ 0 & 0 & \frac{-1}{T} & 0 & 0 & 0 \\ 0 & 0 & 0 & \frac{-1}{T} & 0 & 0 \\ 0 & 0 & 0 & 0 & 0 & 1 \\ 0 & \frac{k}{m} & \frac{k}{m} & \frac{k}{m} & \frac{-k}{m} & \frac{-b}{m} \end{bmatrix} \begin{bmatrix} \theta \\ \gamma_o \\ \gamma_r \\ \gamma_l \\ \gamma_t \\ \dot{\gamma}_t \end{bmatrix} + \begin{bmatrix} \omega_0 & 0 & 0 \\ \frac{-Cl^5}{T} & 0 & 0 \\ 0 & \frac{1}{T} & 0 \\ 0 & 0 & \frac{1}{T} \\ 0 & 0 & 0 \\ 0 & 0 & 0 \end{bmatrix} \begin{bmatrix} \omega \\ u_r \\ u_l \end{bmatrix} \quad (5.7)$$

$$y = \begin{bmatrix} \frac{l}{A} & 0 & 0 & 0 & 1 & 0 \end{bmatrix} \begin{bmatrix} \theta \\ \gamma_o \\ \gamma_r \\ \gamma_l \\ \gamma_t \\ \dot{\gamma}_t \end{bmatrix} \quad (5.8)$$

In Fig. 5.4, we present a comparison between the experiment and the model results of the deflection of a flaplet’s tip due to the oscillation of its neighbour. The plot demonstrates the ability of the model to fairly capture the dynamic interaction between the neighbouring flaplets during the different phases of the beat cycle. Although minor deviation between the two responses can be observed, we assume that it does not affect the resulted variation of the beat cycle period during the

transition from a chaotic to a coordinated beating pattern as illustrated in the next section.

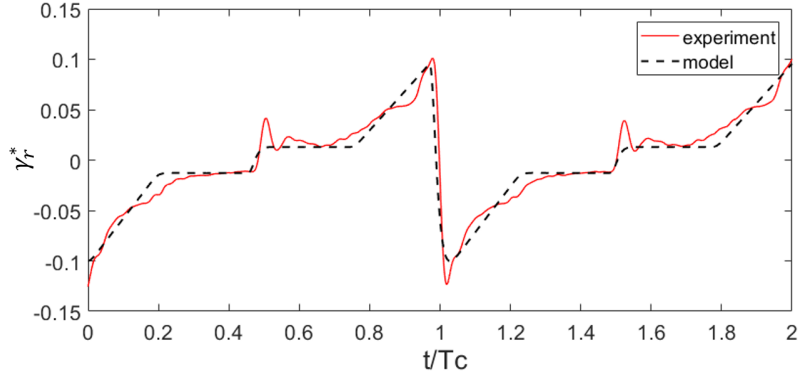


**Figure 5.4:** Normalized deflection of a still flaplet’s tip due to the oscillation of its right neighbour during two successive beat cycles. The distance  $r$  between the two neighbouring tips varies in the domain  $0 < r < 2A$  during a beat cycle.

## 5.5 Results and analysis

The system is configured with the same setup as in the physical experiment in order to test the spontaneous emergence of synchronization among the oscillators and compare the results of both the model and the experiment. The synchronization is considered to start when the oscillators start to beat with the same frequency while keeping a certain phase shift between each other forming a metachronal wave. The experimental control loop algorithm is applied to the model as well. After investigating the emergence of hydrodynamic synchronization among the flaplets, the internal states of the system are analysed to better understand the synchronization effects.

### 5.5.1 Hydrodynamic synchronization

Starting from random initial angular positions, 32 oscillators are brought together and allowed to interact by the help of their modelled bending deflections due to the surrounding viscous forces. The system as a unit could clearly show the emergence of metachronal coordination. Fig. 5.5 shows a colour representation of the position trajectories of individual oscillator tips as a function of the number of beat cycles. A

straight uni-coloured line in the figure indicates a uniform inter-phase relationship throughout the system and hence metachronal coordination. The model has been rendered several times with different random initial positions. At each time, the system has eventually come into a synchronized state at which the phase slopes throughout the whole system remain the same. For different initial conditions, the emergence is found to choose between two steady-state phase slopes with the same slope magnitude but opposite directions. In other words, the uni-coloured lines at the steady state make an angle with the direction of time increase that can take the two values:  $\alpha$  and  $(180-\alpha)$ . We believe that the dominating direction depends on the initial conditions and decides the direction of the swimming forces build-up (discussed in the next section). Sometimes, either the very first or the very last oscillator at the edges appears to slightly lag the others during the synchronized state until it gradually joins the synchronization after a long term. As the edged oscillator, the cross-talk with its neighbours takes place on one side only and therefore it can be less sensitive to the viscous coupling.

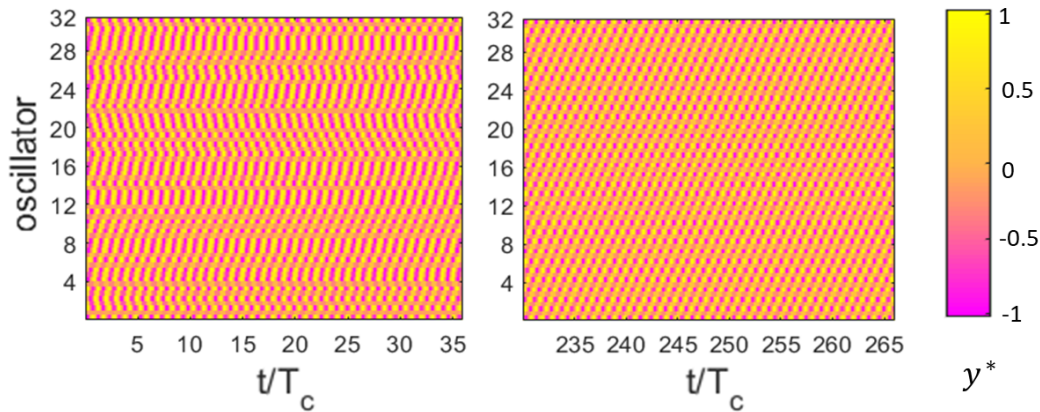


**Figure 5.5:** Position trajectories of 32 oscillators' tips in the modelled viscous environment. The randomness in the phase relationship is shown as curvy lines at the start of the beating (left). The emerged synchronization is shown as straight (constant slope) lines after 225 cycles from the start of beating (right)

The spontaneous synchronization could also be witnessed in experiment for five oscillators while beating inside the glycerine fluid. Starting from different phase shifts between each couple of neighbours, the system has come into synchronization after multiple cycles. Fig. 5.6 shows a comparison between the emerged synchronization for five oscillators in the model (top) and in the experiment (bottom). As the

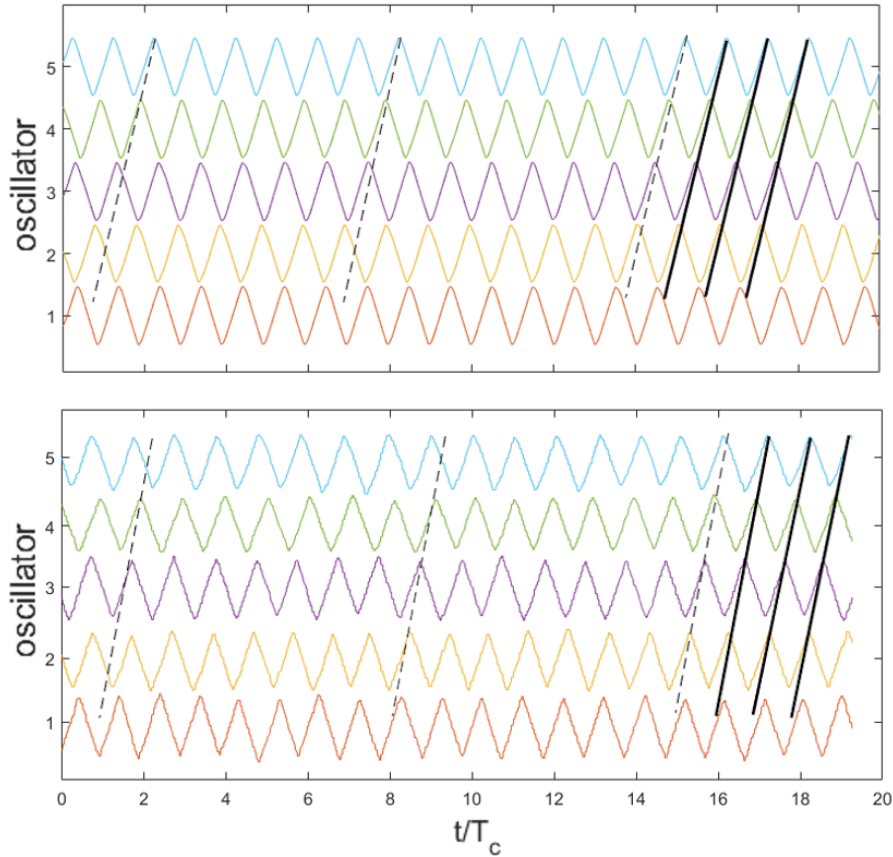


**Figure 5.6:** Evolution of synchronization in a row of five flexible oscillators in the model (top) and in the experiment (bottom). The different colours indicate different oscillators. The solid lines indicate a constant phase slope among four neighbouring oscillators and the dash lines are parallel to the solid ones and show the deviations from coordination at the early stages.

oscillator moves inside the viscous fluid, it interacts with its neighbours in the form of bending. This results in time-variant velocities of the tips and phase relationships among the neighbouring oscillators. This behaviour lasts until the synchronization is reached when each oscillator maintains a certain phase lag with its neighbour that is constant among the beating system. The solid lines in the figure show a constant phase slope that indicates the start of synchronization in both cases. The dash lines that overlay the position trajectories are parallel to the synchronization lines. They show the different phase relationships between the adjacent oscillators at the start of beating and during the evolution of synchronization.

## 5.5.2 Net propulsion force

In this section, we investigate the ability of the mechanism to generate a net propulsion force from the action of the group of beating flaplets. The modelled forces acting on each oscillator are extracted from the system's internal states during the run-time such that:

$$f_m(t) = k\gamma = k(\gamma_r + \gamma_l + \gamma_o)$$

The force that acts on a single oscillator is dependent on the phase relationship of the neighbours and takes the form of a quasi-harmonic function. In order to represent the effective swimming force, a cyclic average of the harmonic force signals as a function of time is calculated. The total effective swimming forces,  $F_t$ , is then represented as the summation of the single forces for all the oscillators in the system.

$$\begin{aligned} f_{av}(n) &= \frac{1}{T_c} \int_{(n-1)T_c}^{nT_c} f_m(t) dt, \quad n \in \{1..300\} \\ F_t(n) &= \sum_{i=1}^N f_{av}^i(n) \end{aligned} \tag{5.9}$$

where  $N$  is the total number of oscillators rendered in the model and  $i$  is the oscillator index.

We found that a net propulsion force starts to emerge as the system is forming a coordinated pattern of oscillations. The gradual build-up of the propulsion forces can be tracked during the coordination build-up when the damping of the system is sufficiently high. This is implemented in the model by increasing the damping of the flaplet's dynamic model. It can be also realized in experiment by selecting a flaplet material of a lower Young's Modulus or moment of inertia.

Fig. 5.7 shows the temporal evolution of the normalized total force,  $F_t/N$ , acting on a model of 32 and 16 oscillators at a high damping  $\zeta = b/\sqrt{km} \simeq 3$ . The resulted synchronization is found to build up in the direction of the increase of swimming effective forces and hence increasing the efficiency of propulsion. It is observed that even the undetectable small phase variations during the synchronized state (after

reaching the straight slope lines in the position trajectories) result in a noticeable gain in the total effective forces. The periods after synchronization lines appear in the two models are highlighted in Fig. 5.7 by the blue- and red-shaded areas. Notice that the force gain, that is bounded by the dash lines in the figure, takes place in during these shaded periods.

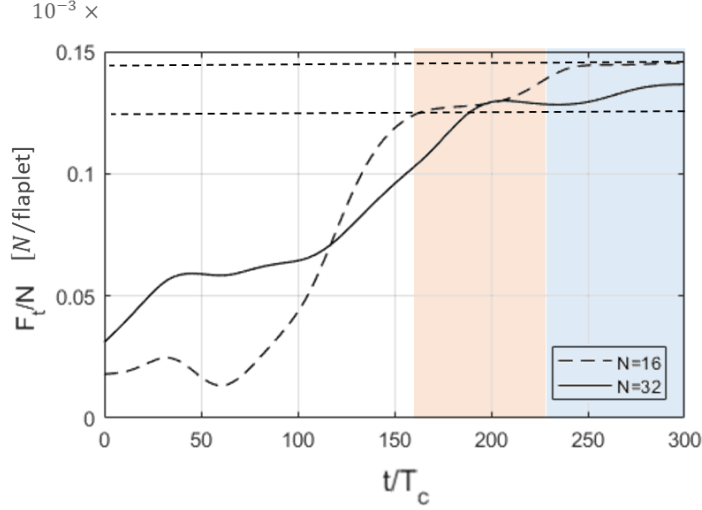


**Figure 5.7:** Evolution of the net propulsion force that arises due to the emerged synchronization at  $\zeta \simeq 3$ . The presented results are for 32- and 16-oscillator models respectively. The shaded areas represent the period after the synchronization lines (constant slope lines) are witnessed in the tips' position trajectories (red for  $N = 16$  and blue for  $N = 32$ ). The blue area is shown on top of the red area which also covers the part beneath it. The dash lines bound the growth in the effective forces due to barely noticeable deviations in the phase slopes during the coordinated state.

An interesting observation from the force response analysis is the stair-wise increase in the force build-up during the emergence of coordination. During the early stages, until approximately 50% of the settling time, the synchronization build-up is partial and separate segments of synchronized 3 to 4 neighbouring oscillators are formed. However, this is not reflected as a global increase in the effective swimming forces. The reason is that there are counteracting segments that are synchronized in opposite directions (slope angles of  $\alpha$  and  $180 - \alpha$ ) and therefore, the net propulsion force is not rising. After this period, a global tendency towards the final synchronization direction starts to emerge and the effect of this tendency is then clearly witnessed as an effective force build-up. The resulted net propulsion force is almost proportional to the number of flaplets in the system.

### 5.5.3 Stability of the synchronization

As demonstrated by Fig. 5.5 (right), once the model reaches its synchronized state, it remains in that state and the synchronization does not break. Since the main goal of the model is to prove the emergence of both synchronization and propulsion, we choose the total effective force,  $F_t(n)$  defined in Eq. 5.9 to study its long-term behaviour using the Lyapunov criterion. For a system of 32 oscillators we select  $F_t(300)$  as the position of rest,  $F_t(e)$ . By computing  $F_t(n)$  over a long period ( $n = 10^3$ ), we find that;

$$\forall n > 280 \quad \exists \epsilon < 0.01F_t(e) \quad [ \|F_t(n) - F_t(e)\| < \epsilon ]$$

This means that starting from any position close enough to  $F_t(e)$ , the value of  $F_t(n)$  remains close enough to  $F_t(e)$  and within a range which does not exceed 1% of its value. Upon this analysis the synchronized system of 32 oscillator is Lyapunov stable.

A strong correlation could also be noticed between the initial conditions and the settling time the system takes until the position of rest is reached. In a robotic swimmer application, it is recommended to include a supervisory controller that can use the real-time model for state forecasting (as a state observer) and impose a set of initial conditions that would minimize the settling time. That said, we believe that even the maximum settling periods reported do not represent a problem in case of a micro-swimmer application. The smaller the size scale of the swimmer body and the inter-spacings is, the higher the beating frequency of oscillations that would keep a low Reynolds number. In recently reported micro-swimmer studies, the beating frequency reaches up to 60 *Hz* (Kim et al. 2016). This frequency boost would result in a faster emergence of the required propulsion forces.

## 5.6 2D flow visualization

In this section, we experimentally test the system capability to generate a coherent directed transport at the surface of the oscillators during metachronal coordination.

In order to visualize the flow near the flaplet's surface, a Particle-Image-Velocimetry (PIV) measurement is prepared. Due to optical obstruction, the flow measurement cannot be carried out simultaneously while running the vision-based control loop. Therefore, an open-loop control algorithm is implemented to drive the five motors at a predefined amplitude, frequency and phase difference between each adjacent couple of motors. We define a general oscillatory profile of the motors as a triangle-wave form of  $\theta$  which is described as a function of time  $t$  in the following equation:

$$\theta(t) = \frac{4A_\theta}{T_c} \left( t - \frac{T_c}{2} \left\lfloor \frac{2t}{T_c} + \frac{1}{2} \right\rfloor \right) (-1)^{\lfloor \frac{2t}{T_c} + \frac{1}{2} \rfloor} \quad (5.10)$$

where the symbol  $\lfloor i \rfloor$  is the floor function of the number  $i$  and  $A_\theta$  is the amplitude of the angular position of the motors. The trajectory of the  $n^{\text{th}}$  motor's rotation follows the profile prescribed by:

$$\theta_n(t) = \theta(t - jT_c(n - 1)), \quad n \in \{1..5\}, \quad j \simeq 0.2 \quad (5.11)$$

where  $n$  is the motor index with the motors ordered from left to right and  $j$  is the cyclic ratio which quantifies the metachronal-wave phase shift among the oscillators as a factor of the beat cycle  $T_c$ .

The metachronal wave form is set to match the wave that spontaneously emerged during the closed loop experiment which is reported in chapter 4 in detail. The oscillatory profile of the motors here is the same as the original oscillation profile after the emergence of the metachronal wave in experiment (i.e., the same phase-relationships reported in Fig. 4.6 after 15 cycles). The only difference is that the coordinated oscillations of the motors here are imposed by the controller and not left to emerge spontaneously due to hydrodynamic interactions. The reason is that when the PIV measurement is running, the laser light represents an optical obstruction to the vision-based control loop of the spontaneous experiment, that is based on the real-time tracking of the five tips as single white dots in the image. Therefore, we imposed the metachronal-wave oscillation pattern by the external control of the five motor trajectories.

The control algorithm is implemented in an NI cRio-9074 control unit (National

Instruments, Austin, USA) using the LabVIEW FPGA software suite. Fig. 5.8 shows the experimental setup which is prepared in order to perform the PIV measurements for visualizing the flow around the beating flaplets. A Phantom Miro 310/311 Ametek camera is used to record the image of the flow around the flaplets. Fluorescent tracer-particles ( $50 \mu\text{m}$  in radius) are mixed with the glycerine liquid inside the flaplets' chamber. A continuous wave argon-ion laser beam (Raypower 5000, 5 W power at  $\lambda = 532 \text{ nm}$ , Dantec Dynamics) is expanded to a light-sheet and used to illuminate the flow in the vertical (X-Y) plane along the centre of the flaplets. The light scattered by the particles is then captured and recorded in a synchronized mode, where the camera is set to capture a single frame per each beating cycle at the same phase (phase-locked imaging of the oscillators). Consequently, displaying the successive frames provides a visualization of the net cyclic transport of the particles.

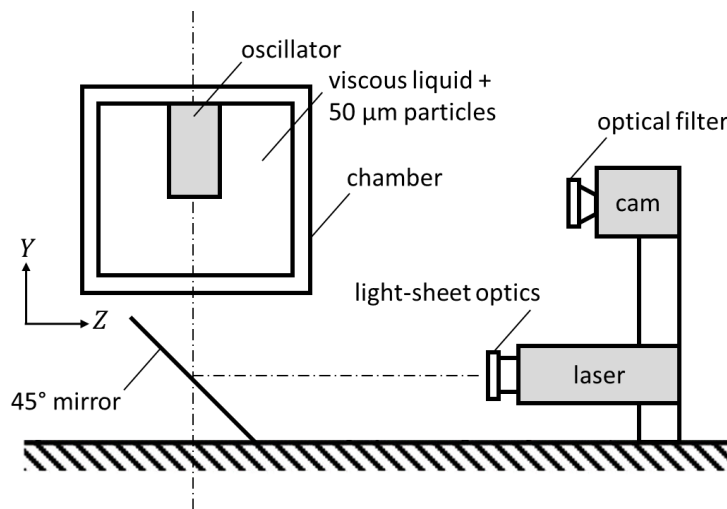


**Figure 5.8:** Schematic of the experimental setup for the Particle Image Velocimetry measurements. A vertical laser light-sheet parallel to the X–Y plane and passing through the centre of the flaplets is used along with the shown camera configuration to record the 2D flow field around the oscillators while beating in metachronal coordination.

A total of 105 particle images are recorded by the camera in a period of approximately 6 min. Fig. 5.9 shows the pathlines followed by the fluorescent particles while each oscillator is following the waveform prescribed by Eq. 5.11. The pathlines show a coherent structure of the flow below the flaplets which suggests that the flow at the vertical X–Y plane that passes through the centre of the flaplets can be considered steady in the present configuration. The figure shows smaller vortex

structures below the flaplets' surface which arise due to the fact that the flaplets are close to the bottom wall while the chamber is closed.

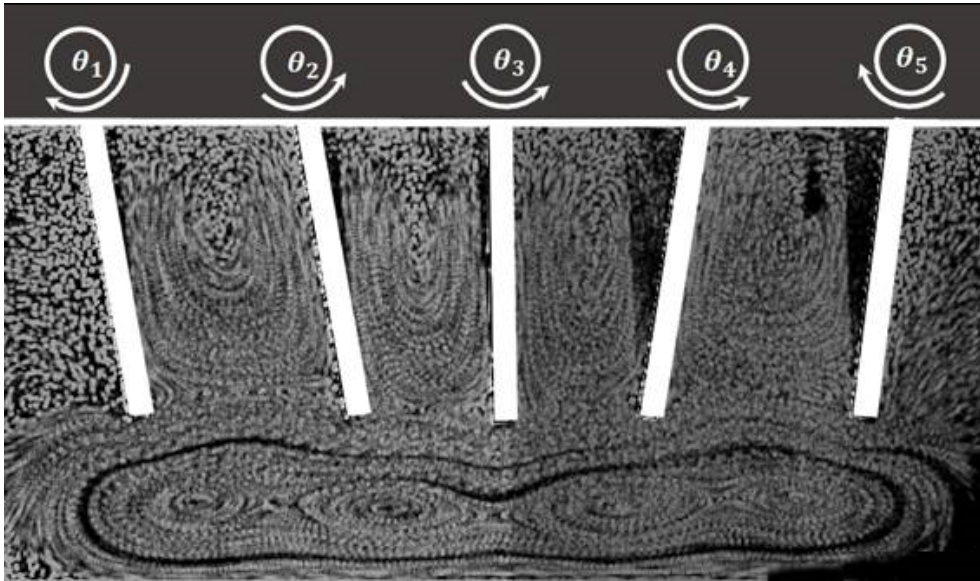


**Figure 5.9:** The pathlines of the tracer particles in the glycerine fluid as the flaplets follow the metachronal wave pattern prescribed by Eq. 5.11. The image is acquired by overlaying the frame of the flaplets with 5 phase-locked particle images that are recorded with a frame rate equal to the frequency of the flaplets' oscillatory motion. The direction of the flaplet oscillation at the instance of recording is shown by the white arrows.

In order to measure the velocity field of the flow, 2D cross-correlation of the successive frames of the particles is performed. The resulting time-averaged vector map of the velocity field of the 2D flow around the oscillators is shown in Fig. 5.10. Since the flow below the flaplets is mostly horizontal, we overlaid the vector map with the colour map of the horizontal component of the velocity  $u$ . As the graph shows, the flow near the flaplets' surface is roughly coherent and directed to the left which shows a clear net pumping effect (steady streaming) of the metachronal wave. Since the flaplets are still, this transport can be a directional measure of the net cyclic force acting on the flaplets in the X direction.

In the lower part of the flow field near the bottom wall of the chamber, the fluid is moving to the right direction; opposite to the flow at the flaplets' tips. This is a consequence of the conservation of mass in the closed chamber. Adding horizontal fluid flow in the horizontal layer at the tips in an otherwise quiescent environment must be counter-balanced by the generation of another horizontal layer of flow in the opposite direction. Between the two layers, the fluid shear is forming the vortices

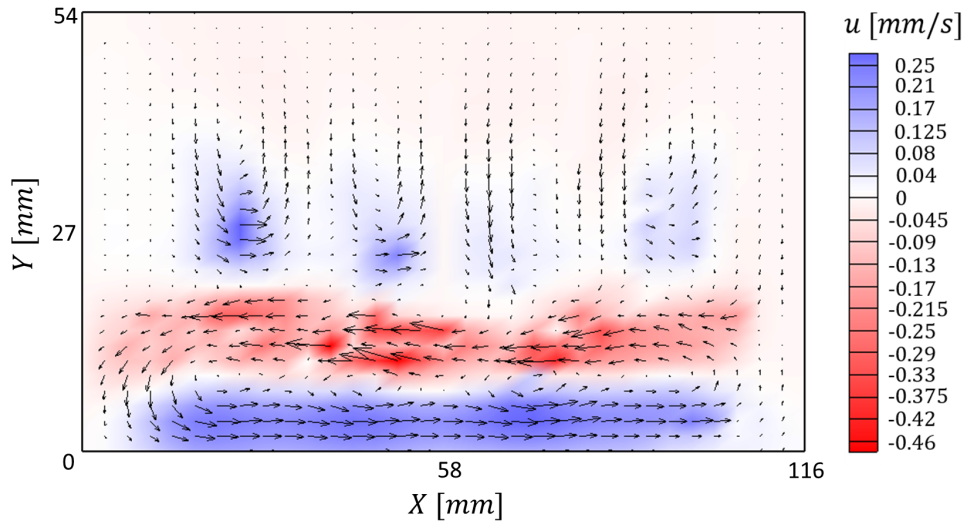


**Figure 5.10:** Time-averaged vector map of the velocity field in a vertical plane around the oscillators while beating in the metachronal coordination prescribed by Eq. 5.11. The colour map overlaid with the graph represents the magnitude and direction of  $u$  in  $mm/s$  (the  $X$  component of the velocity vectors).

known as the cat’s eye vortices that can be seen in Fig. 5.9.

## 5.7 Conclusion

For low-Reynolds propulsion, we developed a model of a flat-plate swimmer that consists of rectangular shape-symmetric flexible oscillators. Each oscillator was modelled as a cantilever beam of a rectangular cross-section, that can experience small deflections depending on its material and the surrounding viscous forces. The control of a single degree of freedom per each oscillator (the angle of rotation  $\theta$ ) was used to bound the individual oscillations to a certain amplitude. The viscous interaction forces among the oscillators and the surrounding fluid were modelled in the form of induced bending deflections at each tip. This resulted in tip trajectories that slightly deviated from the position prescribed by the driving motor angles. This deviation allowed for the cross-talk to take place throughout the system which is necessary for the emergence of spontaneous coordination. The control algorithm was based on the geometric clutch hypothesis that illustrates the geometrical limits of the oscillations in biological ciliary micro-swimmers.

Starting from random phase relationships, we could show the emergence of

both the hydrodynamic synchronization and the propulsion for this design of swimmers. The results of synchronization were compared to the produced data of a five-oscillator experiment in a viscous environment. The comparison confirmed similar coordination patterns and time scales.

The internal states of the model were then combined to represent the effective global force that acts on the swimmer due to its body-fluid interaction. The temporal evolution of the global force showed the emergence of a swimming action as the system damping goes higher. After reaching the synchronized state, the effective force still showed a remarkable increase towards its maximum value due to hardly detected variations in the oscillators' relative phases. The magnitude of the net propulsion force was found to be a linear function of the number of oscillators in the system.

Previous models of the hydrodynamic synchronization of oscillating elements used numeric simulations to render the fluid-structure interactions and the fluid dynamics. The main goal there was to reproduce and understand the process of self-synchronization due to hydrodynamic forces without worrying about the physical implementation of the simulated system nor the use of the mathematical model in engineering applications for control optimization purposes. The presented model herein bridges the gap between the simple analytical models that could not predict the resulted propulsion effect of the synchronization (e.g., concentrated-beads model of cilia (Niedermayer et al. 2008)) and the complicated high-fidelity numeric models of real cilia where the model rendering was too slow and the computations were too heavy to be used for control purposes (particle-collision-dynamics mesoscopic model of cilia (Elgeti & Gompper 2013)). The reader is referred to Table 2.3 in chapter 2 for a summary of the previously-conducted experimental and numerical studies of the hydrodynamic synchronization of cilia-like elements.

The simplicity of the proposed model's design allows for its application in different scales and environments. The flexible oscillator is a rotating flat plate attached to a rotary motor. The deflection induced at the oscillator tip, due to the surrounding viscous forces and the neighbouring oscillators, is isotropic. Several actuation mechanisms can be used to drive the rotary motion. The linearity of the model and

the observability of its internal states nominate it for real-time observer applications. Moreover, the model can be utilized for the forecasting of the settling time and the direction of the resulting forces due to a set of initial conditions.

Furthermore, the stability of the emerged synchronization in the introduced model was analysed. To begin with, the synchronization was defined as a constant phase difference between each neighbouring couple of oscillators in the beating system. This state was recognized by a constant slope (straight uni-coloured lines) in the position trajectories plots. It was observed that once the system formed this coordinated pattern, partially or globally, it kept this state from thereon. However, after analysing the emerged swimming force, we found that it still tended to increase up to its maximum value even after the first synchronization lines appeared. Accordingly, we applied the Lyapunov stability criterion on the resulted swimming forces. The long-term study showed that the system is Lyapunov stable as the value of the induced force, starting from any position close to its rest position, remained close enough to that steady-state value for the rest of the study period.

In the end, we experimentally measured the 2D velocity field of the flow around the oscillators while beating in metachronal coordination ( $j \simeq 0.2$ ) using Particle Image Velocimetry. The results showed a uni-directional steady-streaming transport of the fluid at the surface of the oscillators which can be translated into an effective propulsion force if the oscillators were attached to a body that is free to move.

## 5.8 Appendix A

### Derivation of the mathematical model

At very low Reynolds numbers  $Re \ll 1$ , , analytical expressions that describe the motion of slender bodies in Stokes flow can be used to mathematically represent interacting oscillatory systems. The reader is referred to the study here (Koenis & Lauga 2016) which examines the hydrodynamic behaviour of a slender ribbon in the Stokes flow, and the study presented in (Barta 2011) which investigates the unsteady Stokes flow around oscillatory slender bodies. The analysis performed there can be of interest in modelling the hydrodynamic interaction among oscillating elements in that Reynolds regime. On the other hand, at a Reynolds number close to unity, the effect of inertial forces cannot be completely neglected. Therefore the Stokes flow expressions are less relevant in our present study where  $Re \in [0.1, 1]$ .

The model described herein is derived on the basis of a dynamic system of which the steady-state variables are identified from theory and the experiments. This model is then rendered in Matlab Simulink to simulate the time-varying behaviour of the system under given initial conditions (angle  $\theta$  at time  $t = 0$  ). The model assumes a linear superposition of the bending contributions (self-oscillations and viscous coupling) and a first order response for their causing viscous forces. The dynamic behaviour of each oscillator is modelled as a second order response of a one-sided clamped Euler–Bernoulli beam. The different contributions to the mathematical model are given below.

### Steady-state modelling

The steady-state of the cantilever beam is represented by the total deflection of the tip  $\gamma(l)$ . Fig. 5.11 shows the model beam and its curvature parameters in response to an applied load. The radius of curvature of the deflected beam is inversely proportional to the bending moment  $M$  applied on it (Bansal 2010). By relating the beam deflection to the radius of curvature, we end up with the differential

equation of static beam deflection (Eq. 5.12).

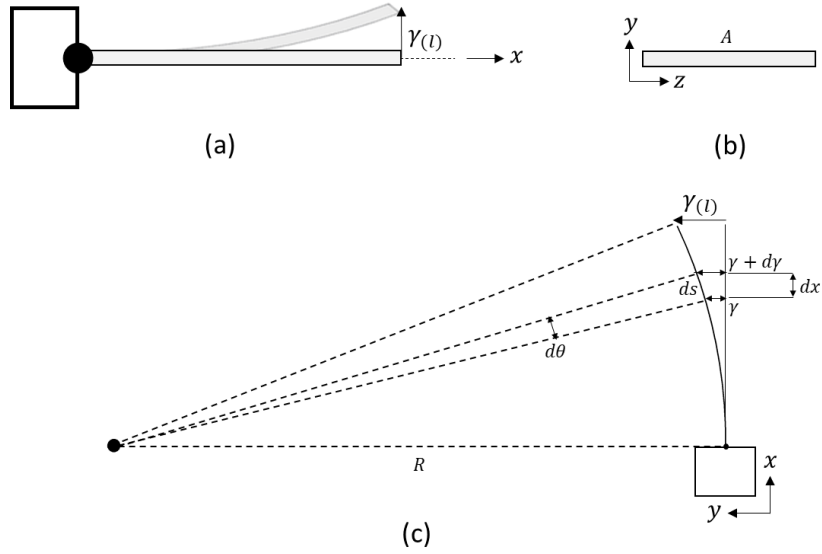


**Figure 5.11:** (a,b) Schematic view of the oscillator model as a simple beam (c) the curvature of deflection and strain parameters in the  $x$ - $y$  plane. The deflection of the oscillator is magnified in the figures for better visibility. The actual deflection does not exceed 5% of the total length. The coordinate system  $(x,y,z)$  introduced here is attached to the oscillator and inherits its orientation while the global coordinate system  $(X,Y,Z)$  is presented in Fig. 5.8.

$$\frac{d^2\gamma(t \rightarrow \infty)}{dx^2} = \frac{M(x)}{EI}, \quad \frac{d^2M}{dx^2} = \frac{dH_s}{dx} = q(x) \quad (5.12)$$

where  $\gamma(t \rightarrow \infty)$  is the steady-state deflection,  $EI$  is the flexural rigidity of the oscillator,  $H_s$  is the shear load and  $q(x)$  is the distributed load per unit length acting normal to the  $x$ - $z$  face of the flaplet. Eq. 5.12 can be solved to find an expression of the steady-state deflection of the beam's tip for a given load profile. The latter is composed of two contributions, first the load due to the drag-forces acting on the flap while rotating in the viscous liquid and secondly the effect of the neighbouring oscillators on the pressure and velocity due to viscous coupling. Given that the beam differential equation 5.12 is linear, the principle of superposition holds. It means that the steady-state total deflection of a beam can be represented as the summation of the individual deflection amounts of multiple decoupled forces. Eq. 5.13 describes the total steady-state deflection of a flaplet,  $\gamma$  as the sum of  $\gamma_o^*$

due to its own rotation in the viscous medium and  $\gamma_{r,l}^*$  due to its interaction with the right and left neighbouring oscillators.

$$\gamma^*(t \rightarrow \infty) = \gamma_o^*(t \rightarrow \infty) + \sum_{i \in \{l,r\}} \gamma_i^*(t \rightarrow \infty) \quad (5.13)$$

## Force contribution due to rotation in a still fluid

Considering the case when the flaplet is freely rotating inside the glycerine liquid. Note that the background fluid in this case is considered still, therefore  $v_r = \omega x$  when the flaplet is rotating with an angular speed of  $\omega$ . The load profile on the oscillator at  $Re \in [0.1, 1]$  can be derived from the drag coefficient of a flat rectangular plate, which is experimentally investigated in (Jones 1957) for  $Re < 2$  and found to be inversely proportional to the Reynolds number, Eq. 5.14 (Jones 1957):

$$C_d = \frac{\kappa}{Re} = \frac{\kappa\mu}{\rho v_r l} \rightarrow q(x) = \frac{1}{2} \rho w C_d v_r^2 \quad (5.14)$$

$$q(x) = -R_{\perp} v_r$$

where  $\rho$  is the fluid density and  $v_r$  is the velocity of the body relative to the background. Similar to the resistance definition in Stokes flow, we combine the factors leading the relative velocity in Eq. 5.14 as the resistance drag coefficient  $-R_{\perp}$  in the direction normal to the surface and use it in the following analysis (the negative sign indicates that the direction of the drag force is opposite to the direction of the local relative speed). Eq 5.14 suggests that the load  $q(x)$  acting on the rotating plate at this regime is directly proportional to its speed  $v_r = \omega x$  and therefore varies linearly along the flap  $q(x) \propto x$ .

In order to validate this assumption and to show that the load is approximately constant along the span a CFD numerical model of the flaplet was generated inside the ANSYS Workbench multi-physics platform. The Finite Volume Fluent Solver was used to solve the Navier–Stokes equations and capture the pressure field on the flaplet while rotating at a Reynolds number of  $Re \simeq 0.2$ . Fig. 5.12 shows the CFD results of the pressure field on the x–z face of the flaplet while rotating in the

glycerine fluid. The dimensionless notations,  $p^*$  and  $x^*$  are used where  $p^* = p/\rho(\omega l)^2$  and  $x^* = x/A$ . The figure shows a linear fit that fairly describes the load distribution along the flaplet's length.

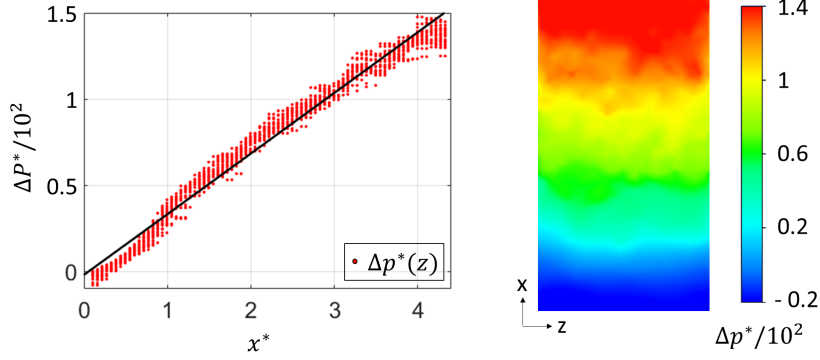


**Figure 5.12:** CFD model results of the normalized pressure difference between the x-z faces of a flaplet that rotates inside the viscous medium at a Reynold number of  $Re \simeq 0.2$ .

Finally, the solution to Eq. 5.12 with the boundary conditions  $H_s(0) = M(0) = \dot{\gamma}(0) = \gamma(0) = 0$  provides the magnitude of deflection at a distance  $x$  from the flaplet's root in the direction opposite to the local velocity at this point:

$$\begin{aligned}
 q(x) &= -R_{\perp} v_r = -R_{\perp} \omega x \\
 \gamma_o(x, t \rightarrow \infty) &= \frac{R_{\perp}}{5! EI} \omega x^5 \\
 \gamma_o^*(x, t \rightarrow \infty) &= -C \omega^* x^5, \quad C = \frac{\omega_0}{A} \frac{R_{\perp}}{5! EI}
 \end{aligned} \tag{5.15}$$

In order to evaluate the deflection magnitude for a given  $\omega$ , the value of  $C$  is experimentally identified. Therefore, we record the tip deflection of a flaplet while rotating in glycerine with different speeds. Fig. 5.13 shows the relation between the normalized deflection at the tip and the different angular speeds of the flaplet. The linear fitting line provides the missing value given in Eq. 5.16. We only consider the deflection at the tip;  $x = l$  in our model. Therefore, we will represent the deflection as a function of time only;  $\gamma^*(l, t) = \gamma^*(t)$ .

$$\gamma_o^*(t \rightarrow \infty) = -0.0145 \omega^*, \quad C = 1.4 \times 10^5 \tag{5.16}$$

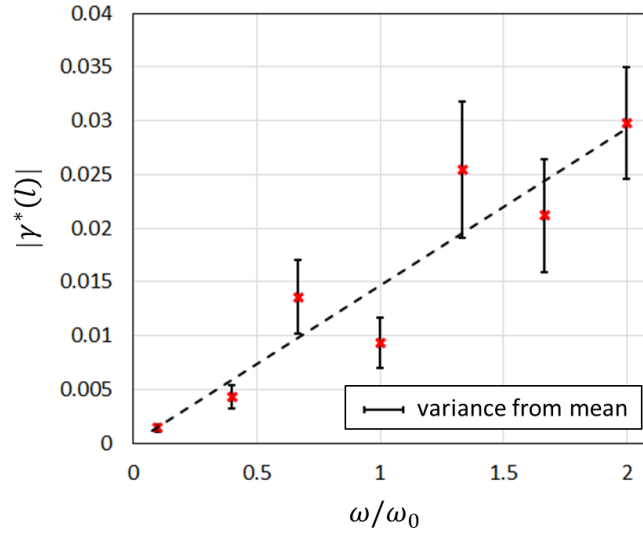


**Figure 5.13:** Normalized deflection magnitude of a rotating flaplet in glycerine as a function of its normalized angular speed. The bar lines indicates the deviation of the dynamic deflection from its mean during a single beat cycle.

## Force contribution due to viscous interaction

The effect of viscous interaction on the flaplet's bending depends on the distance  $r$  between the tips of the neighbouring flaplets. A further experiment was performed, where we allow two neighbouring flaplets (one is rotating and the other is still;  $\Delta\omega = \omega_0$ ) to interact in the viscous fluid and we measure the deflection at the tip of the still flaplet. Fig. 5.14 shows a plot of the normalized deflection of the tip,  $\gamma^*(l)$ , as a function of  $r^*$ . For simplification, we fit a linear function to the part of the curve where  $\gamma^*(l) > 0.02$ . We can then define the distance  $\delta_r^* \simeq 1$  beyond which the interaction is considered constant;  $\gamma^*(l) = 0.013$  as highlighted on the plot. For the given configuration in the experiment,  $\delta_r$  is the boundary limit beyond which the effect of an oscillator rotation on its neighbour deflection at the tip is almost constant and fairly negligible.

The variation of the phase relationships among the flaplets until they reach coordination is dependent on the deflection values at their tips. Fig. 5.14 shows that the deflection of a still flaplet due to the rotation of its neighbour can reach up to 10% of the oscillation amplitude. This observation highlights the significance of the viscous interaction among the flaplets in the emergence of their self-assembly.

According to the experimental result shown in Fig. 5.14, we can approximate

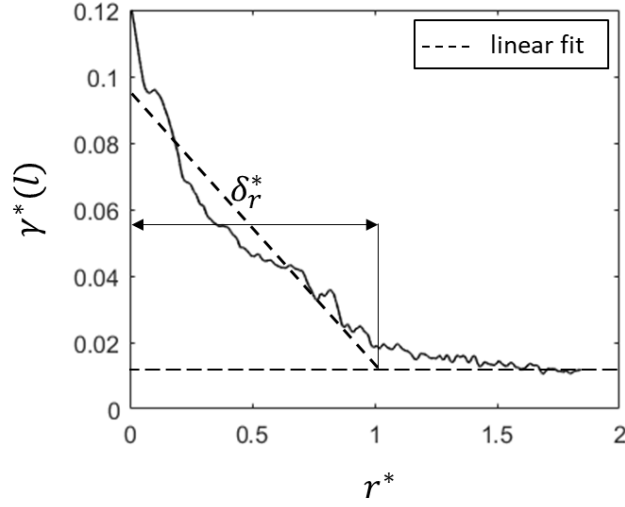


**Figure 5.14:** Normalized deflection of a still flaplet due to the rotation of its neighbour as a function of the normalized distance between their tips. The ramp dashed line is a linear fit for the deflection values that are greater than 2% of the oscillation amplitude. From there the deflection is considered constant.

the bending interaction of a flaplet due to a rotating neighbour with the following definition:

$$\gamma_{r,l}^*(t \rightarrow \infty) = \begin{cases} 0.013d_{r,l} & r_{r,l}^* > 1 \\ d_{r,l}(-0.082r_{r,l}^* + 0.095) & r_{r,l}^* \leq 1 \end{cases}$$

$$d_{r,l} = \frac{\Delta\omega}{\omega_0} \quad (5.17)$$

in which  $d_{r,l}$  is a dimensionless factor that accounts for the direction of the rotational speed of the right/left neighbour,  $\omega_{r,l}$ , relative to the flaplet's self-rotation,  $\omega$ . This linear approximation for the two different contributions allows for the use of the principle of superposition.

## Dynamics modelling

The system dynamics can be divided into two time-invariant dynamic systems that describe the oscillator as well as its surrounding viscous medium. In this section the two models are deduced and identified using results from the experiments.

## Fluid dynamics

The transient behaviour of the fluidic forces that cause the bending is represented by a first-order system as the system is investigated at a low Re-number. This considers the time-constant of the build-up of the deflection forces induced by the rotation of the flaplet in the viscous medium and its interaction with the neighbouring oscillators. This leads to a first-order response of the deflection contributions:

$$\gamma^*(t) = \gamma^*(t \rightarrow \infty)(1 - e^{-\frac{t}{T}}) \quad (5.18)$$

The time constant,  $T$ , is tuned to best match the experimental response described in section 5.4.2 and is found to be at least one order of magnitude lower than the characteristic cycle period.

## Oscillator dynamics

The proposed cantilever beam model, shown in Fig. 5.15, is a second order dynamic system which is analogous to a mass-spring-damper system. This representation is well established and can be derived from the Euler–Bernoulli beam theory and used as a reduced order model of the oscillator (Rao 2007, Banks & Inman 1991). The final response of the deflection of the oscillator tip can be represented by:

$$\gamma_t^*(t) = \gamma^* \left[ 1 - \left( \frac{\lambda_2}{\lambda_2 - \lambda_1} e^{\lambda_1 t} + \frac{\lambda_1}{\lambda_1 - \lambda_2} e^{\lambda_2 t} \right) \right] \quad (5.19)$$

$$\lambda_1, \lambda_2 = -\zeta \omega_n \pm \omega_n \sqrt{\zeta^2 - 1}$$

In order to identify the value of  $\omega_n$  at low Reynolds numbers, we refer to the first mode of vibration of the Euler-Bernoulli beam model (Han et al. 1999).

$$\omega_n = 3.5161 \sqrt{\frac{EI}{m_t l^3}}$$

in which  $m_t$  is the total inertia of the oscillating mechanism.

The oscillator while moving is forcing a part of the liquid mass to move along with it. This leads to an increase in the total effective inertia and consequently a

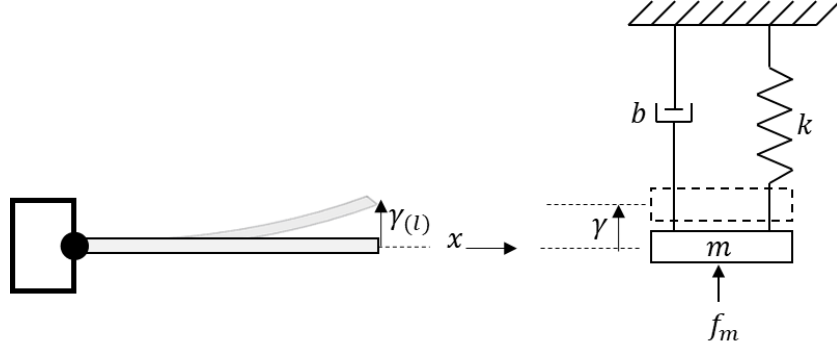


**Figure 5.15:** The model of the flexible flat-plate oscillator as a mass–spring–damper system.

lower output frequency (Vančura et al. 2008). The above relation becomes:

$$\omega_n = \frac{3.5161}{l^2} \sqrt{\frac{EI}{\rho_o b h + \mu_a}} \quad (5.20)$$

where  $\rho_o$  is the oscillator density,  $b$  is its width,  $h$  is its thickness and  $\mu_a$  is the added mass per unit length.

According to (Korayem et al. 2011, Greenspon 1961), the added mass density of a rectangular plate in the presence of the viscous fluid can be approximated by:

$$\mu_a = 0.6\rho_f l^{0.5} b^{1.5}$$

where  $\rho_f$  is the liquid density. By substituting the value of  $\mu_a$  in equation 5.20, we get  $\omega_n = 32.3$ .

We then experimentally investigate the response of the flexible oscillator due to an initial imposed small deflection at its tip,  $\gamma(0) = 0.05l$ . Using a high-speed camera, we could capture the response of the oscillator in the viscous fluid as shown in Fig. 5.16. We can then estimate the period that the tip takes to reach within a range of 5% of  $\gamma(0)$  around its position of rest. This period represents the settling time of the damped system,  $T_{95\%} = 0.026T_c$ , where  $T_c$  is the cycle period.

The damping ratio  $\zeta$  is then tuned to achieve the same settling time in the proposed second order model. The identified value of  $\zeta$  is then found to be  $\zeta = 1.04$ .

Accordingly, the values of  $k$ ,  $m$  and  $b$  can be calculated assuming that the spring

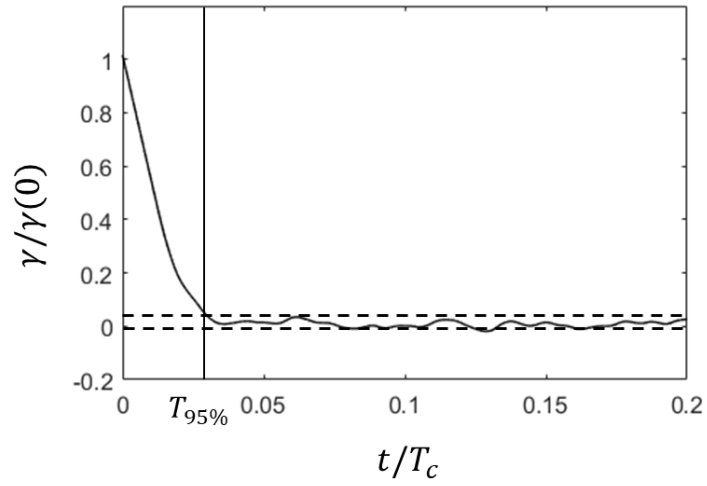


**Figure 5.16:** Measured response of the oscillator's tip in the glycerine liquid due to an initial imposed deflection;  $\gamma(0)$

stiffness  $k = 3EI/L^3$  (Bellon 2008)

$$2\zeta\omega_n = \frac{b}{m_{eff}}, \quad \omega_n = \sqrt{\frac{k}{m_{eff}}}$$

$$m_{eff} = 3.4 * 10^{-3}, \quad b = 0.22, \quad k = 3.54$$

$$f_m = k\gamma$$

## 5.9 Critical analysis

### 5.9.1 Overview and study contributions

The emergence of metachronal waves in 2D flexible flaps beating in a chamber filled with a high viscous liquid is experimentally demonstrated in Chapter 4. In this study, a simple mathematical model of the system that reproduces the phenomena is introduced. The model, that is identified from a set of experiments and from theory, assumes a quasi-linear dynamic model of the rotating flaplets and their viscous coupling in the viscous liquid. At the end of the study, a flow measurement was performed in order to study the pumping performance of the swimmer-model while in metachronal coordination using Particle-Image-Velocimetry. The contributions of the present work can be summarized in the following points: (i) modelling of a row of oscillating cilia-like flaplets in a viscous environment; (ii) presentation of the spontaneous emergence of metachronal coordination and studying its long-term stability; (iii) investigation of the net forces build-up on the flaplets during the self-synchronization; (iv) study of the effective propulsion that results from the emerged metachronal coordination.

### 5.9.2 Exploratory discussion and future work

#### 5.9.2.1 Considerations of the flaplets model in different conditions

Although, the current model is tested inside a closed chamber, a similar behaviour of the flaplets' coordination and the resulted flow is expected in case of an open environment in a real-life application. Firstly, due to the highly-viscous environment, the side walls do not have a big influence on the flaplets' bending and the resulted flow profile. As shown from the PIV results the flow converges to zero in the near region, close to the first and last flaplets, approximately 100 mm far away from the wall from each side. If the side walls were close to the flaplets (less than 20 mm away), their influence on the flaplet's bending would be noticeable and therefore the first and last flaplets would become less sensitive to the viscous-coupling effects that

lead to synchronization. Regarding the bottom wall of the chamber, it is expected that it currently has a detectable effect on the resulted fluid shear, forming the cat's eye vortices witnessed in Fig 5.9 while the flaplets are in metachronal coordination. Having the bottom wall more distant from the flaplets would increase the depth of the uni-directional flow just below the coordinated flaplets.

In nature, the forward and return strokes of cilia are asymmetric, while, in the present study, the oscillation profiles of the coordinated flaplets are in principle time-symmetric. The addition of another degree of asymmetry (e.g., different gait and speed for each stroke) is expected to enhance the propulsion performance of the system at the current Reynolds numbers, by violating the Purcell's symmetry arguments for each oscillator separately. However, that adjustment would also increase the complexity of the oscillators' actuation and/or control. For both cases, the metachronal coordination is still expected to have a significant effect on the resulted propulsion performance. Since, the present results proved that the metachronal coordination of the time-symmetric oscillators provides the system with the ability to generate effective propulsion, the same profiles introduced herein can still be used in real-world applications.

The present study is performed using a single row of the flaplets which allowed us to deal with the hydrodynamic interaction forces and the emerged metachronal coordination in a single direction (the streamwise direction – the  $X$  axis in Fig. 5.8) and with the resulted flow field in the two-dimensional space  $(X, Y)$ . The current problem can be transformed into a three-dimensional problem by using a two-dimensional array of the flaplets instead of a single row. In that case, the metachronal waves can be produced in the  $(X, Y)$  plane, giving rise to a three-dimensional flow field. Accordingly, in experiment, the metachronal waves are expected to emerge in both the  $X$  and  $Y$  directions. This assumption is based on the illustration given by (Elgeti & Gompper 2013) when the emergence of metachronal waves was studied in 2D arrays of model cilia. The resulted coordination there was not confined to a single dimension along the cilia. Instead, a two-dimensional spatial metachronal-wave pattern was formed. In our simulation, in case an array of flaplets is considered, the viscous-coupling model of the flaplet will need to be expanded in order to account

for the hydrodynamic interaction forces in the spanwise direction. These forces will arise from the coupling with the new neighbouring flaplets in that direction and will need to be identified from a 3D experiment. The expanded model would then be able to simulate the emergence of the emerged metachronal waves in two dimensions.

### **5.9.2.2 The role of flexibility in the emergence of both coordination and propulsion**

If the flaplets were rigid, the viscous forces in the given system would not influence the phase relationship among the oscillators and hence they would keep their initial phase relationships for all times. Because the clutch hypothesis is implemented into the control loop by tracking the tips' locations, the addition of flexibility allows the viscous forces to affect the tips' oscillatory motion. Their positions can differ from those of the rigid ones, and hence the phase relationships among the oscillators can vary from cycle to cycle. Herein, we observe the transition of the system gradually to a metachronal wave. If the flexibility were too large (considering the applied viscous forces), there would be no enough momentum added to the surrounding fluid and the system could not generate an effective propulsion. The question of optimum flexibility is not yet discussed in the present study.

### **5.9.2.3 Reynolds-number considerations**

We believe that the rise of metachronal waves is not confined to a finite value of Reynolds number ( $Re$ ). The cilia on the surface of Ctenophora witness coordination while beating at relatively-high Reynolds numbers, ranged from 10 to 300 (Matsumoto 1991). The upper limit of  $Re$  for self-coordination is not studied here and is left open for future studies with liquids of varying viscosities. We also expect a similar behaviour of coordination in the Stokes regime which had been demonstrated for other system types and shapes in previous studies. In the presented simulation, we could not validate the proposed model and its physical assumptions outside of the Reynolds range where we measured the deflection experimentally.

At slightly-higher Reynolds numbers, compared to the present study, the inertial effects will come into play. It is expected that the system parameters particularly

the system's time constants will vary accordingly. Since, the model presented in this study does not account for inertial effects, all parameters would have to be identified from a different set of experiments than the one presented here. As the Reynolds number goes more higher, the viscous coupling among the flaplets will partially deteriorate in the presence of high inertial forces and, accordingly, the superposition and time-independence assumption adopted in the present study might not be valid.

#### **5.9.2.4 Future work of the model as a state-observer for controller design optimization**

Usually, the experimental measurements of some of the system's internal states is not possible. Being able to track these states provides the opportunity to design a more efficient controller (pretty much like how tracking the speed and torque of an electric motor would allow for a better control of its position since the input variables, i.e. voltage and current, influence the output position through these internal states).

By the word "observation", we mean computational tracking rather than experimental measurement. There are observation techniques (e.g. a Kalman Filter) that can be able to deduce the values of the internal states in real-time while the physical system is running given only the measured output of the system. These techniques require a fast computed digital model of the system (unlike finite element models) which need to run faster than the physical system in order to be able to track the values in real-time. The proposed model being linear and fast-computed can serve as a real-time observer in a micro-swimmer control application.

#### **5.9.3 Relation between the number of flaplets and the time required for self-synchronization**

One of the advantages of the proposed model is that it allows for studying the emergence of coordination for large number of flaplets. It is plausible to assume that a correlation exists between the number of flaplets and the period required for the coordination to rise. To verify this assumption, the model of 32 oscillators was rendered starting from random initial positions of the oscillators and ran the

control loop until the system reached full and stable metachronal synchronization, and then examined the periods required for each oscillator to reach synchronization. The oscillator is marked as “joined coordination” once it reaches within 2% around its steady-state phase relationship with its adjacent neighbour. Fig. 5.17 shows the results of this investigation as a cumulative histogram plot of the number of oscillators that reach coordination versus the time in beat cycles.

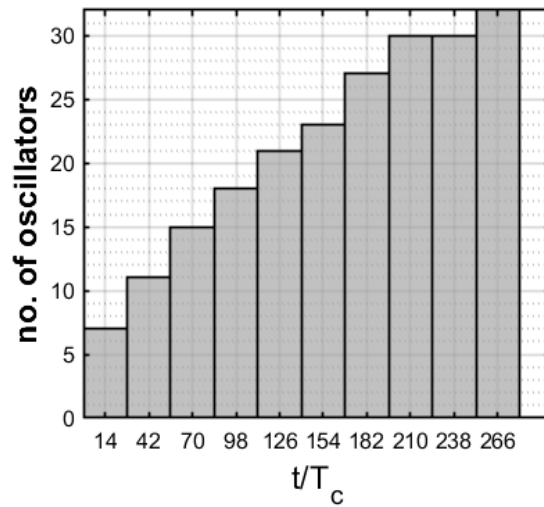


**Figure 5.17:** Number of oscillators to reach synchronization during the build-up stage of full metachronal coordination of 32 oscillators. Each oscillator is considered to join coordination once it reaches within 2% around its steady-state phase relationship with its adjacent neighbour.

The plot shows that the time required for the first 7 oscillators to reach coordination is relatively short (approximately 14 cycles). From there on, a steady increase of the number of oscillators that join coordination is observed with time. The average period required for a new oscillator to join coordination is approximately 7 cycles.

#### 5.9.4 Flow visualization results due to different coordination phase-shifts among the flaplets

As demonstrated in section 2.6, the row of five oscillating flaplets could produce net transport of the fluid at the surface when forming a coordinated beating pattern with a phase shift of 20% of a cycle between the neighbouring flaplets ( $j = 0.2$  in Eq. 5.11). Herein, I investigate the resulted flow field due changing the parame-

ter  $j$  (the phase shift) of the coordinated beating flaplets. Firstly, I refer to the illustration presented in the previous chapter (section 4.5.3) about the application of the Purcell's symmetry arguments to the physical system as a unit (not to the individual oscillators). We concluded that as long as the system do not form an in-phase or out-of-phase beating pattern, the running metachronal wave will have a certain direction that is not time-reversible which suggests that net propulsion could occur. After performing multiple PIV measurements with different values of the parameter  $j$ , it was found out that a net transport of the fluid is achieved for coordination patterns with  $0 < |j| < 0.5$ . These findings are demonstrated in the following three plots in Fig. 5.18; (top) the transport reported in section 2.6 when  $j = 0.2$ ; (middle) opposite-direction net transport of the fluid when  $j = -0.4$ ; (bottom) zero net transport at the surface when  $j = 0.5$  (out-of-phase coordination). The speed scale of the three plots is unified for a clear comparison.

The parameter  $j$  controls the direction of the running metachronal wave. When positive, it indicates that the wave is running from left to right. An example of that case is shown in Figure 5.9. The left-most flaplet (with angular position  $\theta_1$ ) is the leading flaplet in that figure. When the parameter  $j$  is negative, it indicates that the wave is running from right to left, and that the right-most flaplet is the leading flaplet. Depending on the direction of the resulted flow, the metachronal wave herein was found to be antiplectic. It means that the direction of the resulted propulsion is always opposite to the direction of the running metachronal wave. Accordingly, as demonstrated in the figure, the direction of the resulted transport at the flaplets' surface is to the left when the parameter  $j$  is positive and to the right when it is negative. The case of antiplectic metachronism is popular in biological ciliated systems (Knight-Jones 1954). It was demonstrated that this type of metachronal waves is optimal for generating efficient transport in epithelial cilia (Chateau et al. 2019). A symplectic metachronal wave cannot be generated by the current setup. This is because the individual oscillators do not feature a default power stroke on their own, as their beat profiles are time-symmetric. Since the propulsion here is a consequence of the metachronal coordination alone, its direction cannot be reversed without reversing the direction of the running metachronal wave.

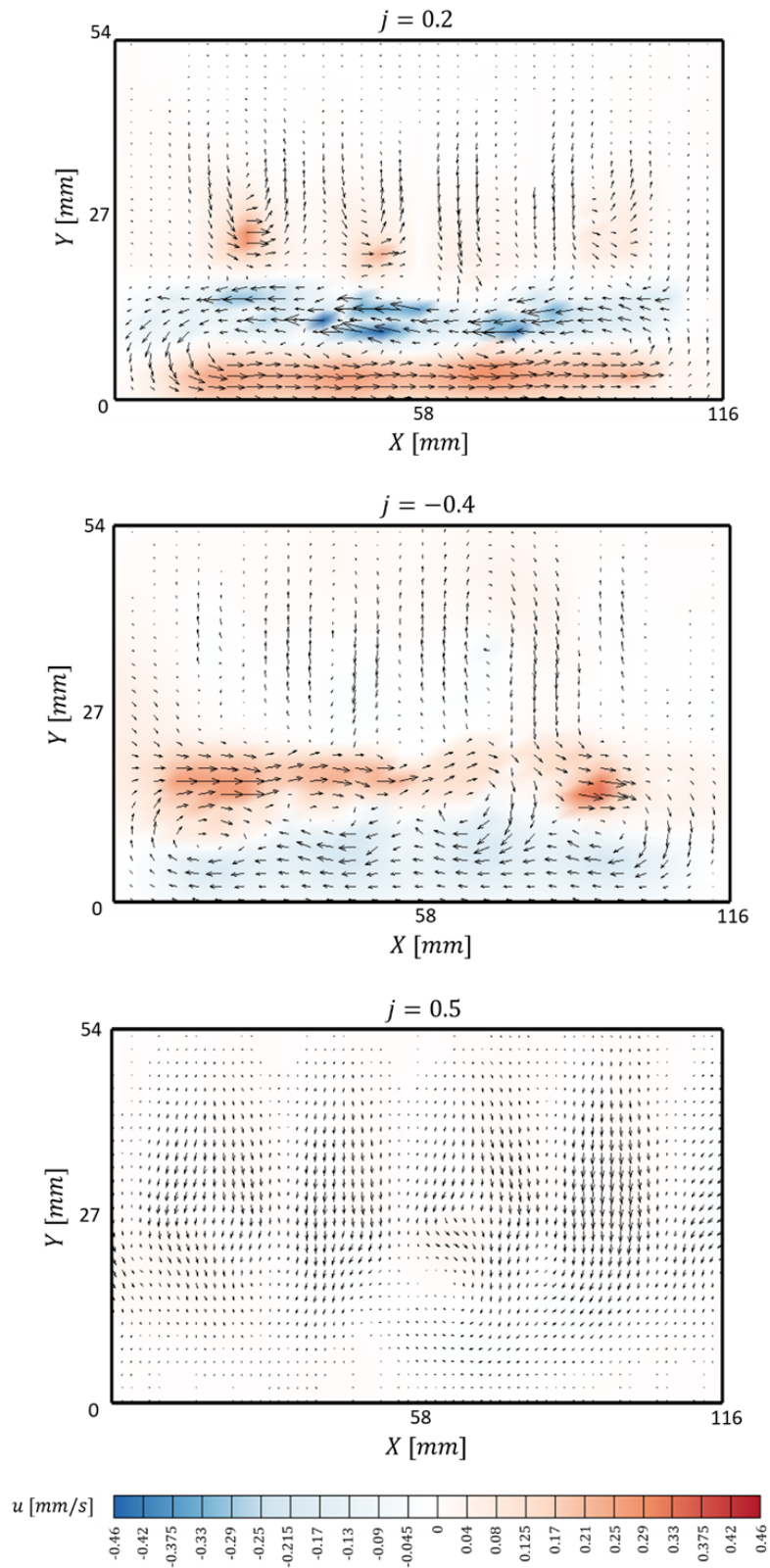


**Figure 5.18:** Flow visualization results of the coordinated oscillators for different phase relationships.

# Chapter 6

## Conclusions

Using engineering tools to mimic the different processes and behaviours witnessed in nature has helped humanity to achieve consequential advancements in multiple fields. The research presented in this PhD thesis has focused on the understanding and employment of two behaviours observed in organisms possessing superficial hair-like structures in fluidic environments. In this chapter, the thesis key results are summarized, highlighting the future work that can build on the present findings.

In the first study, a novel methodology of underwater sensing was developed and tested using deep-learning models. The disturbance signature left behind a wake-generating object in water could be sensed and interpreted as accurate locations of the object. The idea was inspired from the ability of the seal to track preys in water, even blindfolded, by sensing the vibrations of its facial hairs. The seal's brain is able to form a hydrodynamic image of its surroundings by processing these vibrations. Similarly, the presented neural-network models herein could translate the vibrations of an array of artificial whiskers into the two-dimensional position of the disturbance source underwater with a high degree of accuracy.

The implementation of the whisker-array transducer presented here is affordable, lifelike and has a minimum impact on the underwater environment. It can help overcome the well-known challenges of sonar and vision-based sensors. It can also be improved in order to be used for real-time tracking tasks in autonomous and remotely-controlled underwater vehicles.

The introduced measurement setup used a high-speed camera to track the de-

flexion responses of the artificial whiskers made from optical fibers. Future work has already been planned to investigate alternative ways of sensing the vibrations of the artificial whiskers instead of the current vision-based system. Strain gauges or Fiber-Bragg gratings will be considered to replace the camera in the current setup and, therefore, the full embedded system will be ready for testing as a robotic solution. Another project has been also planned to implement the whisker-array sensor in a real-time tracking task. The new measurement system should read the vibration signals of the different whiskers and send them to the controller, The learning models implemented inside the controller will then predict the required orientation of the robot in order to directly face the disturbance source, then the robot will be actuated accordingly with the relative angle of rotation.

The study also introduced the use of computational-intelligence tools for interpreting natural behaviours and fluid-structure-interaction problems. The physics-based modelling of fluid-mechanics problems is sometimes complicated or not possible. Numeric simulations, on the other hand, usually consume a big deal of time and computational resources. Using machine learning to simulate the process or capability being researched not only can facilitate its understanding by interpreting the trained learning models but also allows for its direct deployment in relevant engineered applications.

The second study presented an experiment and a model of the emergence of metachronal self-coordination in a row of flexible oscillators similar to that witnessed in biological ciliary systems. The conditions that lead to hydrodynamic coordination of the oscillators were tested and the evolution of the resulted coordination was closely examined. The hydrodynamic cross-talk among the oscillators (in form of pending deflections at their tips due to the viscous-coupling forces) represented the key factor in the system transformation towards its coordinated state. The study used material flexibility and position feedback control of the oscillator tips to implement the geometric clutch hypothesis that features the cilium beat. This implementation is not confined to the present geometry and may be replicated in future research using different materials and shapes.

The flow field around the resulted coordination-state of the oscillators was in-

investigated using particle-image-velocimetry. The system of coordinated oscillators could generate surface transport of the surrounding medium which can be translated to a net swimming force in case that the system was free to move.

The study proved that flat-plate oscillators with time-symmetric beating profiles can spontaneously synchronize their oscillations and generate propulsion at low-Reynolds environments. The presented artificial-cilia model is simple and easy to control using ordinary rotary actuators, and can generate propulsion at low-Reynolds regimes. In future work, it can be tested in micro-swimmer applications or as a propulsion device in viscous environments. The introduced mathematical state-space model of the oscillators can facilitate the controller-design process in future applications by using state-observation techniques, that would allow to optimize the resulted propulsion performance.

## Bibliography

- Abbott, J. J., Peyer, K. E., Lagomarsino, M. C., Zhang, L., Dong, L., Kaliakatsos, I. K. & Nelson, B. J. (2009), ‘How should microrobots swim?’, *The international journal of Robotics Research* **28**(11-12), 1434–1447.
- Akyildiz, I. F., Pompili, D. & Melodia, T. (2004), ‘Challenges for efficient communication in underwater acoustic sensor networks’, *ACM Sigbed Review* **1**(2), 3–8.
- Allan, R. A., Elgar, M. A. & Capon, R. J. (1996), ‘Exploitation of an ant chemical alarm signal by the zodariid spider *habronestes bradleyi walckenaer*’, *Proceedings of the Royal Society of London. Series B: Biological Sciences* **263**(1366), 69–73.
- Anderson, J. A. (1995), *An introduction to neural networks*, MIT press.
- Avron, J., Kenneth, O. & Oaknin, D. (2005), ‘Pushmepullyou: an efficient micro-swimmer’, *New Journal of Physics* **7**(1), 234.
- Ball, P. (2013), ‘Material witness: When water doesn’t wet’, *Nature materials* **12**(4), 289.
- Banks, H. T. & Inman, D. (1991), ‘On damping mechanisms in beams’, *Journal of applied mechanics* **58**(3), 716–723.
- Bansal, R. (2010), *A textbook of strength of materials*, Laxmi Publications.
- Barta, E. (2011), ‘Motion of slender bodies in unsteady stokes flow’, *Journal of fluid mechanics* **688**, 66–87.
- Batchelor, C. K. & Batchelor, G. (2000), *An introduction to fluid dynamics*, Cambridge university press.

- Battiti, R. (1992), ‘First-and second-order methods for learning: between steepest descent and newton’s method’, *Neural computation* **4**(2), 141–166.
- Becker, L. E., Koehler, S. A. & Stone, H. A. (2003), ‘On self-propulsion of micro-machines at low reynolds number: Purcell’s three-link swimmer’, *Journal of fluid mechanics* **490**, 15–35.
- Beckers, R., Goss, S., Deneubourg, J.-L. & Pasteels, J.-M. (1989), ‘Colony size, communication and ant foraging strategy’, *Psyche: A Journal of Entomology* **96**(3-4), 239–256.
- Beem, H., Hildner, M. & Triantafyllou, M. (2012), Characterization of a harbor seal whisker-inspired flow sensor, in ‘2012 Oceans’, IEEE, pp. 1–4.
- Beem, H. R. & Triantafyllou, M. S. (2015), ‘Wake-induced ‘slaloming’ response explains exquisite sensitivity of seal whisker-like sensors’, *Journal of Fluid Mechanics* **783**, 306–322.
- Bellon, L. (2008), ‘Thermal noise of microcantilevers in viscous fluids’, *Journal of Applied Physics* **104**(10), 104906.
- Bennett, R. R. & Golestanian, R. (2013), ‘Emergent run-and-tumble behavior in a simple model of chlamydomonas with intrinsic noise’, *Physical review letters* **110**(14), 148102.
- Blake, J. R. & Sleigh, M. A. (1974), ‘Mechanics of ciliary locomotion’, *Biological Reviews* **49**(1), 85–125.
- Blake, J., Vann, P. & Winet, H. (1983), ‘A model of ovum transport’, *Journal of theoretical biology* **102**(1), 145–166.
- Bottier, M., Thomas, K. A., Dutcher, S. K. & Bayly, P. V. (2019), ‘How does cilium length affect beating?’, *Biophysical journal* **116**(7), 1292–1304.
- Brokaw, C. (1975), ‘Effects of viscosity and atp concentration on the movement of re-activated sea-urchin sperm flagella’, *Journal of Experimental Biology* **62**(3), 701–719.

- Brokaw, C. J. (1972), ‘Computer simulation of flagellar movement: I. demonstration of stable bend propagation and bend initiation by the sliding filament model’, *Biophysical Journal* **12**(5), 564–586.
- Brücker, C., Schnakenberg, U., Rockenbach, A., Mikulich, V. et al. (2017), ‘Effect of cilia orientation in metachronal transport of microparticles’, *World Journal of Mechanics* **7**(01), 1.
- Brumley, D. R., Wan, K. Y., Polin, M. & Goldstein, R. E. (2014), ‘Flagellar synchronization through direct hydrodynamic interactions’, *Elife* **3**, e02750.
- Bruot, N. & Cicuti, P. (2016), ‘Realizing the physics of motile cilia synchronization with driven colloids’, *Annual Review of Condensed Matter Physics* **7**, 323–348.
- Campanella, C. E., Cuccovillo, A., Campanella, C., Yurt, A. & Passaro, V. (2018), ‘Fibre bragg grating based strain sensors: review of technology and applications’, *Sensors* **18**(9), 3115.
- Chakrabarti, B. & Saintillan, D. (2019), ‘Hydrodynamic synchronization of spontaneously beating filaments’, *Physical Review Letters* **123**(20), 208101.
- Chateau, S., Favier, J., Poncet, S. & d’Ortona, U. (2019), ‘Why antiplectic metachronal cilia waves are optimal to transport bronchial mucus’, *Physical Review E* **100**(4), 042405.
- Cho, S. et al. (2014), ‘Mini and micro propulsion for medical swimmers’, *Micromachines* **5**(1), 97–113.
- Cox, R. (1970), ‘The motion of long slender bodies in a viscous fluid part 1. general theory’, *Journal of Fluid mechanics* **44**(4), 791–810.
- De Langre, E. (2001), *Fluides et solides*, Editions Ecole Polytechnique.
- Dehnhardt, G., Mauck, B. & Bleckmann, H. (1998), ‘Seal whiskers detect water movements’, *Nature* **394**(6690), 235–236.
- Dehnhardt, G., Mauck, B., Hanke, W. & Bleckmann, H. (2001), ‘Hydrodynamic trail-following in harbor seals (*phoca vitulina*)’, *Science* **293**(5527), 102–104.

- Delamare, J., Sanders, R. & Krijnen, G. (2016), 3d printed biomimetic whisker-based sensor with co-planar capacitive sensing, *in* ‘2016 IEEE SENSORS’, IEEE, pp. 1–3.
- Di Leonardo, R., Búzás, A., Kelemen, L., Vizsnyiczai, G., Oroszi, L. & Ormos, P. (2012), ‘Hydrodynamic synchronization of light driven microrotors’, *Physical review letters* **109**(3), 034104.
- Dietterich, T. (1995), ‘Overfitting and undercomputing in machine learning’, *ACM computing surveys (CSUR)* **27**(3), 326–327.
- Dijkstra, M., Van Baar, J., Wiegerink, R. J., Lammerink, T. S., De Boer, J. & Krijnen, G. J. (2005), ‘Artificial sensory hairs based on the flow sensitive receptor hairs of crickets’, *Journal of micromechanics and microengineering* **15**(7), S132.
- Doering, C. R. & Gibbon, J. D. (1995), *Applied analysis of the Navier-Stokes equations*, Vol. 12, Cambridge University Press.
- Drescher, K., Goldstein, R. E. & Tuval, I. (2010), ‘Fidelity of adaptive phototaxis’, *Proceedings of the National Academy of Sciences* **107**(25), 11171–11176.
- Dreyfus, R., Baudry, J., Roper, M. L., Fermigier, M., Stone, H. A. & Bibette, J. (2005), ‘Microscopic artificial swimmers’, *Nature* **437**(7060), 862–865.
- Dreyfus, R., Baudry, J. & Stone, H. A. (2005), ‘Purcell’s “rotator”: mechanical rotation at low reynolds number’, *The European Physical Journal B-Condensed Matter and Complex Systems* **47**(1), 161–164.
- Earl, D. J., Pooley, C., Ryder, J., Bredberg, I. & Yeomans, J. (2007), ‘Modeling microscopic swimmers at low reynolds number’, *The Journal of chemical physics* **126**(6), 02B603.
- Eberhardt, W. C., Wakefield, B. F., Murphy, C. T., Casey, C., Shakhsher, Y., Calhoun, B. H. & Reichmuth, C. (2016), ‘Development of an artificial sensor for hydrodynamic detection inspired by a seal’s whisker array’, *Bioinspiration & biomimetics* **11**(5), 056011.

- Efficient 2D histogram, no toolboxes needed, MATLAB Central File Exchange. Retrieved from:* (n.d.), <https://www.mathworks.com/matlabcentral/fileexchange/45325-efficient-2d-histogram-no-toolboxes-needed>. Accessed: 02-03-2020.
- Elfring, G. J. & Lauga, E. (2009), ‘Hydrodynamic phase locking of swimming microorganisms’, *Physical review letters* **103**(8), 088101.
- Elgeti, J. & Gompper, G. (2013), ‘Emergence of metachronal waves in cilia arrays’, *Proceedings of the National Academy of Sciences* **110**(12), 4470–4475.
- Elgeti, J., Winkler, R. G. & Gompper, G. (2015), ‘Physics of microswimmers—single particle motion and collective behavior: a review’, *Reports on progress in physics* **78**(5), 056601.
- Elshalakani, M. & Brücker, C. (2018), ‘Spontaneous synchronization of beating cilia: An experimental proof using vision-based control’, *Fluids* **3**(2), 30.
- Eshel, D. & Priel, Z. (1987), ‘Characterization of metachronal wave of beating cilia on frog’s palate epithelium in tissue culture.’, *The Journal of physiology* **388**(1), 1–8.
- Evans, B., Shields, A., Carroll, R. L., Washburn, S., Falvo, M. & Superfine, R. (2007), ‘Magnetically actuated nanorod arrays as biomimetic cilia’, *Nano letters* **7**(5), 1428–1434.
- Favier, J., Li, C., Kamps, L., Revell, A., O’connor, J. & Brücker, C. (2017), ‘The pelskin project—part i: fluid–structure interaction for a row of flexible flaps: a reference study in oscillating channel flow’, *Meccanica* **52**(8), 1767–1780.
- Fulford, G. R. & Blake, J. R. (1986*a*), ‘Muco-ciliary transport in the lung’, *Journal of theoretical Biology* **121**(4), 381–402.
- Fulford, G. R. & Blake, J. R. (1986*b*), ‘Muco-ciliary transport in the lung’, *Journal of theoretical Biology* **121**(4), 381–402.
- Galdi, G. (2011), *An introduction to the mathematical theory of the Navier-Stokes equations: Steady-state problems*, Springer Science & Business Media.

- Gao, W., Feng, X., Pei, A., Kane, C. R., Tam, R., Hennessy, C. & Wang, J. (2014), ‘Bioinspired helical microswimmers based on vascular plants’, *Nano letters* **14**(1), 305–310.
- Gauger, E. M., Downton, M. T. & Stark, H. (2009), ‘Fluid transport at low reynolds number with magnetically actuated artificial cilia’, *The European Physical Journal E* **28**(2), 231–242.
- Ghanbari, A. & Bahrami, M. (2011), ‘A novel swimming microrobot based on artificial cilia for biomedical applications’, *Journal of Intelligent & Robotic Systems* **63**(3-4), 399–416.
- Golestanian, R., Yeomans, J. M. & Uchida, N. (2011), ‘Hydrodynamic synchronization at low reynolds number’, *Soft Matter* **7**(7), 3074–3082.
- Grattan, L. & Meggitt, B. (2013), *Optical fiber sensor technology: Advanced applications-Bragg gratings and distributed sensors*, Springer Science & Business Media.
- Greenspon, J. E. (1961), ‘Vibrations of cross-stiffened and sandwich plates with application to underwater sound radiators’, *The Journal of the Acoustical Society of America* **33**(11), 1485–1497.
- Grenander, U. (1959), *Probability and Statistics: The Harald Cramer Volume*, Alqvist & Wiksell.
- Griffiths, G. (2002), *Technology and applications of autonomous underwater vehicles*, CRC Press.
- Gueron, S. & Levit-Gurevich, K. (2001), ‘A three-dimensional model for ciliary motion based on the internal 9+ 2 structure’, *Proceedings of the Royal Society of London. Series B: Biological Sciences* **268**(1467), 599–607.
- Gueron, S., Levit-Gurevich, K., Liron, N. & Blum, J. J. (1997), ‘Cilia internal mechanism and metachronal coordination as the result of hydrodynamical coupling’, *Proceedings of the National Academy of Sciences* **94**(12), 6001–6006.

- Hagan, M. T. & Menhaj, M. B. (1994), ‘Training feedforward networks with the marquardt algorithm’, *IEEE transactions on Neural Networks* **5**(6), 989–993.
- Han, S. M., Benaroya, H. & Wei, T. (1999), ‘Dynamics of transversely vibrating beams using four engineering theories’, *Journal of Sound and vibration* **225**(5), 935–988.
- Hanke, W. & Bleckmann, H. (2004), ‘The hydrodynamic trails of *lepomis gibbosus* (centrarchidae), *colomesus psittacus* (tetraodontidae) and *thysochromis ansorgii* (cichlidae) investigated with scanning particle image velocimetry’, *Journal of Experimental Biology* **207**(9), 1585–1596.
- Hanke, W., Brücker, C. & Bleckmann, H. (2000), ‘The ageing of the low-frequency water disturbances caused by swimming goldfish and its possible relevance to prey detection’, *Journal of Experimental Biology* **203**(7), 1193–1200.
- Hanke, W., Wieskotten, S., Marshall, C. & Dehnhardt, G. (2013), ‘Hydrodynamic perception in true seals (phocidae) and eared seals (otariidae)’, *Journal of Comparative Physiology A* **199**(6), 421–440.
- Hanke, W., Witte, M., Miersch, L., Brede, M., Oeffner, J., Michael, M., Hanke, F., Leder, A. & Dehnhardt, G. (2010), ‘Harbor seal vibrissa morphology suppresses vortex-induced vibrations’, *Journal of Experimental Biology* **213**(15), 2665–2672.
- Hastie, T., Tibshirani, R. & Friedman, J. (2009), *The elements of statistical learning: data mining, inference, and prediction*, Springer Science & Business Media.
- Jones, A. M. (1957), ‘Drag coefficients for flat plates, spheres, and cylinders moving at low reynolds numbers in a viscous fluid’.
- Ju, F. & Ling, S.-F. (2014), ‘Bioinspired active whisker sensor for robotic vibrissal tactile sensing’, *Smart materials and structures* **23**(12), 125003.
- Ju, F. & Ling, S.-F. (2015), ‘A micro whisker transducer with sensorless mechanical impedance detection capability for fluid and tactile sensing in space-limited applications’, *Sensors and Actuators A: Physical* **234**, 104–112.

- Juang, J.-G. & Chang, H.-H. (2002), Application of time delay neural network to automatic landing control, *in* ‘Proceedings of the International Conference on Control Applications’, Vol. 1, IEEE, pp. 150–155.
- Kapral, R. (2008), ‘Multiparticle collision dynamics: Simulation of complex systems on mesoscales’, *Advances in Chemical Physics* **140**, 89–146.
- Kim, D. & Möller, R. (2007), ‘Biomimetic whiskers for shape recognition’, *Robotics and Autonomous Systems* **55**(3), 229–243.
- Kim, J. & Moin, P. (1985), ‘Application of a fractional-step method to incompressible navier-stokes equations’, *Journal of computational physics* **59**(2), 308–323.
- Kim, M., Bird, J. C., Van Parys, A. J., Breuer, K. S. & Powers, T. R. (2003), ‘A macroscopic scale model of bacterial flagellar bundling’, *Proceedings of the National Academy of Sciences* **100**(26), 15481–15485.
- Kim, M. & Powers, T. R. (2004), ‘Hydrodynamic interactions between rotating helices’, *Physical review E* **69**(6), 061910.
- Kim, S., Lee, S., Lee, J., Nelson, B. J., Zhang, L. & Choi, H. (2016), ‘Fabrication and manipulation of ciliary microrobots with non-reciprocal magnetic actuation’, *Scientific reports* **6**, 30713.
- Kinosita, H. & Murakami, A. (1967), ‘Control of ciliary motion.’, *Physiological reviews* **47**(1), 53–82.
- Kinsey, J. C., Eustice, R. M. & Whitcomb, L. L. (2006), A survey of underwater vehicle navigation: Recent advances and new challenges, *in* ‘IFAC Conference of Manoeuvring and Control of Marine Craft’, Vol. 88, Lisbon, pp. 1–12.
- Klindt, G. S., Ruloff, C., Wagner, C. & Friedrich, B. M. (2016), ‘Load response of the flagellar beat’, *Physical review letters* **117**(25), 258101.
- Knight-Jones, E. (1954), ‘Relations between metachronism and the direction of ciliary beat in metazoa’, *Journal of Cell Science* **3**(32), 503–521.

- Koens, L. & Lauga, E. (2016), ‘Slender-ribbon theory’, *Physics of Fluids* **28**(1), 013101.
- Kokot, G., Vilfan, M., Osterman, N., Vilfan, A., Kavčič, B., Poberaj, I. & Babič, D. (2011), ‘Measurement of fluid flow generated by artificial cilia’, *Biomicrofluidics* **5**(3), 034103.
- Korayem, M., Ebrahimi, N. & Sotoudegan, M. (2011), ‘Frequency response of atomic force microscopy microcantilevers oscillating in a viscous liquid: A comparison of various methods’, *Scientia Iranica* **18**(5), 1116–1125.
- Kosa, G., Shoham, M. & Zaaroor, M. (2007), ‘Propulsion method for swimming microrobots’, *IEEE Transactions on Robotics* **23**(1), 137–150.
- Kotar, J., Leoni, M., Bassetti, B., Lagomarsino, M. C. & Cicutta, P. (2010), ‘Hydrodynamic synchronization of colloidal oscillators’, *Proceedings of the National Academy of Sciences* **107**(17), 7669–7673.
- Kottapalli, A. G., Asadnia, M., Miao, J., Barbastathis, G. & Triantafyllou, M. S. (2012), ‘A flexible liquid crystal polymer mems pressure sensor array for fish-like underwater sensing’, *Smart Materials and Structures* **21**(11), 115030.
- Kottapalli, A. G. P., Asadnia, M., Miao, J. & Triantafyllou, M. S. (2017), *Biomimetic microsensors inspired by marine life*, Springer.
- Kröger, R. (2008), ‘The physics of light in air and water.’.
- Krüger, Y., Hanke, W., Miersch, L. & Dehnhardt, G. (2018), ‘Detection and direction discrimination of single vortex rings by harbour seals (*phoca vitulina*)’, *Journal of Experimental Biology* **221**(8), jeb170753.
- Lauga, E. (2011), ‘Life around the scallop theorem’, *Soft Matter* **7**(7), 3060–3065.
- Lawrence, S., Giles, C. L. & Tsoi, A. C. (1997), Lessons in neural network training: Overfitting may be harder than expected, *in* ‘AAAI/IAAI’, Citeseer, pp. 540–545.

- Leal-Junior, A., Frizzera, A., Marques, C. & Pontes, M. J. (2018), ‘Mechanical properties characterization of polymethyl methacrylate polymer optical fibers after thermal and chemical treatments’, *Optical Fiber Technology* **43**, 106–111.
- Lee, D., Kim, G., Kim, D., Myung, H. & Choi, H.-T. (2012), ‘Vision-based object detection and tracking for autonomous navigation of underwater robots’, *Ocean Engineering* **48**, 59–68.
- Lee, S., Erm, L. & Jones, M. (2016), Dye visualisation of wake flow around a model submarine at yaw, *in* ‘Proceedings of the 20th Australasian Fluid Mechanics Conference, Perth, Australia’, pp. 5–8.
- Leonard, J. J., Bennett, A. A., Smith, C. M., Jacob, H. & Feder, S. (1998), Autonomous underwater vehicle navigation, *in* ‘MIT Marine Robotics Laboratory Technical Memorandum’, Citeseer.
- Lepora, N. F. (2016), ‘Biomimetic active touch with fingertips and whiskers’, *IEEE transactions on haptics* **9**(2), 170–183.
- Leshansky, A. M., Kenneth, O., Gat, O. & Avron, J. E. (2007), ‘A frictionless microswimmer’, *New Journal of Physics* **9**(5), 145.
- Lindemann, C. B. (1994), ‘A “geometric clutch” hypothesis to explain oscillations of the axoneme of cilia and flagella’, *Journal of theoretical biology* **168**(2), 175–189.
- Lindemann, C. B. (2007), ‘The geometric clutch as a working hypothesis for future research on cilia and flagella’, *Annals of the New York Academy of Sciences* **1101**(1), 477–493.
- Ma, R., Klindt, G. S., Riedel-Kruse, I. H., Jülicher, F. & Friedrich, B. M. (2014), ‘Active phase and amplitude fluctuations of flagellar beating’, *Physical review letters* **113**(4), 048101.
- Machemer, H. (1974), ‘Ciliary activity and metachronism in protozoa’, *Cilia and flagella* pp. 199–286.

- Man, Y., Page, W., Poole, R. J. & Lauga, E. (2017), ‘Bundling of elastic filaments induced by hydrodynamic interactions’, *Physical Review Fluids* **2**(12), 123101.
- Marquardt, D. W. (1963), ‘An algorithm for least-squares estimation of nonlinear parameters’, *Journal of the society for Industrial and Applied Mathematics* **11**(2), 431–441.
- Marshall, W. F. (2013), *Methods in Enzymology, Cilia*, Academic Press.
- Mason, R. & Burdick, J. (1999), Propulsion and control of deformable bodies in an ideal fluid, in ‘Proceedings 1999 IEEE International Conference on Robotics and Automation (Cat. No. 99CH36288C)’, Vol. 1, IEEE, pp. 773–780.
- Materials, A. (2000-2019), ‘Silicone rubber’. Accessed: 2019-08-12.  
**URL:** <https://www.azom.com/properties.aspx?ArticleID=920>
- Mathworks-MATLAB (2019), ‘System identification toolbox’.  
**URL:** <https://uk.mathworks.com/products/sysid.html>
- Matsumoto, G. (1991), Swimming movements of ctenophores, and the mechanics of propulsion by ctene rows, in ‘Hydrobiologia’, Vol. 216, Springer, pp. 319–325.
- Montgomery, J. C., Coombs, S. & Baker, C. F. (2001), The mechanosensory lateral line system of the hypogean form of *astyanax fasciatus*, in ‘The biology of hypogean fishes’, Springer, pp. 87–96.
- Müller, R. & Kuc, R. (2007), ‘Biosonar-inspired technology: goals, challenges and insights’, *Bioinspiration & biomimetics* **2**(4), S146.
- Murphy, C. T., Eberhardt, W. C., Calhoun, B. H., Mann, K. A. & Mann, D. A. (2013), ‘Effect of angle on flow-induced vibrations of pinniped vibrissae’, *PloS one* **8**(7), e69872.
- Muthuramalingam, M. & Bruecker, C. (2019), ‘Seal and sea lion whiskers detect slips of vortices similar as rats sense textures’, *Scientific reports* **9**(1), 1–15.
- Najafi, A. & Golestanian, R. (2004), ‘Simple swimmer at low reynolds number: Three linked spheres’, *Physical Review E* **69**(6), 062901.

- Nasouri, B., Khot, A. & Elfring, G. J. (2017), ‘Elastic two-sphere swimmer in stokes flow’, *Physical Review Fluids* **2**(4), 043101.
- Niedermayer, T., Eckhardt, B. & Lenz, P. (2008), ‘Synchronization, phase locking, and metachronal wave formation in ciliary chains’, *Chaos: An Interdisciplinary Journal of Nonlinear Science* **18**(3), 037128.
- OpenCV (2000-2019). Last accessed: 2019-08-13.  
**URL:** <https://opencv.org>
- Pearson, M. J., Mitchinson, B., Sullivan, J. C., Pipe, A. G. & Prescott, T. J. (2011), ‘Biomimetic vibrissal sensing for robots’, *Philosophical Transactions of the Royal Society B: Biological Sciences* **366**(1581), 3085–3096.
- Pikovsky, A., Kurths, J., Rosenblum, M. & Kurths, J. (2003), *Synchronization: a universal concept in nonlinear sciences*, Vol. 12, Cambridge university press.
- Polmanteer, K. E. (1988), ‘Silicone rubber, its development and technological progress’, *Rubber chemistry and technology* **61**(3), 470–502.
- Prescott, T. J., Mitchinson, B. & Grant, R. A. (2011), ‘Vibrissal behavior and function’, *Scholarpedia* **6**(10), 6642.
- Purcell, E. M. (1977), ‘Life at low reynolds number’, *American journal of physics* **45**(1), 3–11.
- Putz, V. B. & Yeomans, J. M. (2009), ‘Hydrodynamic synchronisation of model microswimmers’, *Journal of Statistical Physics* **137**(5-6), 1001.
- Rao, S. S. (2007), *Vibration of continuous systems*, Vol. 464, Wiley Online Library.
- Reichert, M. & Stark, H. (2005), ‘Synchronization of rotating helices by hydrodynamic interactions’, *The European Physical Journal E* **17**(4), 493–500.
- Ren, L., Nama, N., McNeill, J. M., Soto, F., Yan, Z., Liu, W., Wang, W., Wang, J. & Mallouk, T. E. (2019), ‘3d steerable, acoustically powered microswimmers for single-particle manipulation’, *Science advances* **5**(10), eaax3084.

- Ricci, N. (1990), ‘The behaviour of ciliated protozoa’, *Animal behaviour* **40**(6), 1048–1069.
- Rockenbach, A., Mikulich, V., Brücker, C. & Schnakenberg, U. (2015), ‘Fluid transport via pneumatically actuated waves on a ciliated wall’, *Journal of Micromechanics and Microengineering* **25**(12), 125009.
- Rockenbach, A. & Schnakenberg, U. (2015), ‘Structured pdms used as active element for a biomimetics inspired fluid transporter’, *Lékař a technika-Clinician and Technology* **45**(2), 37–41.
- Rosenbloom, P. (1956), The method of steepest descent, in ‘Proc Symp Appl Math’, Vol. 6, pp. 127–176.
- Rüffer, U. & Nultsch, W. (1997), ‘Flagellar photoresponses of ptx1, a nonphototactic mutant of chlamydomonas’, *Cell motility and the cytoskeleton* **37**(2), 111–119.
- Sanchez, T., Welch, D., Nicastro, D. & Dogic, Z. (2011), ‘Cilia-like beating of active microtubule bundles’, *Science* **333**(6041), 456–459.
- Sawamoto, K., Wichterle, H., Gonzalez-Perez, O., Cholfin, J. A., Yamada, M., Spassky, N., Murcia, N. S., Garcia-Verdugo, J. M., Marin, O., Rubenstein, J. L. et al. (2006), ‘New neurons follow the flow of cerebrospinal fluid in the adult brain’, *Science* **311**(5761), 629–632.
- Sawyer, E. K., Turner, E. C. & Kaas, J. H. (2016), ‘Somatosensory brainstem, thalamus, and cortex of the california sea lion (*zalophus californianus*)’, *Journal of Comparative Neurology* **524**(9), 1957–1975.
- Schrope, M. (2002), ‘Whale deaths caused by us navy’s sonar’, *Nature* **415**(6868), 106–106.
- Schulte-Pelkum, N., Wieskotten, S., Hanke, W., Dehnhardt, G. & Mauck, B. (2007), ‘Tracking of biogenic hydrodynamic trails in harbour seals (*phoca vitulina*)’, *Journal of Experimental Biology* **210**(5), 781–787.

- Shih, C., Litt, M., Khan, M. & Wolf, D. (1977), 'Effect of nondialyzable solids concentration and viscoelasticity on ciliary transport of tracheal mucus', *American Review of Respiratory Disease* **115**(6), 989–995.
- Short, M. B., Solari, C. A., Ganguly, S., Powers, T. R., Kessler, J. O. & Goldstein, R. E. (2006), 'Flows driven by flagella of multicellular organisms enhance long-range molecular transport', *Proceedings of the National Academy of Sciences* **103**(22), 8315–8319.
- Sleigh, M. (1963), 'Movements and co-ordination of the ciliary comb plates of the ctenophores *Beroë* and *Pleurobrachia*', *Nature* **199**(4893), 620–621.
- Sleigh, M. (1968), 'Metachronal co-ordination of the comb plates of the ctenophore *Pleurobrachia*', *Journal of Experimental Biology* **48**(1), 111–125.
- Sleigh, M. (1974), 'Metachronism of cilia of metazoa', *Cilia and flagella* pp. 287–304.
- Smith, D., Gaffney, E. & Blake, J. (2008), 'Modelling mucociliary clearance', *Respiratory physiology & neurobiology* **163**(1-3), 178–188.
- Stone, H. A. & Samuel, A. D. (1996), 'Propulsion of microorganisms by surface distortions', *Physical review letters* **77**(19), 4102.
- Strogatz, S. H. (2012), *Sync: How order emerges from chaos in the universe, nature, and daily life*, Hachette UK.
- Subramaniam, V., y Alvarado, P. V. & Weymouth, G. (2017), Sensing on robots inspired by nature, *in* 'Biomimetic microsensors inspired by marine life', Springer, pp. 77–110.
- Sullivan, J. C., Mitchinson, B., Pearson, M. J., Evans, M., Lepora, N. F., Fox, C. W., Melhuish, C. & Prescott, T. J. (2011), 'Tactile discrimination using active whisker sensors', *IEEE Sensors Journal* **12**(2), 350–362.
- Summarell, C. C. G., Ingle, S., Fish, F. E. & Marshall, C. D. (2015), 'Comparative analysis of the flexural stiffness of pinniped vibrissae', *PloS one* **10**(7).

- TAMM, S. L. (1973), ‘Mechanisms of ciliary co-ordination in ctenophores’, *Journal of Experimental Biology* **59**(1), 231–245.
- Tamm, S. L. (1983), ‘Motility and mechanosensitivity of macrocilia in the ctenophore *Beroë*’, *Nature* **305**(5933), 430–433.
- Tamm, S. L. (1984), ‘Mechanical synchronization of ciliary beating within comb plates of ctenophores’, *Journal of experimental biology* **113**(1), 401–408.
- Tao, J. & Yu, X. B. (2012), ‘Hair flow sensors: from bio-inspiration to biomimicking—a review’, *Smart Materials and Structures* **21**(11), 113001.
- Tritton, D. J. (2012), *Physical fluid dynamics*, Springer Science & Business Media.
- Trouilloud, R., Tony, S. Y., Hosoi, A. & Lauga, E. (2008), ‘Soft swimming: Exploiting deformable interfaces for low reynolds number locomotion’, *Physical review letters* **101**(4), 048102.
- Underwater Robotics Market Size* (2018), Share & Trends Analysis Report by Type, 2018 to 2025, Grand View Research, Retrieved from: <https://www.grandviewresearch.com/industry-analysis/underwater-robotics-market>.
- Vančura, C., Dufour, I., Heinrich, S. M., Josse, F. & Hierlemann, A. (2008), ‘Analysis of resonating microcantilevers operating in a viscous liquid environment’, *Sensors and Actuators A: Physical* **141**(1), 43–51.
- Vicider, C., Ohman, O. & Elderstig, H. (1995), A pneumatically actuated micro valve with a silicone rubber membrane for integration with fluid-handling systems, in ‘Proceedings of the International Solid-State Sensors and Actuators Conference-TRANSDUCERS’95’, Vol. 2, IEEE, pp. 284–286.
- Violette, R., De Langre, E. & Szydlowski, J. (2007), ‘Computation of vortex-induced vibrations of long structures using a wake oscillator model: comparison with dns and experiments’, *Computers & structures* **85**(11-14), 1134–1141.

- Viswanath, D. S., Ghosh, T. K., Prasad, D. H., Dutt, N. V. & Rani, K. Y. (2007), *Viscosity of liquids: theory, estimation, experiment, and data*, Springer Science & Business Media.
- Von Campenhausen, C., Riess, I. & Weissert, R. (1981), 'Detection of stationary objects by the blind cave fish *hanoptichthys jordani* (characidae)', *Journal of comparative physiology* **143**(3), 369–374.
- Waibel, A., Hanazawa, T., Hinton, G., Shikano, K. & Lang, K. J. (1989), 'Phoneme recognition using time-delay neural networks', *IEEE transactions on acoustics, speech, and signal processing* **37**(3), 328–339.
- Waters, A. M. & Beales, P. L. (2011), 'Ciliopathies: an expanding disease spectrum', *Pediatric nephrology* **26**(7), 1039–1056.
- Wieskotten, S., Dehnhardt, G., Mauck, B., Miersch, L. & Hanke, W. (2010a), 'Hydrodynamic determination of the moving direction of an artificial fin by a harbour seal (*phoca vitulina*)', *Journal of Experimental Biology* **213**(13), 2194–2200.
- Wieskotten, S., Dehnhardt, G., Mauck, B., Miersch, L. & Hanke, W. (2010b), 'The impact of glide phases on the trackability of hydrodynamic trails in harbour seals (*phoca vitulina*)', *Journal of Experimental Biology* **213**(21), 3734–3740.
- Wieskotten, S., Mauck, B., Miersch, L., Dehnhardt, G. & Hanke, W. (2011), 'Hydrodynamic discrimination of wakes caused by objects of different size or shape in a harbour seal (*phoca vitulina*)', *Journal of Experimental Biology* **214**(11), 1922–1930.
- Williamson, C. H. (1996), 'Vortex dynamics in the cylinder wake', *Annual review of fluid mechanics* **28**(1), 477–539.
- Wilson, E. O. (1962), 'Chemical communication among workers of the fire ant *solenopsis saevissima* (fr. smith) 1. the organization of mass-foraging', *Animal behaviour* **10**(1-2), 134–147.

- Windsor, S. P., Tan, D. & Montgomery, J. C. (2008), ‘Swimming kinematics and hydrodynamic imaging in the blind mexican cave fish (*astyanax fasciatus*)’, *Journal of Experimental Biology* **211**(18), 2950–2959.
- Xie, J.-X., Cheng, C., Chau, K.-W. & Pei, Y.-Z. (2006), ‘A hybrid adaptive time-delay neural network model for multi-step-ahead prediction of sunspot activity’, *International journal of environment and pollution* .
- Xu, T., Hwang, G., Andreff, N. & Régnier, S. (2014), ‘Modeling and swimming property characterizations of scaled-up helical microswimmers’, *IEEE/ASME Transactions on Mechatronics* **19**(3), 1069–1079.
- y Alvarado, P. V., Subramaniam, V. & Triantafyllou, M. (2012), Design of a bio-inspired whisker sensor for underwater applications, *in* ‘SENSORS, 2012 IEEE’, IEEE, pp. 1–4.
- Yang, Y., Chen, J., Engel, J., Pandya, S., Chen, N., Tucker, C., Coombs, S., Jones, D. L. & Liu, C. (2006), ‘Distant touch hydrodynamic imaging with an artificial lateral line’, *Proceedings of the National Academy of Sciences* **103**(50), 18891–18895.
- Yang, Y., Elgeti, J. & Gompper, G. (2008), ‘Cooperation of sperm in two dimensions: synchronization, attraction, and aggregation through hydrodynamic interactions’, *Physical Review E* **78**(6), 061903.
- Yu, Y.-S., Zhao, Z.-Y., Zhuo, Z.-C., Zheng, W., Qian, Y. & Zhang, Y.-S. (2004), ‘Bend sensor using an embedded etched fiber bragg grating’, *Microwave and Optical Technology Letters* **43**(5), 414–417.
- Zhuang, C., Kubilius, J., Hartmann, M. J. & Yamins, D. L. (2017), Toward goal-driven neural network models for the rodent whisker-trigeminal system, *in* ‘Advances in Neural Information Processing Systems’, pp. 2555–2565.